The UVic Earth System Climate Model: Model Description, Climatology, and Applications to Past, Present and Future Climates

Andrew J. Weaver[1], Michael Eby[1], Edward C. Wiebe[1], Cecilia M. Bitz[2], Phil B. Duffy[4], Tracy L. Ewen [1], Augustus F. Fanning[1], Marika M. Holland[3], Amy MacFadyen[1], Oleg Saenko[1], Andreas Schmittner[1], Huaxiao Wang[4], Masakazu Yoshimori[1]

[1]School of Earth and Ocean Sciences
University of Victoria
PO Box 3055, Victoria, BC, V8W 3P6
Canada

[2]Polar Science Center
Applied Physics Laboratory
1013 NE 40th Street
Seattle, WA, 98105
USA

[3]National Center for Atmospheric Research
PO Box 3000, Boulder, CO, 80307
USA

[4]Lawrence Livermore National Laboratory
PO Box 808, Livermore, CA, 94550
USA

submitted to *Atmosphere-Ocean*
November, 2000

Abstract

A new earth system climate model of intermediate complexity is developed and its climatology is compared against observations. The UVic Earth System Climate Model consists of a three-dimensional ocean general circulation model coupled to a thermodynamic/dynamic sea ice model, an energy-moisture balance atmospheric model with dynamical feedbacks, and a thermomechanical land ice model. In order to keep the model computationally efficient a reduced complexity atmosphere model is used. Atmospheric heat and freshwater transports are parametrised through Fickian diffusion, and precipitation is assumed to occur when the relative humidity reaches greater than 85%. Moisture transport can also be accomplished through advection if desired. Precipitation over land is assumed to instantaneously return to the ocean via one of 33 observed river drainage basins. Ice and snow albedo feedbacks are included in the coupled model by locally increasing the prescribed latitudinal profile of the planetary albedo. The atmospheric model includes a parametrisation of water vapour/planetary long wave feedbacks, although the radiative forcing associated with changes in atmospheric CO_2 is prescribed as a modification of the planetary long wave radiative flux. A specified lapse rate is used to reduce the surface temperature over land where there is topography. The model uses prescribed present day winds in its climatology although a dynamical wind feedback is included which exploits a latitudinally-varying empirical relationship between atmospheric surface temperature and density. The ocean component of the coupled model is based on the GFDL Modular Ocean Model 2.2, with a global resolution of a 3.6° (zonal) by 1.8° (meridional) and 19 vertical levels, that includes an option for a brine-rejection parametrisation. The sea ice component incorporates an elastic-viscous-plastic rheology to represent sea ice dynamics and various options for the representation of sea ice thermodynamics and thickness distribution. The systematic comparison of the coupled model with observations reveals good agreement, especially when moisture transport is accomplished through advection.

Global warming simulations conducted using the model to explore the role of moisture advection reveal a climate sensitivity of 3.0°C for a doubling of CO_2, in line with other more comprehensive coupled models. Moisture advection, together with the wind feedback leads to a transient simulation in which the meridional overturning in the North Atlantic initially weakens, but eventually re-establishes to its initial strength once the radiative forcing is held fixed, as found in many coupled atmosphere GCMs. This is in contrast to experiments in which moisture transport is accomplished through diffusion whereby the overturning re-establishes to a strength that is greater than its initial condition.

When applied to the climate of the Last Glacial Maximum, the model obtains tropical cooling (30°N – 30°S), relative to the present, of about 2.1°C over the ocean and 3.6°C over the land. These are generally cooler than CLIMAP estimates, but not as cool as some other reconstructions. This moderate cooling is consistent with alkenone reconstructions and a low to mid climate sensitivity to perturbations in radiative forcing. An

amplification of the cooling occurs in the North Atlantic due to the weakening of North Atlantic Deep Water formation. Concurrent with this weakening is a shallowing and a more northward penetration of Antarctic Bottom Water.

Climate models are usually evaluated by spinning them up under perpetual present-day forcing and comparing the model results with present-day observations. Implicit in this approach is the assumption that the present day observations are in equilibrium with the present day radiative forcing. The comparison of a long transient integration (starting at 6 KBP), forced by changing radiative forcing (solar, CO_2, orbital), with an equilibrium integration reveals substantial differences. Relative to the climatology from the present-day equilibrium integration, the global mean surface air and sea surface temperatures (SSTs) are 0.74°C and 0.55°C colder, respectively, deep ocean temperatures are substantially cooler, and southern hemisphere sea ice cover is 22% larger, although the North Atlantic conveyor remains remarkably stable in all cases. The differences are due to the long timescale memory of the deep ocean to climatic conditions which prevailed throughout the late Holocene. It is also demonstrated that a global warming simulation that starts from an equilibrium present-day climate (cold start) underestimates the global temperature increase at 2100 by 13% when compared to a transient simulation, under historical solar, CO_2 and orbital forcing, that is also extended out to 2100. This is larger (13% compared to 9.8%) than the difference from an analogous transient experiment which does not include historical changes in solar forcing. These results suggest that those groups that do not account for solar forcing changes over the 20th century may slightly underestimate (˜3% in our model) the projected warming by the year 2100.

1 Introduction

Coupled atmosphere-ocean general circulation models (GCMs) are frequently used to understand both past, present and future climate and climate variability. The computational expense associated with these models, however, often precludes their use for undertaking extensive parameter sensitivity studies. While they must ultimately be used as the primary tool for undertaking climate projections on which policy will be based, it is important to conduct sensitivity studies in parallel using simpler models. Simple models, or models of intermediate complexity, allow one to explore the climate sensitivity associated with a particular process or component of the climate system over a wide range of parameters. In addition, they allow one to streamline the experiments that are performed using more complicated GCMs. These more idealised coupled models vary in complexity from simple one dimensional energy balance/upwelling diffusion models (Wigley and Raper 1987 1992; Raper et al. 1996; Wigley 1998), to zonally-averaged ocean/energy balance atmosphere models (Stocker et al. 1992; Stocker and Schmittner 1997), to models with more sophisticated subcomponents (Fanning and Weaver 1996; Petoukhov et al. 2000).

1.1 Models of Intermediate Complexity

Simple and intermediate complexity climate models are designed with a particular class of scientific questions in mind. In the development of the model, only those processes and parametrisations are included which are deemed important in the quest to address the scientific questions of concern. For example, Wigley (1998) used an upwelling diffusion-energy balance climate model (see Kattenberg et al. (1996)) to evaluate Kyoto Protocol implications for increases in global mean temperature and sea level. While such a simple climate model relies on climate sensitivity and ice-melt parameters obtained from coupled atmosphere-ocean GCM, it nevertheless allows for a first-order analysis of the climatic consequence of various post-Kyoto emissions reductions. The results from this analysis suggested very minor effects on global mean temperature under a range of post-Kyoto emissions. Stocker and Schmittner (1997) used a three-basin zonally-averaged ocean circulation model coupled to a simple energy-balance atmospheric model (described in Stocker et al. (1992)), to undertake a systematic parameter sensitivity study of the response of the North Atlantic thermohaline circulation to both the rate of increase and equilibrium concentration of atmospheric CO_2. They showed that in general, the slower the rate of increase in atmospheric CO_2, the greater the equilibrium concentration required to permanently shut down the conveyor in the North Atlantic. While the actual critical thresholds that arose from this study would need verification by more complicated models, the study clearly illustrates the importance of the rate of CO_2 increase on the North Atlantic thermohaline circulation, a result difficult, if not impossible, to achieve with the computationally expensive present generation coupled models.

The CLIMBER group at the Potsdam Institute have taken the approach of building a climate model of intermediate complexity to examine climate change and variability with a sophisticated, albeit highly parametrised, atmospheric component. Their atmospheric model is based on the statistical-dynamical approach without resolving synoptic variability (Petoukhov et al. 2000; Ganopolski et al. 2001). Their three-basin, zonally-averaged ocean component is very similar to the ocean component of Stocker and Schmittner (1997) and they also incorporate a simple dynamic/thermodynamic ice model. The CLIMBER-2 model sacrifices resolution (10° latitudinal by 51° zonal) and complexity for computational efficiency. This model has been used to investigate both the climate of the last glacial maximum (LGM —Ganopolski et al. (1998)) as well as the cause for the collapse of the conveyor in global warming experiments (Rahmstorf and Ganopolski 1999).

Fanning and Weaver (1996) developed an energy-moisture balance model coupled to an ocean general circulation model and a thermodynamic sea-ice model. This model has been used to undertake a number of sensitivity studies including the role of sub-grid-scale ocean mixing (and flux adjustments — Fanning and Weaver (1997a)) in global warming experiments (Wiebe and Weaver 1999) and steric sea level rise (Weaver and Wiebe 1999), and the ocean's role in the LGM and Ordovician climates (Weaver et al. 1998; Poussart et al. 1999).

All of the simple or intermediate complexity climate models discussed above are free of explicit flux adjustments. Nevertheless, these same models necessarily include implicit adjustments through the fine tuning, within observational ranges, of internal model parameters in an attempt to reproduce the present-day climate.

One of the purposes of this paper is to document the climatology of and parametrisations used in a new intermediate complexity earth system climate model (ESCM) which has substantially evolved from the earlier version described by Fanning and Weaver (1996). This new model incorporates a better representation of atmospheric processes, including the addition of moisture advection, orography and wind feedbacks, as well as more sophisticated sea ice and snow models, and a dynamical ice sheet model.

Our philosophy in building this model is to develop a tool with which to understand processes and feedbacks operating within the climate system on decadal and longer timescales. We include a full three-dimensional ocean GCM as we believe horizontal ocean gyre transports and subduction processes are fundamental to the stability and variability of the thermohaline circulation, and as we believe the latter is important for climate/paleoclimate change/variability on long timescales. Our atmospheric model is simple, although we believe that it captures the necessary surface balances and feedbacks of heat, freshwater and momentum. Atmospheric 'weather' is not calculated explicitly in our model, although in some applications its statistics have been added as a forcing. This allows our model to reach an equilibrium climate free of variability, both internal to the atmosphere, and excited in the ocean and sea ice subcomponent models. The sophisticated sea ice model was built and tested within the context of the ESCM and has since been included in the Canadian Centre for Climate Modelling and

Analysis (CCCma) coupled AOGCM. The glaciological model was developed at the University of British Columbia and coupled into our model while the inorganic chemistry subcomponent was built following the guidelines of the international Ocean Carbon-Cycle Model Intercomparison Project. By building the ESCM in a systematic fashion, we ensure that energy and moisture are conserved exactly as all parameters are consistent between all subcomponent models.

Our approach is complementary to that of major coupled AOGCM centres, and our model fills an important gap within the hierarchy of climate models (Claussen et al. 2000; Shackley et al. 1998). In fact, our model has been used, and is still being used, as a tool with which to examine the sensitivity of a particular process or subcomponent model across a wide range of parameters, in order to streamline the process of improving certain components of the CCCma coupled AOGCM. The complexity of the CCCma AOGCM is such that relatively few 'production runs' can be conducted, leaving systematic parameter sensitivity analyses to be conducted with the UVic ESCM.

1.2 Initialisation of Coupled Models

In developing coupled atmosphere-ocean GCMs, it is common to integrate them to equilibrium under present day radiative forcing (in the case of coupled atmosphere-ocean models) or using present day surface boundary conditions (in the case of ocean- or atmosphere-only models). The evaluation process then involves a detailed comparison of model results with present-day observations (e.g., Oreskes and Belitz (1994); Gates et al. (1996); Flato et al. (2001)). Since the ocean, and especially its deep and weakly ventilated regions, have a long adjustment time to changes in radiative forcing, the present-day oceanic observations are not in equilibrium with the present forcing. As such, models which start from a control integration which is in equilibrium with its radiative forcing suffer from a warm bias (Weaver and Wiebe 1999). Even if the ocean or coupled model were perfect, it would therefore not be possible to reproduce these observations under perpetual present-day model forcing. Many coupled atmosphere-ocean climate GCMs, that have been used to examine the transient response of the climate system to increasing greenhouse gases, start from a present-day equilibrium climate (see Kattenberg et al. (1996)). This equilibrium climate is usually obtained by separately spinning up the oceanic and atmospheric components of the coupled model under perpetual present day forcing (see Weaver and Hughes (1996) for a review). Upon coupling, flux adjustments are often employed to avoid climate drift. It has been suggested that this approach leads to an apparent 'cold start' problem (Fichefet and Tricot 1992; Hasselmann et al. 1993; Cubasch et al. 1994; Keen and Murphy 1997), and it has been argued that since the prior build up of radiative forcing has been neglected, the initial rate of warming is slower than it should otherwise be (see Kattenberg et al. (1996)).

This apparent problem has been dealt with recently by most coupled model groups by accounting for the 20$^{\mathrm{th}}$

century build up of atmospheric CO_2 through long integrations starting from preindustrial times. Nevertheless, these same models evaluate their present-day climate obtained from present-day radiative forcing, assume that the present-day climate is representative of 1850, and then impose changes in radiative forcing to the present-day climate consistent with changes since 1850 (Mitchell et al. 1995). Some more recent efforts (e.g., HadCM3 — Gordon et al. (2000)) have actually used preindustrial levels of greenhouse gases in their coupled model initialisation, although the evaluation problem still remains as insufficient data exist to properly validate the equilibrium model climate with the preindustrial observational record. A second goal of this study is to quantify the memory of the present-day ocean to prior conditions through an examination of its response to 6000 years of changing radiative forcing. This should be viewed as an extension of Weaver et al. (2000) in that we consider here not only the effects of changing CO_2 and orbital forcing, but also changes in solar luminosity.

1.3 The Climate of the Last Glacial Maximum

The issue of tropical cooling at the LGM represents a challenge for both the paleoclimate data and modelling communities. Conflicting evidence has emerged from the reconstruction community with tropical coral (Guilderson et al. 1994; Beck et al. 1997), noble gas (Stute et al. 1995), ice core (Thompson et al. 1995), and sediment (Curry and Oppo 1997) records inferring tropical temperatures substantially colder than today. Alkenone records (Sikes and Keigwin 1994; Bard et al. 1997; Lyle et al. 1992), on the other hand, have inferred tropical temperatures colder than CLIMAP Project Members (1976 1981) reconstructions (which were close to today's) but only slightly colder than present.

Simulations with coupled models also disagree on estimates of tropical temperatures during the LGM. Ganopolski et al. (1998), using the CLIMBER-2 model, and Bush and Philander (1998), using ocean and atmospheric GCMs that were coupled together and integrated under LGM forcing for 15 years (starting from a present-day initial condition), found much cooler tropical LGM temperatures than today. Weaver et al. (1998), using a coupled OGCM/energy-moisture balance model and Broccoli (2000), using an AGCM coupled to a mixed layer ocean model, found tropical temperatures only slightly cooler than today and consistent with alkenone reconstructions (see also Crowley (2000)). A final goal of this paper is to reexamine this issue, once more with our new ESCM.

1.4 Outline

The outline of the rest of this paper is as follow: In the next section we provide a detailed description of the UVic ESCM, starting with the atmospheric component (section 2.1) then moving to the cryospheric components (sea ice, land ice and snow — section 2.2) and the oceanic component (section 2.3). In section 3 we provide a comparison between the model climatology and observations using a diffusive approximation for moisture transport. This approximation is relaxed in section 4 where moisture advection is included and in section 5 we perform global warming simulations with and without this moisture advection option. The climate of the LGM, and in particular the resulting tropical SSTs and Atlantic thermohaline circulation, are examined in section 6. In section 7 we perform experiments similar to those done by Weaver et al. (2000) in which we analyse the differences between the results from a transient experiment starting at 6KBP and two experiments conducted with perpetual 1850 and 1998 radiative forcing. We also extend the transient integration out to 2100 to study the cold start problem. Our results are summarised in section 8.

2 Model Description

The coupled model consists of an energy-moisture balance atmospheric model, loosely based on Fanning and Weaver (1996), a dynamic-thermodynamic sea ice model (Hibler 1979; Hunke and Dukowicz 1997; Bitz et al. 2001) and a primitive equation oceanic general circulation model (Pacanowski 1995). The model is global in coverage with a spherical grid resolution of 3.6° (zonal) by 1.8° (meridional), similar to the resolution used in most coupled atmosphere-ocean general circulation models. A new feature of this model is that the poles in the ocean, atmosphere and sea ice subcomponents have been rotated such that the North Pole is in Greenland while the South Pole remains in Antarctica (see Fig. 1). This simple Euler angle grid rotation (Appendix A) removes the problem of grid convergence near the North Pole, thereby eliminating the need for filtering or the placement of an artificial island at the pole in the ocean model. The only modification from a "standard" spherically-gridded version of the model is that variables that are normally a function of grid latitude, such as the Coriolis parameter, are transformed so that they remain a function of geographic latitude.

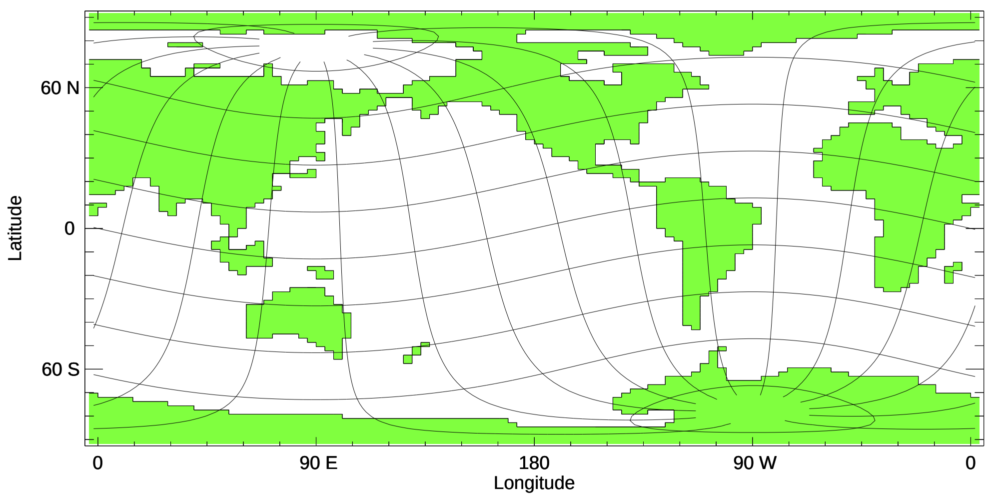

Figure 1: Model grid showing lines of geographic latitude and longitude in the rotated frame of reference. Rotated lines of geographic latitude are every 20 degrees and lines of longitude are every 30 degrees.

2.1 Atmospheric Model

The atmospheric model uses the Fanning and Weaver (1996) energy-moisture balance model as its starting point. The formulation of the vertically-integrated thermodynamic energy balance equations assumes a decreasing vertical distribution of energy and specific humidity (from surface values) with specified e-folding scale heights. The prognostic equations for momentum conservation are replaced by specified wind data, although dynamical wind feedbacks are also included (section 2.1.1). The other major simplification to the atmosphere is the parametrisation of atmospheric heat and moisture transport by diffusion, although moisture advection by the winds is also included as an option (section 4).

The vertically-integrated atmospheric thermodynamic energy balance equation is given by:

$$\rho_a h_t c_{pa} \frac{\partial T_a}{\partial t} = Q_T + Q_{SW} C_A + Q_{LH} + Q_{LW} + Q_{SH} - Q_{PLW} \tag{1}$$

where $\rho_a = 1.25$ kgm^{-3} is a constant surface air density, $h_t = 8.4$ km (Gill 1982) is a constant representative scale height for temperature, $c_{pa} = 1004$ Jkg^{-1}K^{-1} is the specific heat of air at constant pressure, and T_a is the sea level air temperature. The terms on the right hand side of Eq. (1) represent sources or sinks of heat for the atmosphere.

The heat transport term Q_T is parametrised by Fickian diffusion, and takes the form:

$$Q_T = \rho_a h_t c_{pa} \nabla \bullet (\nu \nabla T_a) \tag{2}$$

where $\nabla(\nu \nabla T_a)$ is the diffusion operator (Appendix B) acting on T_a with diffusivity ν (section 4; Fig. 23).

The incoming short wave radiation at the top of the atmosphere is given by:

$$Q_{SW} = \frac{S_\odot}{4} I(1 - \alpha) \tag{3}$$

where $S_\odot = 1368$ Wm^{-2} is the solar constant and I is the annual distribution of insolation entering the top of the atmosphere (Berger 1978). The planetary albedo α varies as a function of latitude and time of year to account for the effects of changes in solar zenith angle (Graves et al. 1993). $C_A = 0.3$ (da Silva et al. 1994) is an absorption coefficient which parametrises the absorption of heat in the atmosphere by water vapour, dust, ozone and clouds etc. (Ramanathan et al. 1987). We refer the reader to Fanning and Weaver (1996) for an extensive parameter sensitivity study of the stand-alone EMBM to C_A.

The latent heat flux into the atmosphere takes the form:

$$Q_{LH} = \rho_o P \begin{cases} L_v & \text{if P is rain} \\ L_s & \text{if P is snow} \end{cases} \tag{4}$$

where ρ_o is a reference density of water, $L_v = 2.50 \times 10^6$ J kg^{-1} is the latent heat of vapourization,

$L_s = 2.84 \times 10^6$ J kg^{-1}is the latent heat of sublimation and P is the precipitation (in ms^{-1}) .

The parametrisation for outgoing planetary long wave radiation Q_{PLW} is taken from Thompson and Warren (1982) and depends on the surface relative humidity (r) and temperature (T_a). This term is modified to parametrise the radiative forcing associated with changes in atmospheric CO_2 concentration, and is given by:

$$\begin{aligned} Q_{PLW} = & \quad c_{00} + c_{01}r + c_{02}r^2 \\ + & \quad (c_{10} + c_{11}r + c_{12}r^2)T_a \\ + & \quad (c_{20} - c_{21}r + c_{22}r^2)T_a^2 \\ + & \quad (c_{30} + c_{31}r + c_{32}r^2)T_a^3 \\ - & \quad \Delta \mathrm{F}_{2x} ln \frac{C(t)}{C_o} \end{aligned} \tag{5}$$

where $C(t)/C_o$ is the ratio of the prescribed atmospheric CO_2 concentration to a present day reference level ($C_o = 350$ ppm), and $\Delta\mathrm{F}_{2x} = 5.77$ Wm^{-2} corresponds to a specified radiative forcing of 4 Wm^{-2} for a doubling of atmospheric CO_2 (Ramanathan et al. 1987). The constants in Eq. 5 are taken from Table 3 of Thompson and Warren (1982).

The long wave radiation emitted by the Earth's surface is absorbed by the atmosphere and re-emitted both upward and downward. The net upward long wave radiative flux into the atmosphere can be written as:

$$Q_{LW} = \varepsilon_s \sigma T_s^4 - \varepsilon_a \sigma T_a^4 \tag{6}$$

where T_s is the surface temperature and $\varepsilon_s = 0.94$ and ε_a are the surface and atmospheric emissivities, and $\sigma = 5.67 \times 10^{-8}$ Wm^{-2}K^{-4} is the Stefan-Boltzmann constant. The atmospheric emissivity is taken from Fig. 2a of Fanning and Weaver (1996), scaled by 0.98. A bulk parametrisation is used for the calculation of the sensible heat flux,

$$Q_{SH} = \rho_a C_H c_{pa} U (T_s - T_a) \tag{7}$$

where $C_H = 0.94 C_E$ (Isemer et al. 1989) is the Stanton number and C_E is the Dalton number (see below), and U is the surface wind speed. We refer the reader to Fanning and Weaver (1996) for an extensive parameter sensitivity study of the stand-alone EMBM to ε_s, ε_a, T_s, and U.

The vertically-integrated moisture balance equation is given by,

$$\rho_a h_q \left\{ \frac{\partial q_a}{\partial t} - \nabla \cdot (\kappa \nabla q_a) \right\} = \rho_o (E - P) \tag{8}$$

where $h_q = 1.8$ km (Peixoto and Oort 1992) is a constant scale height for specific humidity, q_a is the surface specific humidity, κ is an eddy diffusivity (section 4; Fig. 23), E is evaporation (in ms^{-1}) or sublimation and P is precipitation. Evaporation (or sublimation) is calculated from the following bulk formula:

$$E = \frac{\rho_a C_E U}{\rho_o}(q_s(T_s) - q_a) \tag{9}$$

where C_E is the time-dependent Dalton number calculated according to Eq. 18 of Fanning and Weaver (1996) and $q_s(T_s)$ is the saturation specific humidity:

$$q_s(T) = c_1 exp \begin{cases} \left(\frac{c_2 T}{T + c_3}\right) & \text{if } T = T_i \\ \left(\frac{c_4 T}{T + c_5}\right) & \text{otherwise} \end{cases} \tag{10}$$

where T is the ocean (T_o) or ice (T_i) surface temperature, in the calculation of E (Eq. 9), or the air temperature (T_a) in the calculation of precipitation P (Eq. 11). The constants in Eq. 10 are defined as: $c_1 = 3.80$ gkg^{-1}, $c_2 = 21.87$, $c_3 = 265.5$ °C, $c_4 = 17.67$, and $c_5 = 243.5$ °C (Bolton 1980). Precipitation is assumed to occur whenever the relative humidity r is greater than a specified threshold $r_{max} = 0.85$, and is given by:

$$P = \begin{cases} \frac{\rho_a h_q}{\rho_o \Delta t}(q_a - r_{max} q_s(T_a)) & \text{if } r > r_{max} \\ 0 & \text{otherwise} \end{cases} \tag{11}$$

where Δt is the model time step, $q_s(T_a)$ is the saturation specific humidity at air temperature T_a.

No heat or moisture is stored on the land surface, so $E = 0$ and the heat radiated back to the atmosphere from the surface ($Q_{LW} + Q_{SH}$) must equal the short wave radiation reaching the surface ($Q_{SW}(1 - C_A)$). Over land Eq. (1) becomes:

$$\rho_a h_a c_{\rho_a} \frac{\partial T_a}{\partial t} = Q_T + Q_{SW} + Q_{LH} - Q_{PLW} \tag{12}$$

Precipitation that falls as rain or accumulated snow (section 2.2) that melts on land, is returned instantaneously to the ocean. The total runoff for a river basin is then divided between specified points (river outflows) and an even distribution along the basin's coastal points (see Fig. 2).

Orography is felt by the atmosphere in four ways (see Fig. 3). A globally-averaged lapse rate is used to

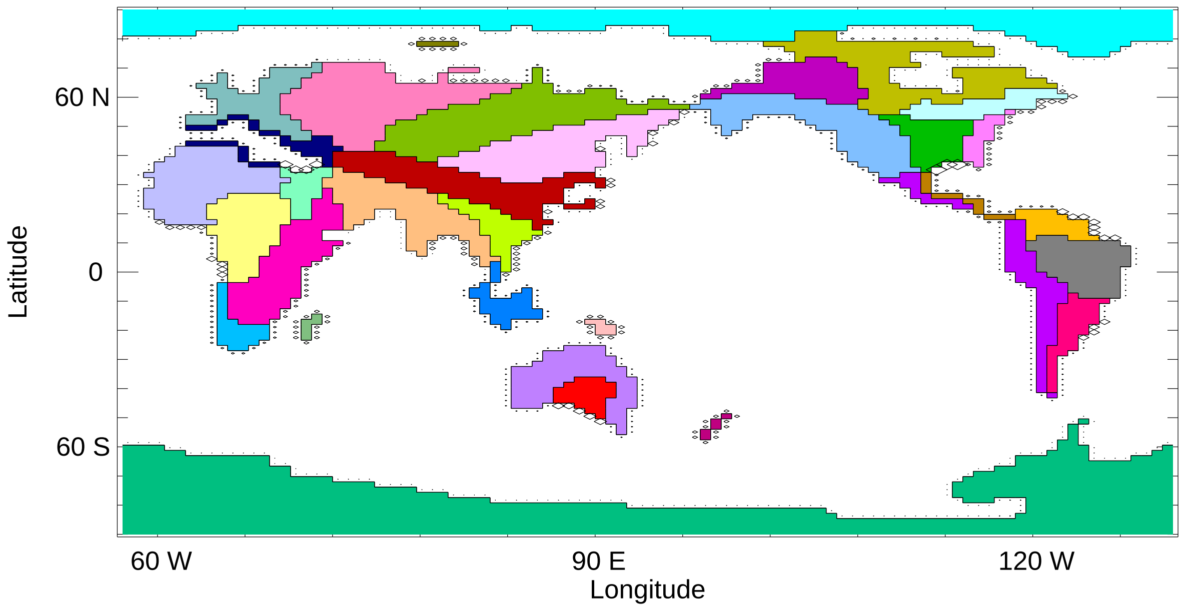

Figure 2: River drainage basins. Outlines indicate the 32 different river basins used and diamonds indicate discharge points. The size of the diamond indicates the proportion of total basin precipitation that is discharged at the point. Latitudes and longitudes are in the rotated coordinate system.

reduce the model's apparent sea level temperature in calculating the following: the outgoing long wave radiation; the surface air temperature (SAT) dependent planetary co-albedo through the calculation of the areal fraction of terrestrial snow/ice; the saturation specific humidity to determine the amount of precipitation; whether the precipitation will fall as rain or snow. A beneficial consequence of adding orography is that realistic river basins can be used (compare Fig. 2 with Fig. 1 of Weaver et al. (1998)). Using the reduced temperature for calculating outgoing radiation makes the long wave radiation more dependent on topography than is seen in the observations, but it improves the simulated surface temperatures, which are otherwise generally too low over areas of high elevation.

The model includes a full annual cycle of solar insolation for both present and past orbital configurations (Berger (1978)). As such, it is capable of being used for both equilibrium paleoclimate applications (e.g., Weaver et al. (1998)) or long transient paleoclimate integrations (e.g., Weaver et al. (2000)). A monthly wind stress climatology, created from 40 years (1958–1998) of daily Kalnay et al. (1996) reanalysis data, is used to force the ocean and ice components of the coupled model. This wind stress climatology is also converted to wind speeds for use in the calculation of latent and sensible heat fluxes between the atmosphere and ice or ocean models.

2.1.1 Parametrisation of wind stress anomalies

It has been suggested (Schiller et al. 1997; Fanning and Weaver 1997b) that the dynamic response of the atmosphere to SST anomalies has a stabilising effect on the Atlantic thermohaline circulation. In order to account for

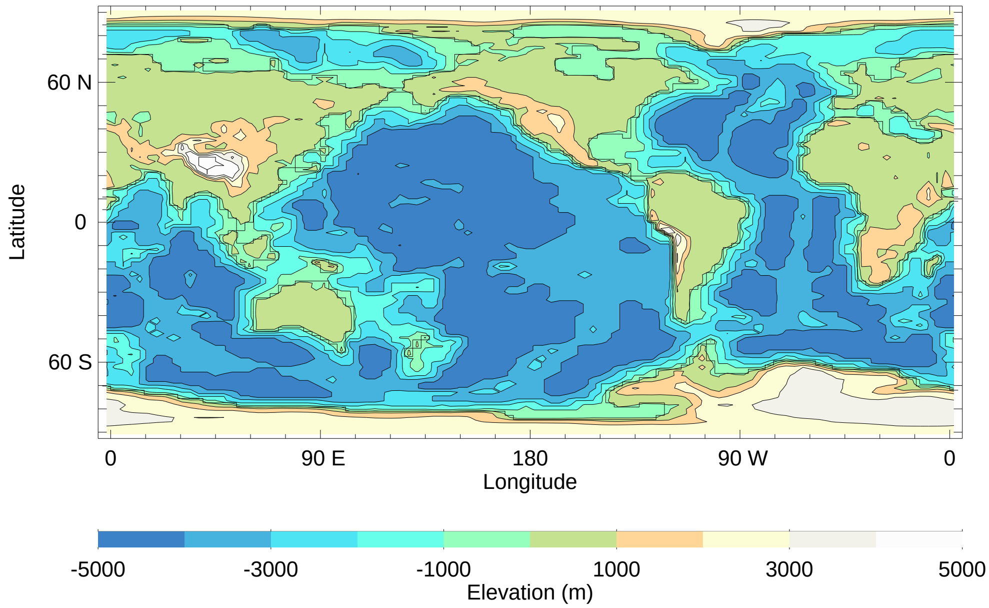

Figure 3: Land elevations and ocean depths. Contours are every 1000 m. Latitudes and longitudes are in the rotated coordinate system.

this effect in our non dynamic energy-moisture balance model we follow the idea of Fanning and Weaver (1997b) and parametrise wind stress anomalies in terms of SAT anomalies. The starting point for this parametrisation is a linear approximation between the density ρ and air temperature T_a near the surface:

$$\rho = a + bT_a. \tag{13}$$

As an example we show values of ρ and T_a at 45° N from the mean seasonal cycle of the 15 year ECMWF-reanalysis data Gibson et al. (1997) (abbreviated as ERA15) in Fig. 4. The correlation is similarly high at all other latitudes (not shown).

Using the equation of state for dry air it is now possible to express the sea-level pressure p in terms of air temperature T_a:

$$p = R\rho T_a = R(aT_a + bT_a^2), \tag{14}$$

where $R = 287$ Jkg^{-1}K^{-1} is the gas constant for dry air. We use the geostrophic approximation, with Rayleigh damping near the equator, for the calculation of the near surface wind velocities as follows:

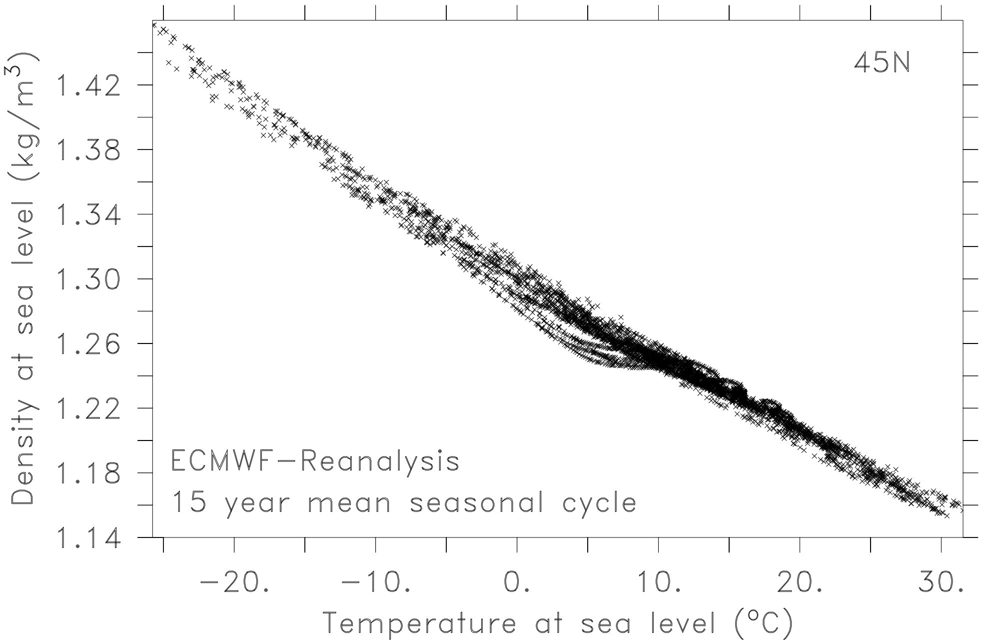

Figure 4: Near surface air density versus near surface air temperature at 45^o N from ERA15.

$$
\begin{aligned}
-fv + \frac{1}{\rho_a r_e \cos\phi}\frac{\partial p}{\partial \lambda} + \frac{u}{\tau} &= 0 \qquad (15)\\
fu + \frac{1}{\rho_a r_e}\frac{\partial p}{\partial \phi} + \frac{v}{\tau} &= 0 \qquad (16)
\end{aligned}
$$

where $\mathbf{V} = (u, v)$ is the wind velocity vector, and

$$
\frac{1}{\tau} = \frac{1}{\tau_0} exp[-(\phi/15^o)^2] \qquad (17)
$$

Here $r_e = 6370$ km is the radius of the Earth, ϕ is the latitude, and λ is the longitude and $f = 2\Omega\sin(\phi)$ is the Coriolis parameter ($\Omega = 7.29 \times 10^{-5}$ s^{-1}is the Earth's rotation rate). The damping coefficient $\tau_0 = 3600$ s in Eq. (17) is assumed to be constant at all latitudes, although the entire Rayleigh damping term becomes negligible outside of the tropics. Solving Eqs. 15 and 16 for the geostrophic velocities yields

$$
\begin{aligned}
u &= \frac{1}{(f^2 + 1/\tau^2)\,\rho_a}\left(-\frac{1}{\tau r_e \cos\phi}\frac{\partial p}{\partial \lambda} - \frac{f}{r_e}\frac{\partial p}{\partial \phi}\right) \qquad (18)\\
v &= \frac{1}{(f^2 + 1/\tau^2)\,\rho_a}\left(\frac{f}{r_e \cos\phi}\frac{\partial p}{\partial \lambda} - \frac{1}{\tau r_e}\frac{\partial p}{\partial \phi}\right) \qquad (19)
\end{aligned}
$$

Surface wind velocities $\mathbf{V}_s$ are calculated through a rotation and contraction of the wind velocity vector as described in Fanning and Weaver (1997b), namely

$$\mathbf{V}_s = C_t \begin{pmatrix} \cos\psi & -\sin\psi \\ \sin\psi & \cos\psi \end{pmatrix} \mathbf{V}$$

where $C_t = 0.8$ is a contraction factor and $\psi = 20°$ is a rotation angle (positive in the northern hemisphere and negative in the southern hemisphere). The wind stress vector $\boldsymbol{\tau}$ can then be derived from the bulk formula Gill (1982)

$$\boldsymbol{\tau} = c_D \rho_a \left|\mathbf{V}_s\right| \mathbf{V}_s \tag{20}$$

where $c_D = 1 \times 10^{-3}$is a constant dimensionless drag coefficient.

While one could use this wind stress approximation to provide mean winds, we only use it to calculate anomalous wind feedbacks that are then added to the mean observational wind field. That is, the model is integrated to equilibrium with specified present-day winds. Any perturbation away from the present climate allows us to calculate SAT anomalies, and hence surface pressure anomalies (Eq. 14) . These surface pressure anomalies then allow us to calculate anomalous wind (Eqs. 18, 19) and hence wind stress (Eq. 20) anomalies which are added to the specified mean fields. This procedure leads to a first order approximation of dynamical feedbacks associated with changing winds in a changing climate.

In the following we present an evaluation of this parametrisation using results from an atmospheric GCM, in which wind velocities are explicitly computed. Initial tests showed that the use of global constants for the parameters a and b in Eq. 13 lead to results which were not entirely satisfactory, mainly due to the fact that small errors in a and b lead to relatively large errors in the calculation of sea-level pressure in Eq. 14. We therefore allowed a and b to be a function of latitude, but not time. Their values at different latitudes as calculated from the mean seasonal cycle from ERA15 are shown in Fig. 5. In order to estimate the uncertainty in a and b, we also recalculate them using NCEP reanalysis data. While small differences exist (Fig. 5), the general form of the curves is remarkably similar for both reanalysis products.

For the evaluation we use sea-level pressure and near surface temperature output from two runs (equilibrium control and $2 \times CO_2$ simulations) conducted using the CCCma second generation atmospheric GCM (McFarlane et al. 1992), coupled to a mixed layer ocean model. Geostrophic (frictional near the equator) velocities were computed from Eqs. 18 and 19 using the GCM sea-level pressure data, and compared with the velocities arising from the parametrised sea-level pressure field obtained from Eq. 14 using the GCM near surface temperature

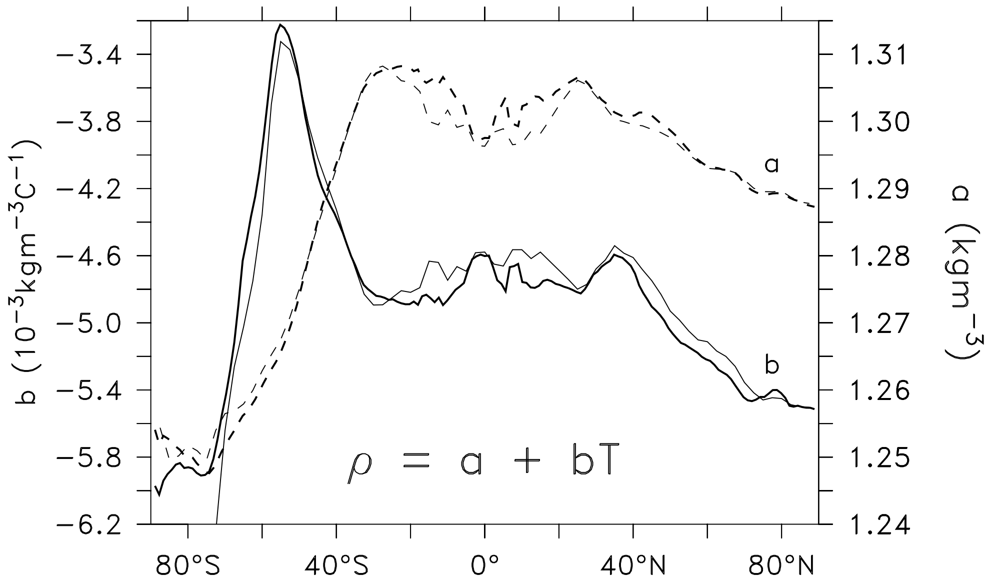

Figure 5: Latitudinal profiles of slope b (solid, left scale) and intercept a (dashed, right scale) for the parametrisation of surface air density as calculated by a linear regression from ERA15 (thick lines) and NCEP (thin lines).

data as input. We did this for both the ERA15- and NCEP-derived values of a and b, although subsequent sections only use the ERA15 version of the parametrisation. Figure 6 shows the zonally-averaged differences in geostrophic velocities between the $2\times$ CO_2 and control climates over each of the three major ocean basins, as well as over the total ocean. The parametrised geostrophic wind anomalies capture many of the large scale features of the anomalous geostrophic GCM wind fields, although the amplitude of the parametrised field is too large for u in the southern ocean. These differences highlight the limitations of the parametrisation although the general shape of the curves is reasonably captured. Differences in the results from the NCEP- and ERA15-derived parametrisations are, in general, much smaller than their respective differences from the GCM wind field. Errors in the calculated surface wind stress would be larger due to the quadratic dependence of wind stress on the wind velocity in Eq. 20. Nevertheless, with these limitations in mind, we suggest that the parametrisation represents a first order approximation of atmospheric wind feedbacks on the ocean circulation both through changes in sensible and latent heat exchange and changes in wind stress. The comparison of the red and green curves in Fig. 6 allows us to also argue that uncertainty in the physical basis of the parametrisation is much larger than uncertainty in the individual constants a and b.

Figure 6: Geostrophic (frictional near the equator) wind velocity anomalies for a doubling of CO_2. Zonal (upper four panels) and meridional (lower four panels) velocities were zonally averaged over the individual ocean basins and smoothed with a 10° sliding window to suppress small scale variability. Parameters a and b Eq. 13 are derived from ERA15 (red lines) and NCEP (green lines).

2.2 Atmosphere-Ocean-Sea Ice Coupling and the Sea Ice and Snow Subcomponent Models

Our ESCM of intermediate complexity includes several options for the representation of sea ice thermodynamics and thickness distribution. We start this section with a discussion of the standard sea ice model which involves simple two-category (sea ice, open water) thermodynamics (section 2.2.1.1) and elastic-viscous plastic dynamics (section 2.2.1.2). Other more sophisticated thermodynamic components have been developed such as a multi-layer thermodynamic model with heat capacity (Bitz and Lipscomb 1999) and thickness distribution (Holland et al. 2001; Bitz et al. 2001). The more sophisticated thermodynamical treatment is discussed in section 2.2.2 and the more sophisticated thickness distribution options are discussed in section 2.2.3.

2.2.1 The standard sea ice model

2.2.1.1 Thermodynamics The standard representation of thermodynamics in the sea ice model is the relatively simple zero layer formulation of Semtner (1976), with the lateral growth and melt parametrisation of Hibler (1979). This assumes that the ice has no heat capacity and that the surface temperature is in instantaneous balance with the external forcing. The model predicts ice thickness (H_i), areal fraction (A_i) and ice surface temperature (T_i). The ice dynamics (section 2.2.1.2) uses the elastic viscous plastic rheology developed by Hunke and Dukowicz (1997).

The change in ice thickness over a grid cell is given by,

$$\frac{\partial H_i}{\partial t} = \frac{(Q_b - Q_t)}{\rho_i L_f} - \frac{\rho_o}{\rho_i} E - L(H_i) \tag{21}$$

where Q_b is the heat flux from the ocean, Q_t is the heat flux from the atmosphere (Q_t and Q_b are assumed to be positive downward), $\rho_i = 913$ and $\rho_o = 1035$ kgm^{-3} are representative values for the ice and water densities, respectively, $L_f = 3.34 \times 10^5$ J kg^{-1} is the latent heat of fusion of ice, E is sublimation given by Equation 9 and $L(H_i)$ is horizontal advection of H_i (Appendix B).

Since grid cells are allowed to be partially ice-covered, the total heat flux from the atmosphere is calculated for both the open water (Q_{to}) and ice covered (Q_{ti}) portions such that:

$$Q_t = (1 - A_i)Q_{to} + A_i Q_{ti} \tag{22}$$

where A_i is the areal fraction of ice . Over the ocean:

$$Q_{to} = Q_{SW}(1 - C_A) - Q_{LW} - Q_{SH} - \rho_o L_\nu E \tag{23}$$

and similarly over ice:

$$Q_{ti} = Q_{SW}(1 - C_A) - Q_{LW} - Q_{SH} - \rho_o L_s E \tag{24}$$

where L_s is the latent heat of sublimation.

The heat flux from the ocean is calculated according to McPhee (1992)

$$Q_b = c_h u_\tau (T_f - T_o)\rho_o C_{po} \tag{25}$$

where $c_h = 0.0058$ is an empirical constant, u_τ=0.02 ms^{-1} is the skin friction velocity, $C_{po} = 4044$ Jkg^{-1}K^{-1} is the specific heat of sea water under ice at constant pressure. Note that Eq. 25 is equivalent to relaxing the temperature of the uppermost ocean grid box, with thickness $\Delta z = 50$ m, to the salinity-dependent freezing point $T_f(S_o)$, with a timescale of 5 days (here S_o is the salinity at the uppermost ocean level). The change in ice areal fraction depends on the growth rates over ice-covered and open water areas.

$$\begin{aligned}\frac{\partial A_i}{\partial t} = & \begin{cases} \frac{(1-A_i)}{H_0}\frac{(Q_b - Q_{to})}{\rho_i L_f} & \text{if } Q_{to} < Q_b \\ 0 & \text{otherwise} \end{cases} \\ + & \begin{cases} \frac{A_i}{2H_i}\left(\frac{(Q_b - Q_t)}{\rho_i L_f} - \frac{\rho_o}{\rho_i}E\right) & \text{if } Q_t > Q_b \\ 0 & \text{otherwise} \end{cases} \\ - & \quad L(A_i) \end{aligned} \tag{26}$$

where $H_0 = 0.01$ m is a demarcation thickness between thick and thin ice.

The first term on the right hand side of Eq. 26 parametrises the change in area under freezing conditions, where the open water portion $(1 - A_i)$ exponentially decays with time constant $H_0\rho_i L_f/(Q_b - Q_{to})$. The second term parametrises melting and assumes that all ice is uniformly distributed in thickness between 0 and $2H_i/A_i$. Assuming uniform melting over time $\triangle t$, this term opens up area where thickness is less than $-(\frac{(Q_b - Q_t)}{\rho_i L_f} - E)\triangle t$.

The surface temperature is calculated by equating the conductive flux through the ice (and snow) with the energy flux at the surface

$$\frac{T_i - T_f}{\frac{H_i}{I_{cond}} + \frac{H_s}{S_{cond}}} = Q_{ti}(T_i) \tag{27}$$

where $I_{cond} = 2.166\ \mathrm{Wm^{-1}K^{-1}}$ is a constant ice conductivity (and H_s and $S_{cond} = 0.31\ \mathrm{Wm^{-1}K^{-1}}$ are the thickness and conductivity of snow respectively). The maximum value of T_i is limited to the freezing temperature.

2.2.1.2 Dynamics The ice dynamics are governed by the momentum balance:

$$m\frac{\partial \mathbf{u}}{\partial t} = \nabla \cdot \sigma - mf\mathbf{k} \times \mathbf{u} + \boldsymbol{\tau}_a + \boldsymbol{\tau}_w - mg\nabla H \tag{28}$$

where m is the ice mass per unit area, $\mathbf{u}$ is the ice velocity, σ is the internal stress tensor, f is the Coriolis parameter, $\mathbf{k}$ is the unit normal vector in the vertical, $\boldsymbol{\tau}_a$ and $\boldsymbol{\tau}_w$ are the atmospheric (wind) and oceanic stresses, H is the sea surface dynamic height, $g = 9.81\ \mathrm{ms^{-2}}$ is the acceleration due to gravity. Ice acceleration and nonlinear advection terms are neglected. The internal stress tensor is solved from the elastic viscous plastic constitutive law described by Hunke and Dukowicz (1997):

$$\frac{1}{E}\frac{\partial \sigma_{ij}}{\partial t} + \frac{1}{2\eta}\sigma_{ij} + \frac{\eta - \zeta}{4\eta\zeta}\sigma_{kk}\delta_{ij} + \frac{P}{4\zeta}\delta_{ij} = \dot{\epsilon}_{ij} \tag{29}$$

where E is Young's modulus (dependent on model resolution), η and ζ are shear and bulk viscosities (which depend on $\dot{\epsilon}_{ij}$ and P), P here is the pressure (which is a function of ice thickness and area), δ_{ij} is the Kronecker delta and $\dot{\epsilon}_{ij}$ is strain rate tensor. This formulation adds an elastic component to the viscous plastic rheology described by Hibler (1979). It approximates the viscous-plastic solution on timescales associated with the wind forcing through the inclusion of artificial elastic waves that allow for an efficient numerical solution technique using an explicit timestep.

The oceanic stress is given by:

$$\begin{aligned} \boldsymbol{\tau}_w = \quad & \rho_o C_w |\mathbf{U}_w - \mathbf{u}|[(\mathbf{U}_w - \mathbf{u})\cos\theta \\ + \quad & \mathbf{k} \times (\mathbf{U}_w - \mathbf{u})\sin\theta] \end{aligned} \tag{30}$$

where $C_w = 0.0055$ is the water drag coefficient, $\mathbf{U}_w$ are the geostrophic ocean currents and $\theta = 25^\circ$ is a turning angle. The tilt term $-mg\nabla H$ is calculated using geostrophy and approximating $\mathbf{U}_w$ by the second ocean level velocities

2.2.2 Snow

Precipitation falls as snow when the SAT (reduced with elevation at a prescribed lapse rate) falls below a critical value (usually $-5\,^{\circ}$C). Snow allows for storage of moisture over land and, if complete melt does not occur, can be used as a primitive (non-dynamic) ice sheet model. Snow is not only important in creating a seasonal runoff but its presence also changes the value of the planetary albedo. The albedo is smoothly changed when the SAT falls below the critical value for snowfall (-5°C) and reaches it's maximum at $-10\,^{\circ}$C. The albedo is also changed smoothly with the depth of snow, reaching a maximum when the average snow depth reaches 1 m. Over land, snow melt occurs once the SAT reaches the critical value for snowfall and melts at a rate of 0.5 cm day^{-1} $^{\circ}$C $^{-1}$. The latent heat used to melt snow is taken from the atmosphere (see Eq. 4 with P interpreted as snow melt). Once snow accumulation reaches more than 10 m, the model treats any further accumulation as rain. Optionally, for paleoclimate simulations snow thickness may be accumulated over land (up to some thickness limit).

Over sea ice snow is treated as part of the surface energy balance (Eq. 27) with heat from the atmosphere preferentially melting snow and heat from the ocean preferentially melting ice. If all of the ice melts or there is no ice, snow is converted to water and placed in the ocean, with the necessary latent heat coming from the atmosphere. If the weight of accumulated snow is sufficient to push the ice-snow interface below the ocean surface, then the snow that would otherwise be submerged is converted to ice.

2.2.3 Other Sea Ice Model Options

2.2.3.1 Ice thickness Distribution (ITD) A sub-gridscale ITD (Thorndike et al. 1975) is incorporated into the model using the formulation of Hibler (1980) and Flato and Hibler (1995). This allows an arbitrary number of ice thickness categories within each model grid cell. The thermodynamic evolution of each category is independent of other categories with different fluxes computed at the ice/ocean and ice/atmosphere interfaces. The thickness distribution function is defined following Thorndike et al. (1975) as

$$\int_{h_1}^{h_2} g(h)dh = \frac{1}{\Gamma}\gamma(h_1, h_2) \tag{31}$$

where Γ is the total area of some fixed region, and $\gamma(h_1, h_2)$ is the area within Γ covered by ice of thickness h in the range $h_1 \leq h < h_2$. This distribution evolves according to

$$\frac{\partial g(h)}{\partial t} = -\nabla \cdot (\mathbf{u}g) - \frac{\partial}{\partial h}(f_g g) + \Psi + F_L, \tag{32}$$

where here f_g is the thermodynamic growth rate and F_L is the modification of the ITD due to lateral melting. Ψ, the "redistribution" function, describes how ice is redistributed among the various thickness categories due for example to deformation events in which thin ice is ridged into thicker categories. A detailed description of the formulation of this function can be found in Flato and Hibler (1995). The compressive strength of the ice cover is computed as a function of the ITD, following Rothrock (1975). A description of the theory and numerical method used to solve for the compressive strength is discussed in Hibler (1980).

2.2.3.2 Ice Thickness Distribution and Multi-layer Thermodynamics Another formulation of the ice-thickness distribution of Thorndike et al. (1975) has been developed with the UVic ESCM by Bitz et al. (2001) in which each category has a single thickness of ice which varies in response to ice growth/melt, advection, and deformation. This ice thickness distribution model has more in common with that shown in Rothrock (1986) where the interpolation process was eliminated and each category was allowed to vary freely in thickness for a one-year simulation. The number of categories is limited by constraining each category to lie between lower and upper thickness limits that are fixed. When a category outgrows its limits, the ice is transfered from one category to another, where it is merged with ice that may already exist by conserving volume, energy, and area.

The thickness-distribution, $g(h)$, for M categories is written

$$g(h) = g_0\delta(h) + \sum_{i=1}^{M} g_i\delta(h - H_i) \tag{33}$$

where M is the number of ice categories, $\delta(h)$ is the Dirac delta function, and g_i is the concentration within category i (category 0 is open water). The evolution of horizontal ice concentration and ice volume per unit area, V_i, for each category is governed by a pair of continuity equations

$$\frac{\partial g_i}{\partial t} = -\nabla \cdot (\mathbf{u} g_i) + \Psi_i + \mathcal{G}_i \tag{34}$$

and

$$\frac{\partial V_i}{\partial t} = -\nabla \cdot (\mathbf{u} V_i) + \Theta_i + \mathcal{V}_i, \tag{35}$$

respectively, where $\mathbf{u}$ is the velocity of the ice, Ψ_i and Θ_i are contributions by mechanical redistribution (Thorndike et al. 1975), and $\mathcal{G}_i$ and $\mathcal{V}_i$ are contributions by thermodynamic processes. Employing a vertical coordinate that is normalised by the sea ice thickness, $z_i^* = z/h_i$, the energy of melting, $E_i(z_i^*)$ evolves according to

$$\frac{\partial E_i}{\partial t} = -\nabla \cdot (\mathbf{u} E_i) + \Pi_i + \mathcal{E}_i, \tag{36}$$

where $\Pi_i(z_i^*)$ is the contribution by mechanical redistribution and $\mathcal{E}_i(z_i^*)$ is the contribution by thermodynamic processes.

Vertical heat conduction and storage in the sea ice are governed by the heat equation. The vertical temperature profile is resolved in the ice in roughly 50 cm intervals, so the number of vertical layers N_i for category i depends on the thickness limits for that category. Following Bitz and Lipscomb (1999), the amount of energy needed to melt a unit volume of sea ice with salinity S at temperature T in Celsius, is equal to

$$q(S,T) = \rho_i c_i(-\mu S - T) + \rho_i L_f \left(1 + \frac{\mu S}{T}\right), \tag{37}$$

where $c_i = 2054$ Jkg^{-1}K^{-1}and $L_f = 3.34 \times 10^5$ Jkg^{-1}K^{-1}are the heat capacity and latent heat of fusion for fresh ice and $\mu = 0.054$°C psu^{-1} is the empirical constant from the linear approximation relating the melting temperature and the salinity of sea ice $T_m = -\mu S$. Thus the energy of melting for layer l in category i in Eq. 36 is

$$E_{i,l} = q(S_{i,l}, T_{i,l}) \frac{V_i}{N_i} \tag{38}$$

In Eqs. 37 and 38, the salinity profile is specified to vary from 0 ‰ at the top to 3.2 ‰ at the bottom according to the observations of Schwarzacher (1959), but the ice is assumed to be fresh for purposes of computing the freshwater exchange between sea ice and the atmosphere or ocean. For more details see Bitz et al. (2001).

2.2.4 Continental Ice Dynamics Model and Coupling Strategy

Our ESCM includes the continental ice dynamics model (CIDM) that was developed at the University of British Columbia (Marshall 1996; Marshall and Clarke 1997ab). The reader is referred to Yoshimori et al. (2001) for a detailed evaluation of its performance and an application to the last glacial termination. Generally, glaciers can move due to the superposition of three mechanisms: 1) internal deformation of ice (creep); 2) basal sliding; and 3) subglacial sediment (bed) deformation (Alley 1989; Paterson 1994). Flow in most regions of an ice sheet is through internal deformation, whereas ice streams and surge lobes flow by the last two mechanisms. The CIDM models the first mechanism based on the vertically-integrated mass balance equation and three dimensional momentum equations under the shallow ice approximation, in which the flow is approximated as vertical shear deformation with no horizontal shear deformation (Hutter 1983 1993). As an ice rheology in the constitutive equations, the traditional Glen's flow law is employed in which ice is treated as nonlinear (power law) viscous material (Glen 1955 1958; Paterson 1994).

To investigate first-order continental ice dynamics and the coupled influence of land ice on the climate, we adopt a simple approach. Ice is approximated as isothermal and the vertically-integrated mass balance equation is written as

$$\frac{\partial H_i}{\partial t} + \nabla_h \cdot (\overline{\mathbf{v}}_h H_i) = M \tag{39}$$

where H_i is ice thickness, $\overline{\mathbf{v}}_h$ is the vertically-averaged horizontal velocity, M is the net accumulation, t is time, and ∇_h is a horizontal gradient operator. The vertically-integrated horizontal volume flux is written as

$$\overline{\mathbf{v}}_h H_i = -\frac{2A(T)}{n+2}(\rho_i g)^n H_i^{n+2} \left|\nabla_h h_s\right|^{n-1} \nabla_h h_s \tag{40}$$

where ρ_i is ice density, g is the gravitational acceleration, h_s is the surface elevation. The flow law exponent n of Glen's flow law is set to be 3, which is typical for ice sheet studies (Paterson 1994). Therefore, the volume flux varies with ice thickness to the power 5 and surface slope to the power 3. Also, the flow law coefficient is given by

$$A(T) = mA_0 e^{(-Q/RT)} \tag{41}$$

where T is the ice temperature, R is the ideal gas constant, A_0 is $1.14 \times 10^{-5}\mathrm{Pa}^{-3}\mathrm{yr}^{-1}$ ($T < 263.15\mathrm{K}$) and $5.47 \times 10^{10}\mathrm{Pa}^{-3}\mathrm{yr}^{-1}$ ($T \geq 263.15\mathrm{K}$), and Q, the activation energy, is $60\mathrm{kJmol}^{-1}$ ($T < 263.15\mathrm{K}$) and $139\mathrm{kJmol}^{-1}$ ($T \geq 263.15\mathrm{K}$). The enhancement factor m accounting for the softening of ice due to impurities, meltwater, and crystal fabric is set to be 3 (van de Wal 1999). We use a uniform (effective) ice temperature of -15°C representative of the lower ice column, where most internal deformation occurs. Although this value is too cold and makes the ice too stiff in some regions, it is a reasonable average of warm- and cold-based regions within ice rheology uncertainties.

In general, the bedrock responds to the varying ice load through an elastic deformation of the lithosphere and a viscous flow in the asthenosphere. The resulting uplift and depression of the bedrock is approximated by local displacement of mantle material, and neglect of the lithosphere flexure. A local response type isostatic adjustment is applied, in which the response is relaxed to a local isostatic equilibrium:

$$\frac{\partial h_b}{\partial t} = -\frac{1}{\tau}\left(h_b + r_\rho H_i - h_b^0\right) \tag{42}$$

where h_b is the bedrock elevation, $r_\rho = 0.277$ is the ratio of ice density to bedrock density, h_b^0 is the undisturbed (ice-free) equilibrium bedrock elevation, and τ is the relaxation time set to be 3,000 years here (Peltier and Marshall 1995; Tarasov and Peltier 1997).

We do not permit basal sliding or ice stream development and as a first step we use the same resolution in the CIDM as the climate model ($3.6° \times 1.8°$), although we are working towards refining the resolution of the ice sheet model and sub-grid scale topographic effects on ice sheet evolution. Our current resolution is rather coarse for the proper representation of ice dynamics and mass balance, particularly in marginal-ice regions. However, this resolution permits easy and consistent coupling with the climate model, while providing a first look at the coupled problem.

In nature, ice accumulation occurs through snowfall, deposition of water vapour from the atmosphere (negligible), refreezing of melt water, and freezing of rain, while ice depletion occurs by sublimation, surface or basal melting, and calving in the ocean. For simplicity, we assume the dominant factors are snowfall, surface melting and calving. Snowfall and surface melting are provided by the atmospheric model and we assume instantaneous calving and subsequent melting over the ocean, i.e., no ice is allowed over the ocean except sea ice.

Because of the slow response time of ice sheets relative to other climate system components, an asynchronous coupling strategy is adopted. When coupled, we integrate the climate model for 10 years, average the net surface accumulation over this period, and pass it to the CIDM as a boundary condition. The CIDM is then integrated for 2,000 years with a 10 year time step and the average ice thickness and surface elevation are returned to the climate model. This cycle is repeated until both models reach steady state.

As our ice sheet model is currently used only for equilibrium paleoclimate simulations, all precipitation occurring over land in the atmospheric model is passed instantaneously into the oceanic component (Fig. 2) regardless of whether it is rain or snow. This differs from the case where the climate model is run without the interactive CIDM, where snow remains on land until it melts. As mentioned above, to allow for ice sheet growth the net snow accumulation is passed to the CIDM, although no melt water is passed to the oceanic component since the original source of the melt water (i.e., snow) is already passed to the ocean model when it falls on land. This is to avoid making the ocean unstable through massive freshwater discharge owing to the asynchronous coupling which could allow the ice to be transported and piled up in an incompatibly warm location. The atmospheric model has no limitation on the amount of surface melting as long as ice exists. Therefore, it is possible that the ice accumulated in the 2,000 year CIDM integration segment could melt away during one atmosphere/ocean/sea ice model integration segment (10 years). This strategy also allows arbitrary initial conditions for ice thickness. For example, this prevents the oceanic component becoming unstable due to flooding even when the LGM ice sheets are imposed as an initial condition in an incompatibly warm climate, which is inevitable for sensitivity experiments under perpetual forcing.

In summary, the net surface accumulation is calculated in the atmospheric model and passed to the CIDM. Ice thickness is then calculated in the CIDM and passed to the atmospheric model. There is no direct exchange of freshwater between the CIDM and the oceanic component. As a result, the total amount of moisture is strictly conserved within the climate model. Therefore, the model does not yet include the effects of the melt water discharge on the ocean circulation, nor the effects of changes in continental ice volume on the ocean mean salinity. This latter issue is dealt with through modifying the initial global mean ocean salinity, according to proxy reconstructions, prior to integrating the model to equilibrium.

With these limitations in mind, it is very satisfying to find that simulated and observed present-day ice sheets agree well (Fig. 7) in both hemispheres (Yoshimori et al. 2001), although we tend to slightly overestimate their thickness. The maximum ice thickness near the Greenland summit is 3867 m in the model and about 3050 m in the observed field, whereas near Vostok in Antarctica, the simulated field is 4753 m thick versus 4150m in observation. Differences between observed and simulated fields tend to be larger near margins due to the course-resolution of our CIDM and hence its inability to capture sharp surface slopes there. These maximum values can be reduced easily by changing the ice dynamics flow parameter, although we have shown figures here that are consistent with those in Yoshimori et al. (2001).

2.3 Ocean Model

The ocean component of the coupled model is the GFDL Modular Ocean Model version 2.2 (Pacanowski 1995). MOM is based upon the Navier Stokes equations subject to the Boussinesq and hydrostatic approximations. The momentum and tracer equations in spherical geometry are:

$$\begin{aligned} \frac{\partial u}{\partial t} = & \frac{-1}{\rho_o r_e \cos\phi}\frac{\partial p}{\partial \lambda} + \frac{\partial}{\partial z}\left(A_v \frac{\partial u}{\partial z}\right) + \mathcal{F}(A_h, u, v) \\ + & \frac{uvtan\phi}{r_e} + fv - L(u) \end{aligned} \tag{43}$$

$$\begin{aligned} \frac{\partial v}{\partial t} = & \frac{-1}{\rho_o r_e}\frac{\partial p}{\partial \phi} + \frac{\partial}{\partial z}\left(A_v \frac{\partial v}{\partial z}\right) + \mathcal{F}(A_h, v, -u) \\ - & \frac{u^2 tan\phi}{r_e} - fu - L(v) \end{aligned} \tag{44}$$

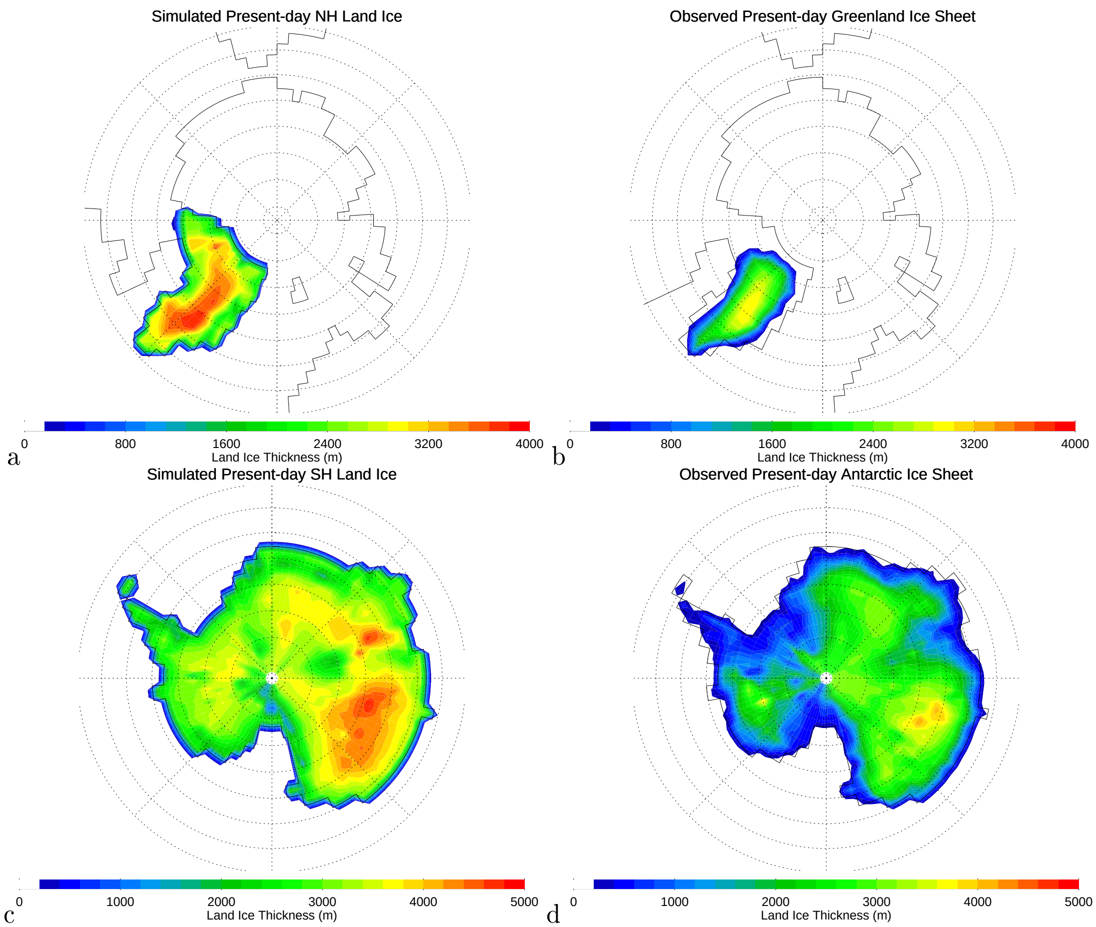

Figure 7: Comparison between observed (b and d) and simulated (a and c) present-day ice sheets for the northern hemisphere (a and b) and southern hemisphere (c and d).

$$\frac{\partial T}{\partial t} + L(T) = \frac{\partial}{\partial z}\left(k_v \frac{\partial T}{\partial z}\right) + \nabla(k_h \nabla T) \tag{45}$$

$$\frac{\partial S}{\partial t} + L(S) = \frac{\partial}{\partial z}\left(k_v \frac{\partial S}{\partial z}\right) + \nabla(k_h \nabla S) \tag{46}$$

$$\frac{\partial w}{\partial z} + \frac{1}{r_e \cos\phi}\left(\frac{\partial u}{\partial \lambda} + \frac{\partial (v\cos\phi)}{\partial \phi}\right) = 0 \tag{47}$$

$$\frac{\partial p}{\partial z} = -g\rho \tag{48}$$

where u, v, and w are the velocity components in the zonal, meridional and vertical directions respectively, f is the Coriolis parameter, r_e is the radius of the earth, p is the pressure, ρ_o is a representative density for sea water, t is time, g is the acceleration due to gravity, and $A_v = 1 \times 10^{-3}\mathrm{m}^2/\mathrm{s}$ is the vertical eddy viscosity. $\mathcal{F}$ is the horizontal Laplacian operator (Appendix B) representing the horizontal mixing of momentum given an eddy viscosity $A_h = 2.5 \times 10^5\mathrm{m}^2/\mathrm{s}$ and L is the advection operator (Appendix B). The ocean density ρ of sea water is a nonlinear function of potential temperature (T), salinity (S) and pressure (UNESCO 1981). A horizontal diffusivity of $k_h = 2 \times 10^3\mathrm{m}^2/\mathrm{s}$ and a modified form of the Bryan and Lewis (1979) vertical distribution of vertical diffusivity, ranging from $k_v = 6 \times 10^{-5}\mathrm{m}^2/\mathrm{s}$ in the thermocline to $k_v = 1.6 \times 10^{-4}\mathrm{m}^2/\mathrm{s}$ in the deep ocean, are used.

While the climatology discussed in section 3 is based on integrations using the standard horizontal/vertical diffusive approach, detailed sensitivity studies have also been done using different parametrisations of sub grid scale mixing. For example, the Gent and McWilliams (1990) parametrisation for mixing associated with mesoscale eddies, in which the diffusion tensor is rotated along isopycnals and isopycnal thickness diffusion is introduced to account for the removal of potential energy from the stratification due to baroclinic instability, has been shown to improve certain aspects of our model climatology (Robitaille and Weaver 1995; Wiebe and Weaver 1999; Duffy et al. 1999 2001). The model also incorporates a parametrisation of brine rejection during sea ice formation (Duffy and Caldeira 1997) that substantially improves our representation of Intermediate Water properties (Duffy et al. 1999 2001).

At the surface, the model is driven by both wind stress and surface buoyancy forcing. Since it is unphysical for ocean temperatures to fall below freezing, the ocean model always calculates the maximum amount of heat available in the first layer (Q_b; Eq. 25) which may be given to either the atmosphere or sea ice. The net heat Q_H and implied salinity Q_S fluxes into the ocean are then,

$$Q_H = (1 - A_i)Q_{to} + A_i Q_b \tag{49}$$

$$Q_S = \rho_o S^* (E - P - R + \frac{Q_b - Q_t}{\rho_o L_f}) \tag{50}$$

where $S^* = 34.9$ psu is a representative salinity for the ocean and R is the runoff from land. Here Q_{to}, Q_t and Q_b are given by Eqs. 23, 22 and 25, respectively, and all heat fluxes in Eqs. 49 and 50 are defined to be positive downward. As such, Q_b is always negative as the top level ocean temperature is always above the freezing point of water T_f (calculated according to Fofonoff and Millard (1983)).

The horizontal grid resolution is the same as that used in the atmosphere and sea-ice models and the vertical grid has 19 unequally spaced levels that vary smoothly in size, following a parabolic profile, from 50 m at the surface to 518 m at the deepest level (with bottom at 5396 m). The ocean bathymetry is taken from the Suarez and Takacs (1986) dataset. We used a raised cosine filter in both directions (latitude and longitude) to come up with a weighted-average for all of the bathymetry in a given grid box. In this approach, the data at the centre have the highest weight and the data at the edges have zero weight. In between, the weight is given a raised cosine functional form so that it slowly and smoothly varies from the highest weight until it approaches zero. The sum of the weights is normalised to 1.0. Five islands were included: Madagascar, Australia, New Guinea, New Zealand and Spitsbergen. An unrealistic hole in the Lomonosov Ridge that was present in the Suarez and Takacs (1986) dataset (near the pole) was filled such that the maximum depth along the ridge was 2000 m. Due to the coarse resolution of our model, and since we require at least two tracer points across a Strait for there to exist a baroclinic transport, Fram, Hudson, Madagascar and the Gibraltar Straits are all wider than in reality. Bering Strait is not open in the version of the model discussed here. Flow over deep sills, such as over the Greenland-Iceland-Faroes rise are fundamental to processes involved in North Atlantic Deep Water (NADW) formation. As we neither resolve the small-scale troughs through these sills, nor currently parametrise their effects, we had to deepen Denmark Strait to 700m and remove Iceland in order to improve the northward transport of heat in the North Atlantic.

2.4 Coupling

Coupling between the atmosphere-sea ice models and the ocean model is done every two ocean timesteps, by which time the atmosphere and sea ice have completed four time steps. In the ocean we use a longer timestep to integrate the tracer equations than the baroclinic velocity and barotropic vorticity equations. No timestep splitting with depth (Bryan 1984) is used.

Since each component uses a leapfrog time stepping scheme with an intermittent Forward Euler mixing time step, a special technique was used to calculate the fluxes exchanged between components to ensure that heat and fresh water were conserved exactly. If the number of time steps between mixing is limited to an even number, and the number of time steps that each subcomponent model completes between coupling is also an even number, then the average flux can be calculated by averaging the fluxes from every other time step (see Fig. 8). That is, only the fluxes that determined the final state of a particular subcomponent model at the timestep of coupling are averaged. Coupling in this manner is extremely useful in finding any potential conservation errors within and between models. As an example, we show the total globally-averaged difference in heat and equivalent freshwater from the initial condition in a 100 year run (Fig. 9). Unlike for salt and equivalent freshwater, which form a closed system in the model, heat is both gained from and lost to space. As such, the total heat calculation also subtracts off any net heat to/from space since the start of the run. A least square fit of the data shows a drift of about 1 TJ/100 years or 31 W (6×10^{-14} Wm^{-2}) for heat and about 0.5 Gg/100 years or 15 mg/s (3×10^{-14} mg/s/m^2) for fresh water, which is close to machine precision and most likely due to truncation error. In other words, the amount of drift globally in our coupled climate model is the equivalent of not accounting for a low wattage light bulb and a rapidly dripping faucet acting over the entire Earth's surface. Ensuring that at least two time steps were completed for any model before coupling also increased the stability of the coupled model permitting the use of longer time steps.

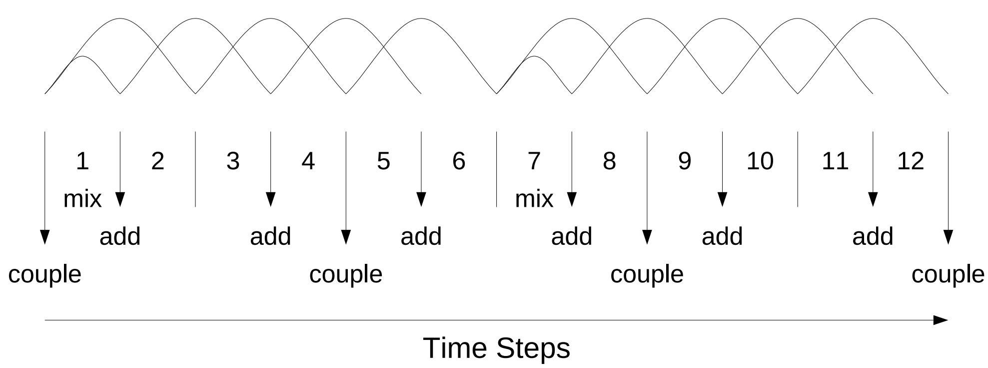

Figure 8: Exact flux coupling for a leapfrog time step scheme. "couple" indicates coupling times (every 4 time steps in this example); "add" are times when the fluxes are added to produce the average flux (every other time step); "mix" indicates a mixing time step (every 6 time steps in this example).

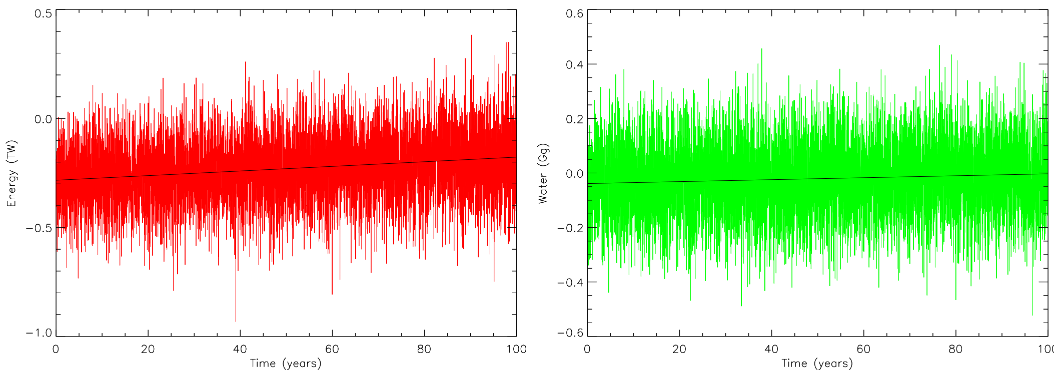

Figure 9: Model drift relative to the total energy (left) and fresh water (right) at the start of a 100 year run. Black lines indicate a linear least squares fit to the totals.

3 Present Day Climate Simulation

As noted earlier, the standard version of our ESCM uses the standard representation of sea ice (section 2.2.1) thermodynamics (section 2.2.1.1) and dynamics (2.2.1.2), as well as a diffusive representation for moisture transport. In this section we describe the control climatology of the ESCM under present-day radiative forcing. This typically involves 2000 years of integration by which time annually-averaged surface fluxes are close to zero. In the next section, we show the dramatic improvements that are realised when moisture transport is treated through advection instead of diffusion.

3.1 Atmosphere

The equilibrium (after 2000 years) present-day atmospheric SAT and its difference from the annually-averaged NCEP Kalnay et al. (1996) reanalysis climatology (Fig. 10), shows good agreement with observations, especially on the zonal mean (Fig. 10). The global and annual mean model SAT is 13.9 ^{o}C which differs from the NCEP climatology by only 0.12 ^{o}C, and a similarly reasonable agreement with NCEP reanalysis data is seen in the seasonal cycle (e.g., Table 1). Of course there are local regions in the model where differences are larger. For example, over land, Antarctica and most high elevation regions are cooler than NCEP while the northeast coast of North America and Asia are warmer. Some of this discrepancy may be attributed to our use of a constant atmospheric lapse rate (6.5 °C/km), but more likely the differences arise from our lack of vegetation and land surface feedbacks on SAT, as well as the lack of atmospheric dynamics (stationary waves, vertical motion etc. — but see section 4). That is, in our model, the planetary albedo is independent of land surface vegetation type and there is no latent or sensible heat exchange between the land and atmosphere.

Over the ocean, the North Atlantic is cooler than in the observations which, as we will discuss, is due to the slightly more extensive sea ice extent than is observed in this region. The latter arises from the fact that

NADW formation tends to occur slightly too far south, as is common in most ocean GCMs without an explicit representation of bottom boundary layers or a parametrisation for flow over sills. In the Southern Ocean, the model is slightly too warm, although this feature can be improved with the inclusion of the Gent and McWilliams (1990) parametrisation for mixing associated with mesoscale eddies (Duffy et al. 1999 2001).

Table 1: Coupled model simulations of globally-average SAT ranked by the average absolute error from observations Gates et al. (1996).

Surface air temperature (^{o}C)			
DJF	JJA	Error	Model
12.4	15.9		observations
12.3	15.7	0.15	UVic*
12.0	15.7	0.30	CCC
12.6	15.5	0.30	COLA*
12.1	15.3	0.45	CSIRO
13.0	15.6	0.45	GISS*
12.7	16.7	0.55	BMRC*
12.0	15.0	0.65	UKMO
11.0	15.2	1.1	MPI(LSG)
11.2	14.8	1.2	MPI(OPYC)
13.4	17.4	1.3	MRI
9.6	14.0	2.4	GFDL
15.5	19.6	3.4	NCAR*

*indicates a model without flux adjustments

As noted by Fanning and Weaver (1996), representing moisture advection as a diffusive process is a useful simplification in attempting to develop an idealised atmospheric model suitable for long-timescale paleoclimate sensitivity studies, as the gross features of the precipitation and evaporation fields can be captured. Nevertheless, this approach has serious shortcomings as highlighted in the fact that tropical moisture transport, through surface trade winds and their subsequent convergence on the equator, is actually an up-gradient process. As discussed in section 4 (see Fig. 23), we attempted to minimise these differences by allowing the moisture diffusion parameter to vary as a function of latitude.

When averaged globally, our total winter precipitation of 2.78 mm/day, and summer precipitation of 2.67 mm/day, is quite similar to both NCEP reanalysis data as well as the results from other coupled models (Table 2). Nevertheless, the two dimensional field is far too diffuse (Fig. 11a), even in the zonal average (Fig. 11c), to be considered an accurate representation of observations (Fig. 11b). Our representation of evaporation, which does not rely on unresolved atmospheric processes, bears much better resemblance to the observed field (Fig. 12), although it slightly overestimates evaporation in the subtropical gyres. When combined together (Fig. 13), the total evaporation minus precipitation field is more diffuse than in reality with the largest differences in the region of the Intertropical Convergence Zone where moisture transport is up-gradient and so can't be represented by a down gradient diffusive process.

a

b

c

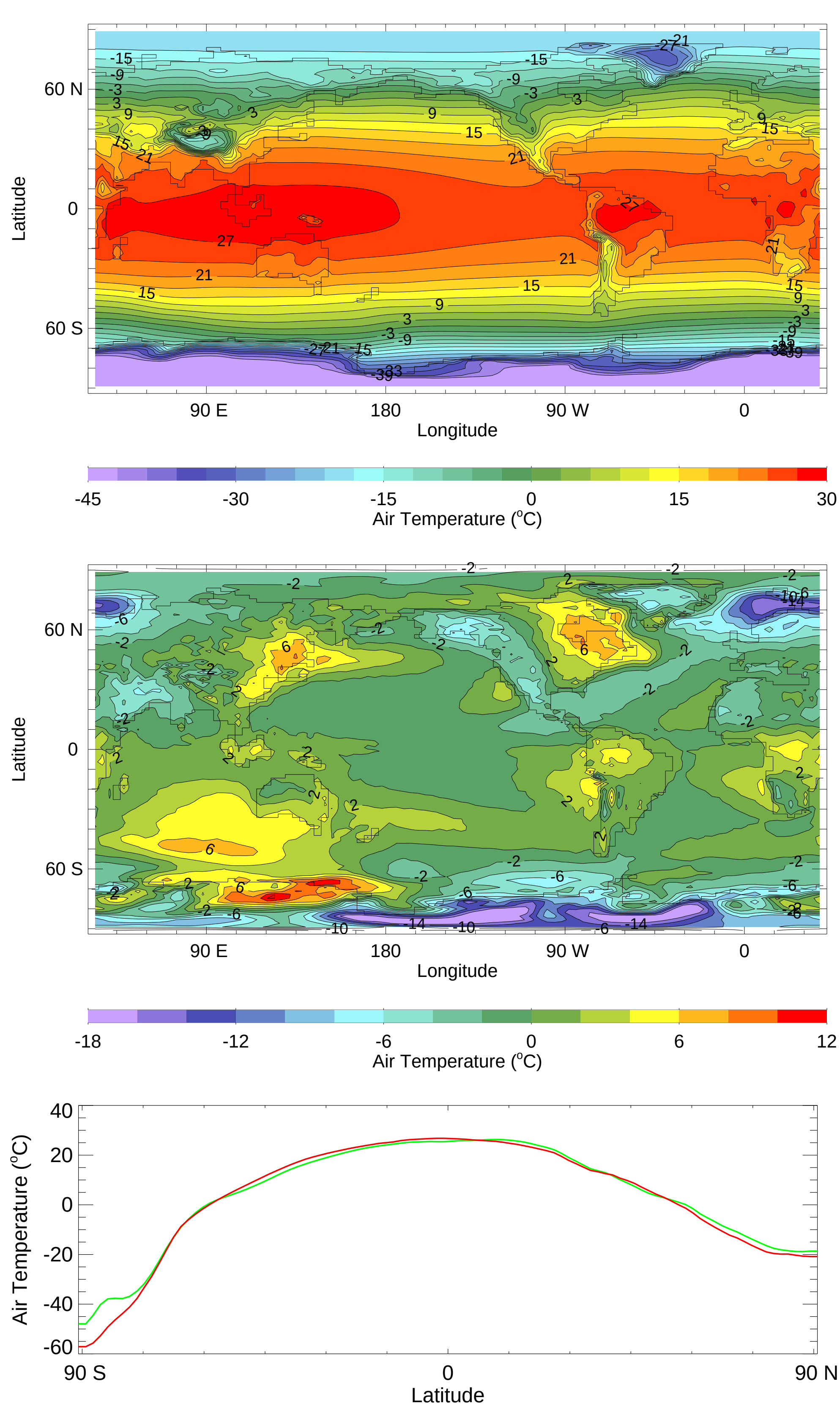

Figure 10: Annually-averaged surface air temperature from a) model, b) model-NCEP and c) zonally-averaged model (red) and NCEP (green) climatologies.

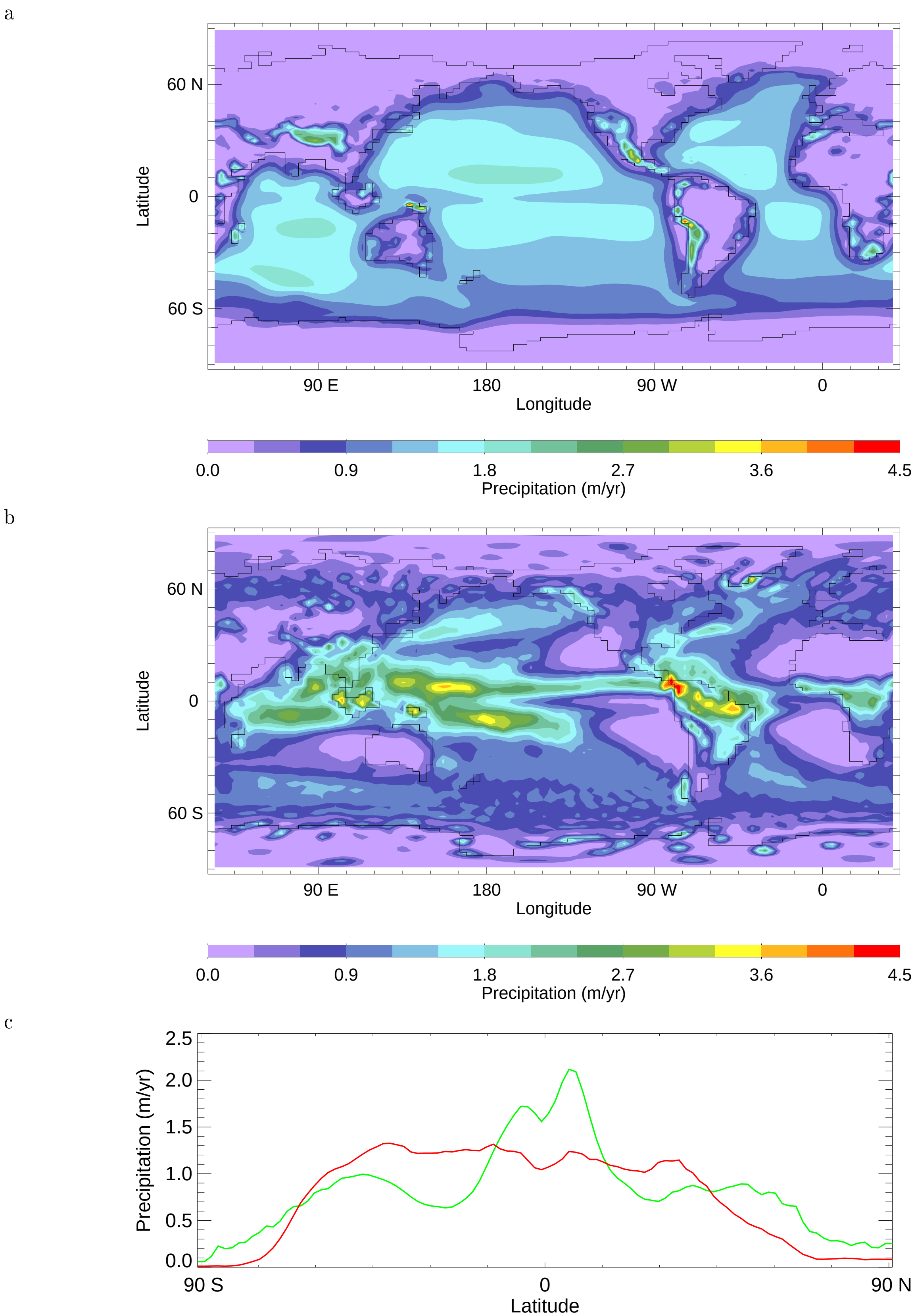

Figure 11: Annually-averaged precipitation from a) model, b) NCEP and c) zonally-averaged model (red) and NCEP (green) climatologies.

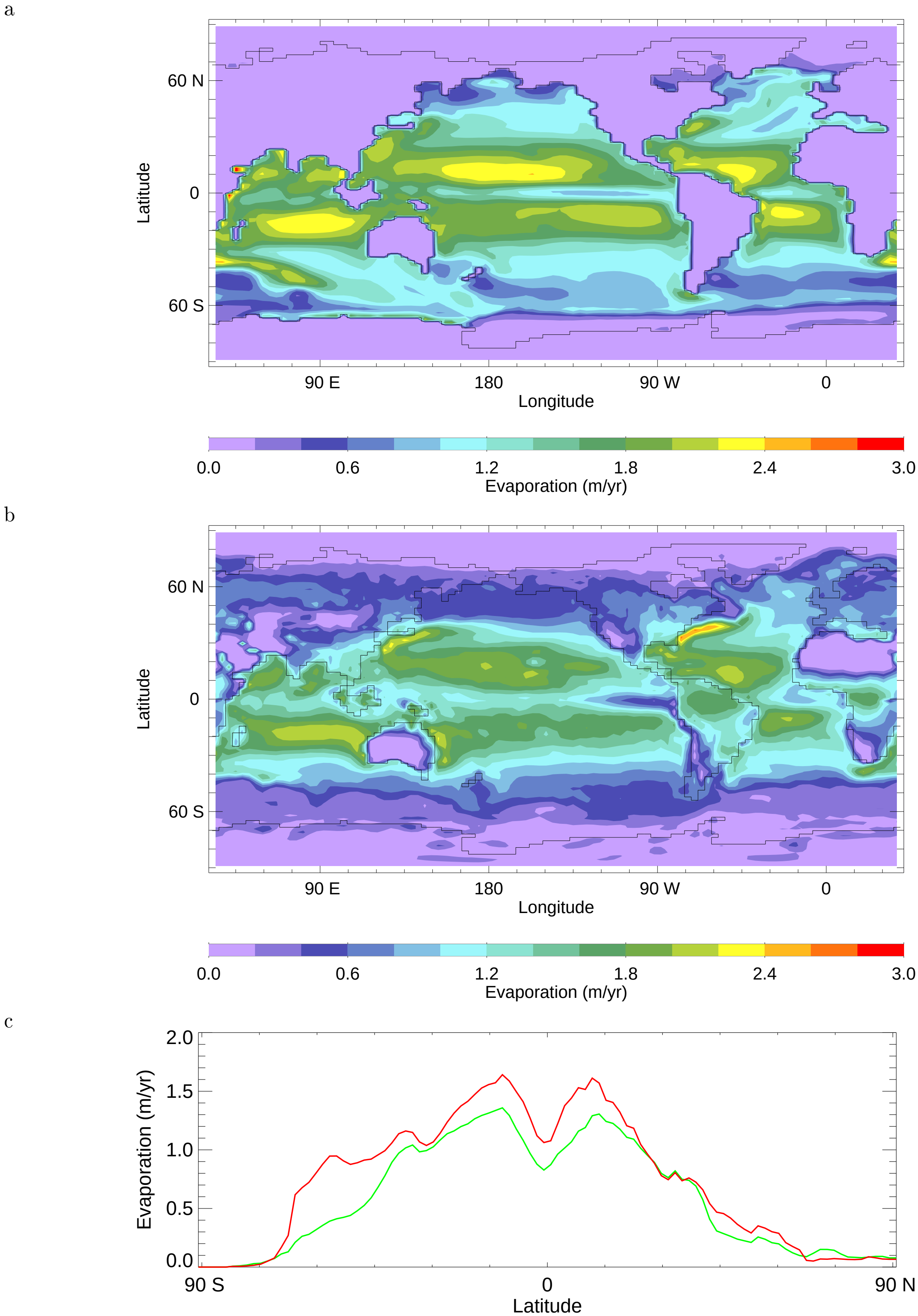

Figure 12: Annually-averaged evaporation from a) model, b) NCEP and c) zonally-averaged model (red) and NCEP (green) climatologies.

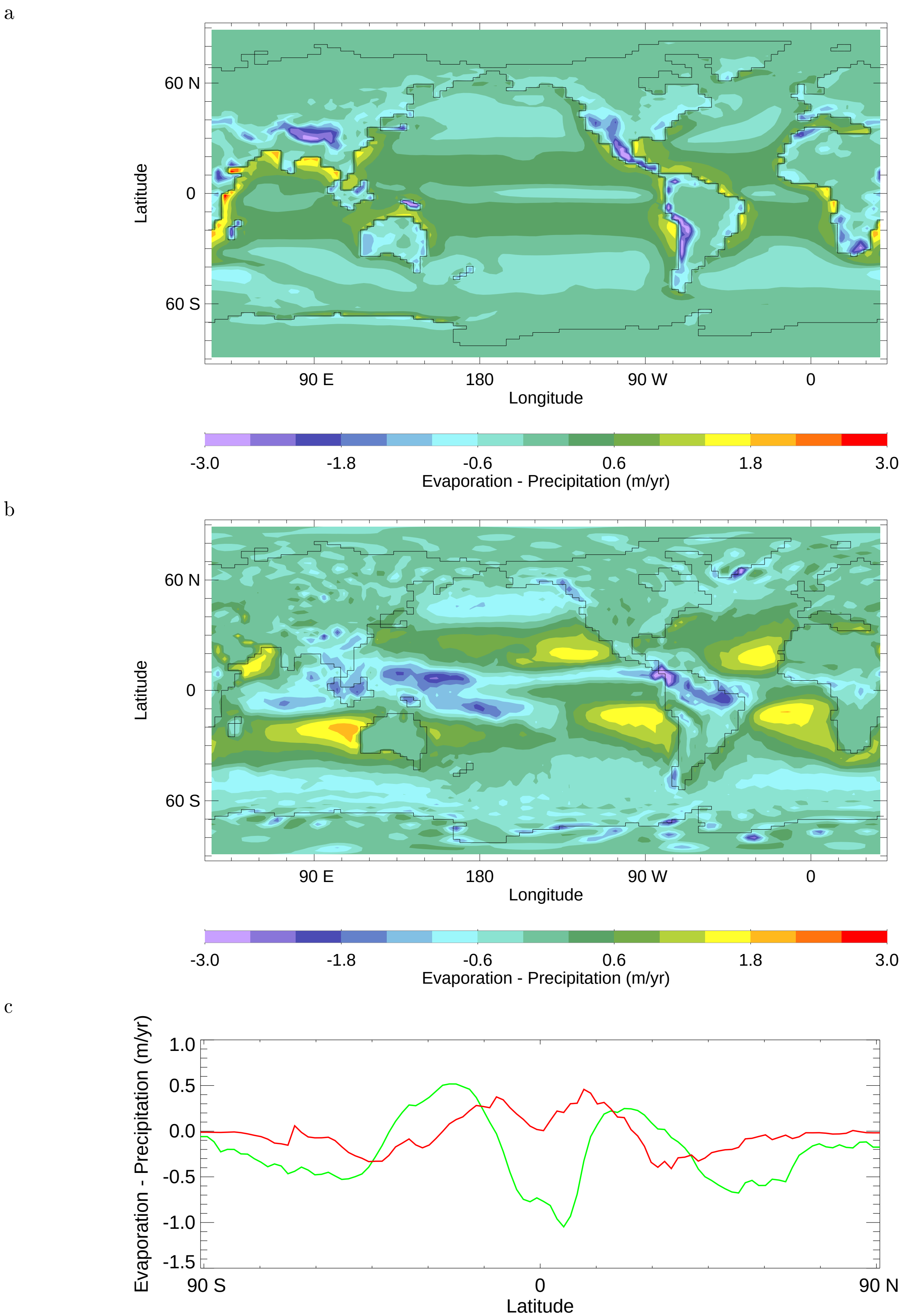

Figure 13: Annually-averaged evaporation minus precipitation from a) model, b) NCEP and c) zonally-averaged model (red) and NCEP (green) climatologies.

Table 2: Coupled model simulations of globally-averaged precipitation ranked by the average absolute error from observations Gates et al. (1996).

Precipitation (mm/day)			
DJF	JJA	Error	Model
2.74	2.90		observations
2.72	2.86	0.030	CCC
2.79	2.92	0.035	BMRC*
2.73	2.82	0.045	CSIRO
2.64	2.73	0.14	MPI(OPYC)
2.78	2.67	0.14	UVic*
2.89	3.03	0.14	MRI
2.64	2.67	0.17	COLA*
3.02	3.09	0.24	UKMO
3.14	3.13	0.32	GISS*
2.39	2.50	0.38	GFDL
3.78	3.74	0.94	NCAR*

*indicates a model without flux adjustments

3.2 Ocean

Over the ocean, the atmospheric surface temperature field shown in Fig. 10a is tightly coupled to the simulated SST field (Fig. 14a), although it is smoother as anomalies tend to be diffused away in the atmosphere. The simulated SST bears good agreement with the annual mean observations of Levitus and Boyer (1994) as illustrated in Fig. 14b, especially in the zonal mean (Fig. 14c), and the global average (18.3 °C, about 0.05 °C colder than that obtained from the Levitus climatology). Nevertheless, some large differences exist. In the southern Indian Ocean and near the mid-latitude coasts of the Pacific and Atlantic, simulated SSTs are too warm, while the Gulf of Alaska and Greenland-Iceland-Norwegian (GIN) Seas are too cold. The SST errors in the North Atlantic are largely attributable to the Gulf Stream separating too far north and not penetrating far enough into the GIN Seas to keep them ice free. Similarly in the Pacific, the Kuroshio separation is too far north and not enough warm water is reaching the Gulf of Alaska. These are common errors found in coarse resolution coupled models that do not employ flux adjustments.

The large positive difference between simulated and observed fields in the southern Indian Ocean is a consequence of the Antarctic Circumpolar Current being steered southward by the Kerguelen plateau and bringing relatively warm waters poleward. This tends to reduce the sea ice extent simulated off the coast of Antarctica between the African and Australian continents. The warmer than observed areas off the west coasts of North and South America as well as Africa, coincide with areas of known marine stratocumulous cloud formation in the atmosphere. These are not treated in our atmospheric model, nor well, if at all in atmospheric GCMs, and so we overestimate the amount of incident solar radiation at the ocean surface, leading to warmer than observed SSTs. The lack of a cloud scheme may also account for discrepancies in other areas too.

The simulated sea surface salinity (SSS) field (Fig. 15a) tends to be more uniform than observations (Figs.

a

b

c

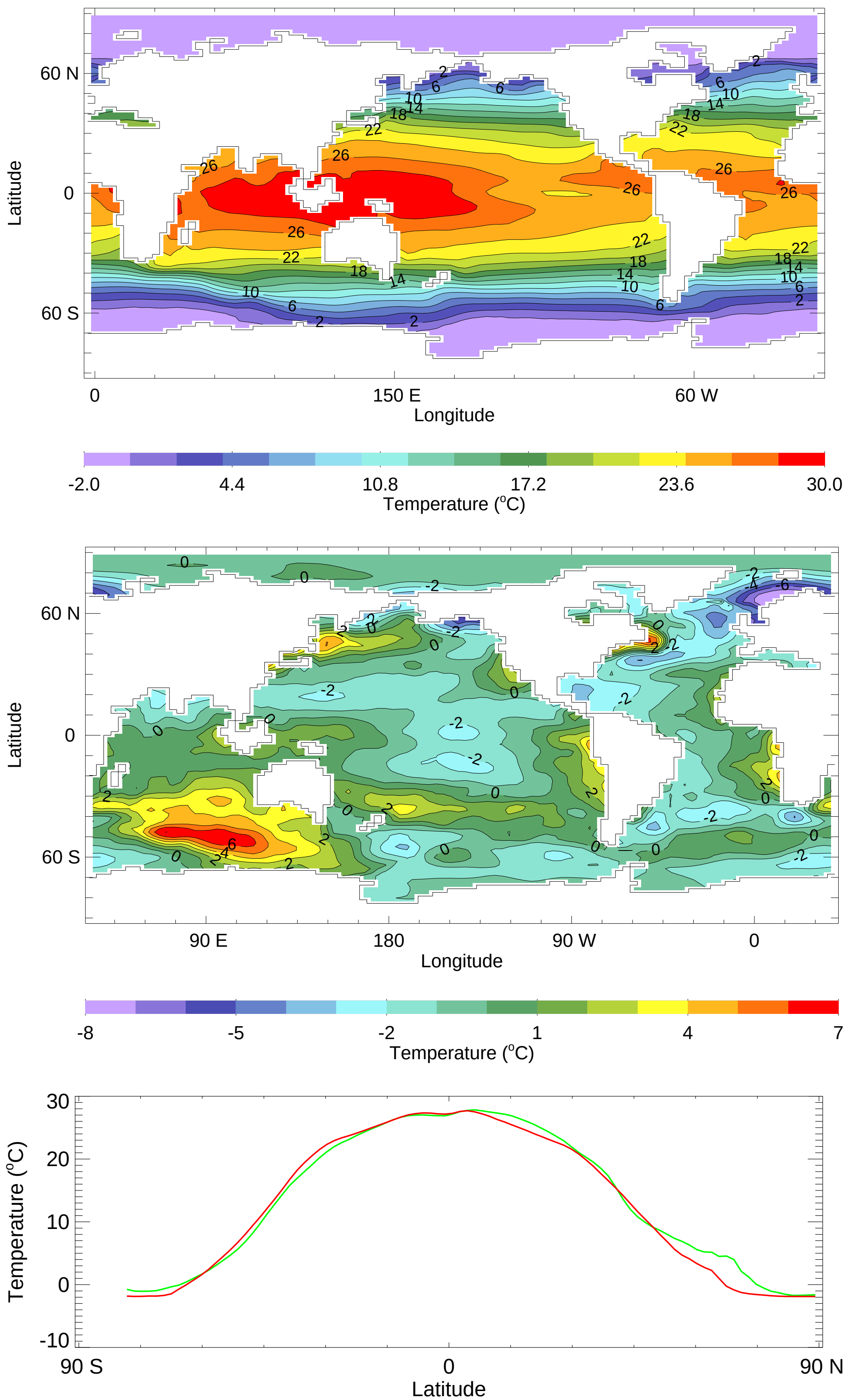

Figure 14: Annually-averaged sea surface temperature from a) model, b) model-Levitus and c) zonally-averaged model (red) and Levitus (green) climatologies.

15b,c), although the global average is similar (34.75 psu simulated — a difference of only 0.04 psu from the Levitus et al. (1994) climatology). The most significant differences arise in the middle of subtropical gyres, where simulated salinities are too fresh; in the Arctic, where simulated salinities are too large; in the GIN Sea region, where salinities are too fresh; in the Antarctic Circumpolar Current, where salinities are too large. As noted in the next section, the surface salinity errors found in the subtropical gyre regions and the Arctic are largely eliminated when moisture transport is accomplished through advection rather than through diffusion. This follows since high pressure centres tend to be associated with descending air and surface divergence, advecting moisture away from the region. The diffusive representation of moisture transport, on the other hand, always transports moisture down gradient and hence even into high pressure centres such as associated with the semipermanent subtropical and Arctic highs. The salinity discrepancy in the GIN Sea region is, as noted earlier, once more associated with our inability to effectively transport surface waters across the Iceland-Faroes ridge, leading to NADW formation occurring too far to the south. We hope to alleviate this problem through the development of a new bottom boundary layer parametrisation for flow over sills.

Finally, the saltier than observed waters in the Antarctic Circumpolar Current region arises from our use of a horizontal/vertical ocean diffusion scheme. Although not done in this standard version of our model, Robitaille and Weaver (1995), Duffy et al. (1999 2001), and Wiebe and Weaver (1999) showed that when the diffusion tensor is rotated along isopycnals, and the Gent and McWilliams (1990) parametrisation for mixing associated with mesoscale eddies is included, these discrepancies are greatly reduced. These parametrisations reduce spurious convection in the Southern Ocean, and so fresh surface waters are mixed less with more saline deeper waters. In addition, spurious meridional cross isopycnal diffusion of more saline subtropical waters into higher latitudes is eliminated. The net effect of including the GM parametrisation together with isopycnal mixing is to keep the surface ocean more fresh. Finally, as discussed in Duffy et al. (1999 2001), a more realistic treatment of brine rejection, in which salinity is mixed to depth (which depends on a prescribed density contrast) during the process of sea ice formation, improves the representation of the southern hemisphere water masses.

The global zonally-averaged potential temperature and salinity fields (Figs. 16 and 17, respectively) show features typical of coarse resolution ocean models which do not incorporate isopycnal mixing and the Gent and McWilliams (1990) parametrisation for mixing associated with mesoscale eddies. The thermocline is deeper than observed, so that positive potential temperature anomalies are evident (Fig. 16b). Similarly, in the subtropical gyre regions, which were too fresh at the surface (Fig. 15), subduction causes further freshening at depth (Fig. 17b). While the properties of the deep waters are reasonably well captured, the formation of relatively fresh, Antarctic Intermediate water (AAIW) is not well captured. As noted earlier and discussed in Duffy et al. (1999), AAIW formation is much better simulated when an improved parametrisation for sub-gridscale brine rejection,

a
b
c

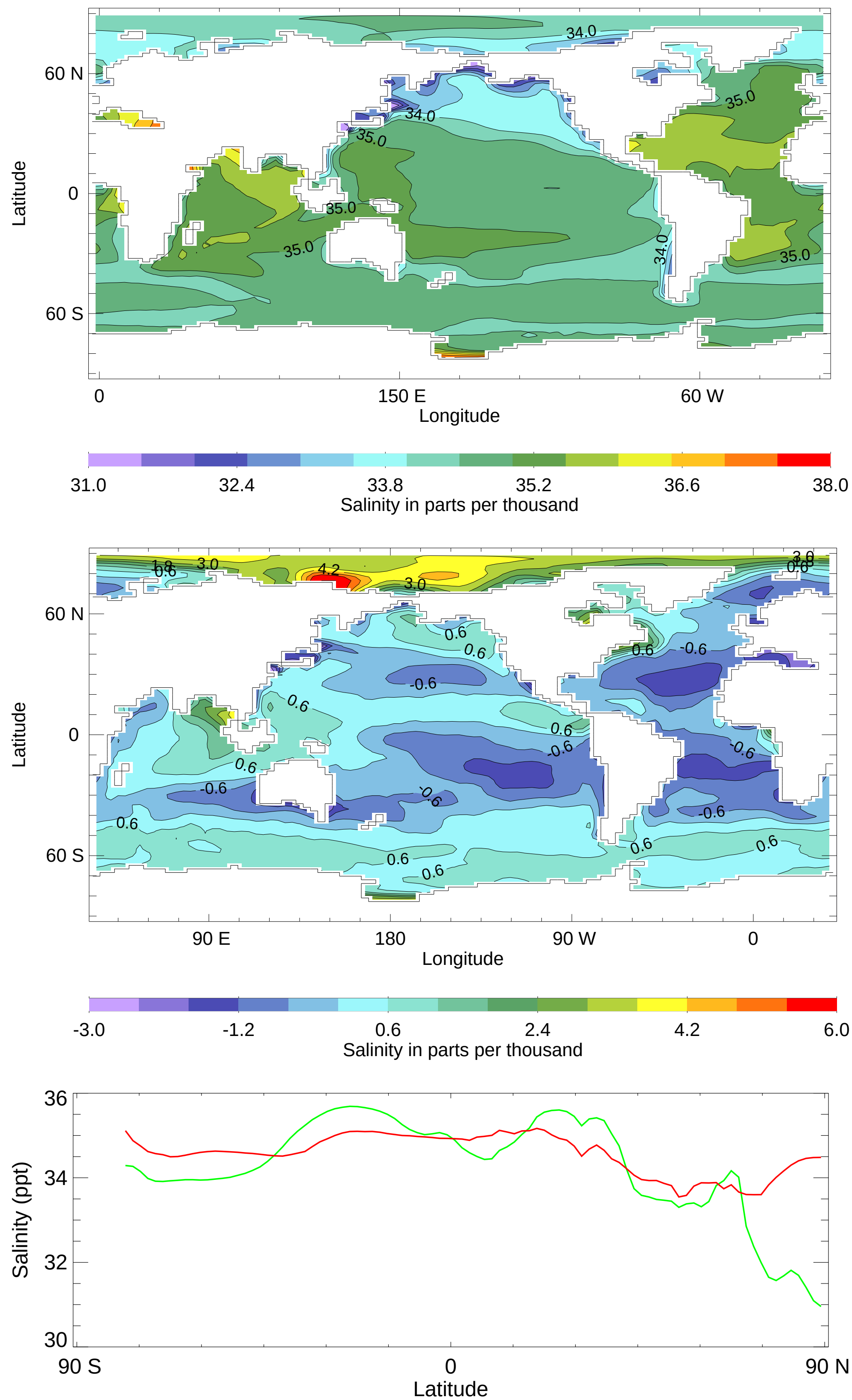

Figure 15: Annually-averaged sea surface salinity from a) model, b) model-Levitus and c) zonally-averaged model (red) and Levitus (green) climatologies.

that occurs during the formation of sea ice around Antarctica, is incorporated (see also section 3.4). As we will see in section 4, further improvements to the salinity distribution are realized when moisture transport is accomplished through advection rather than diffusion.

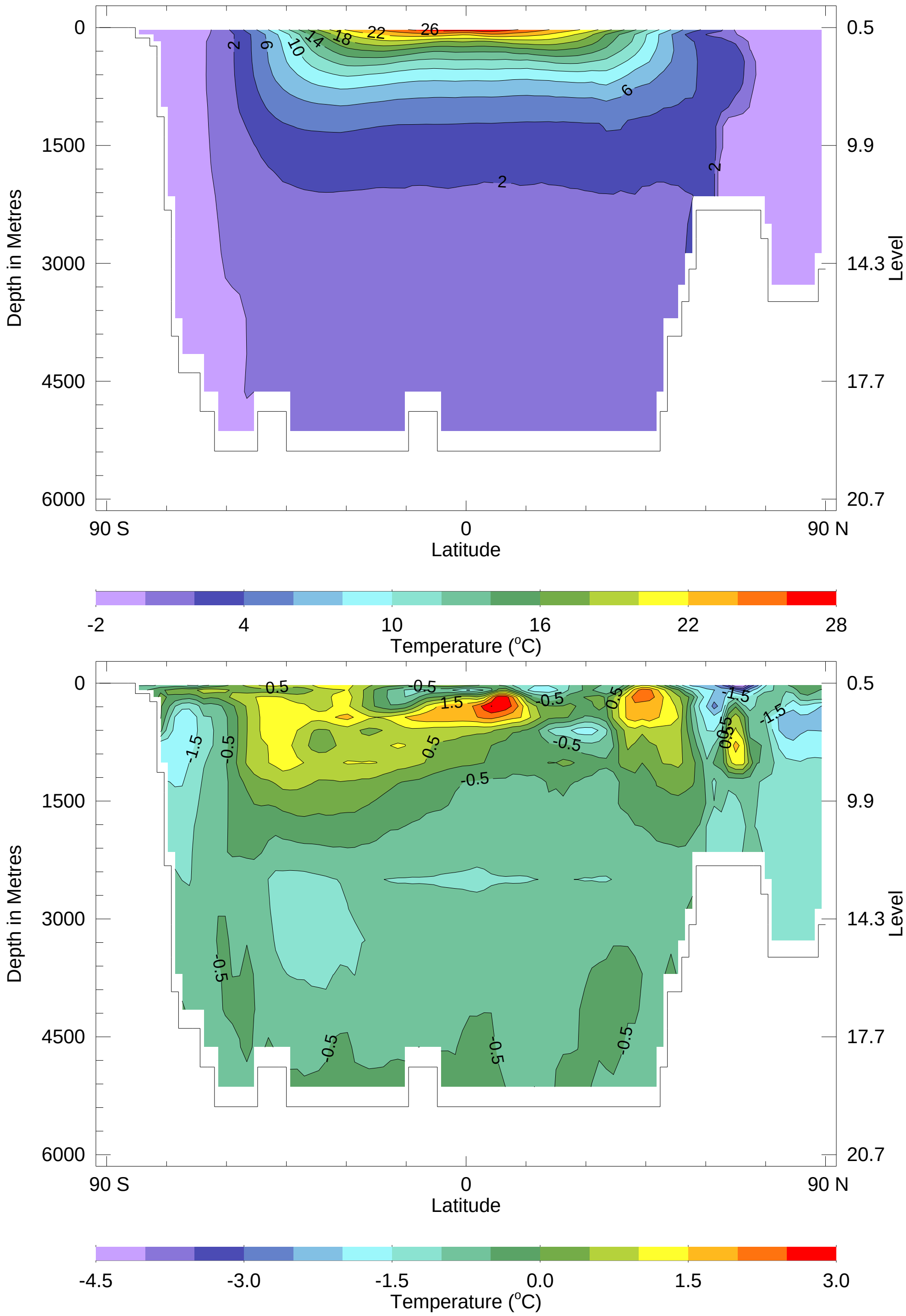

Figure 16: Annual mean zonally-averaged ocean potential temperature from a) model and b) model-Levitus climatologies.

a

b

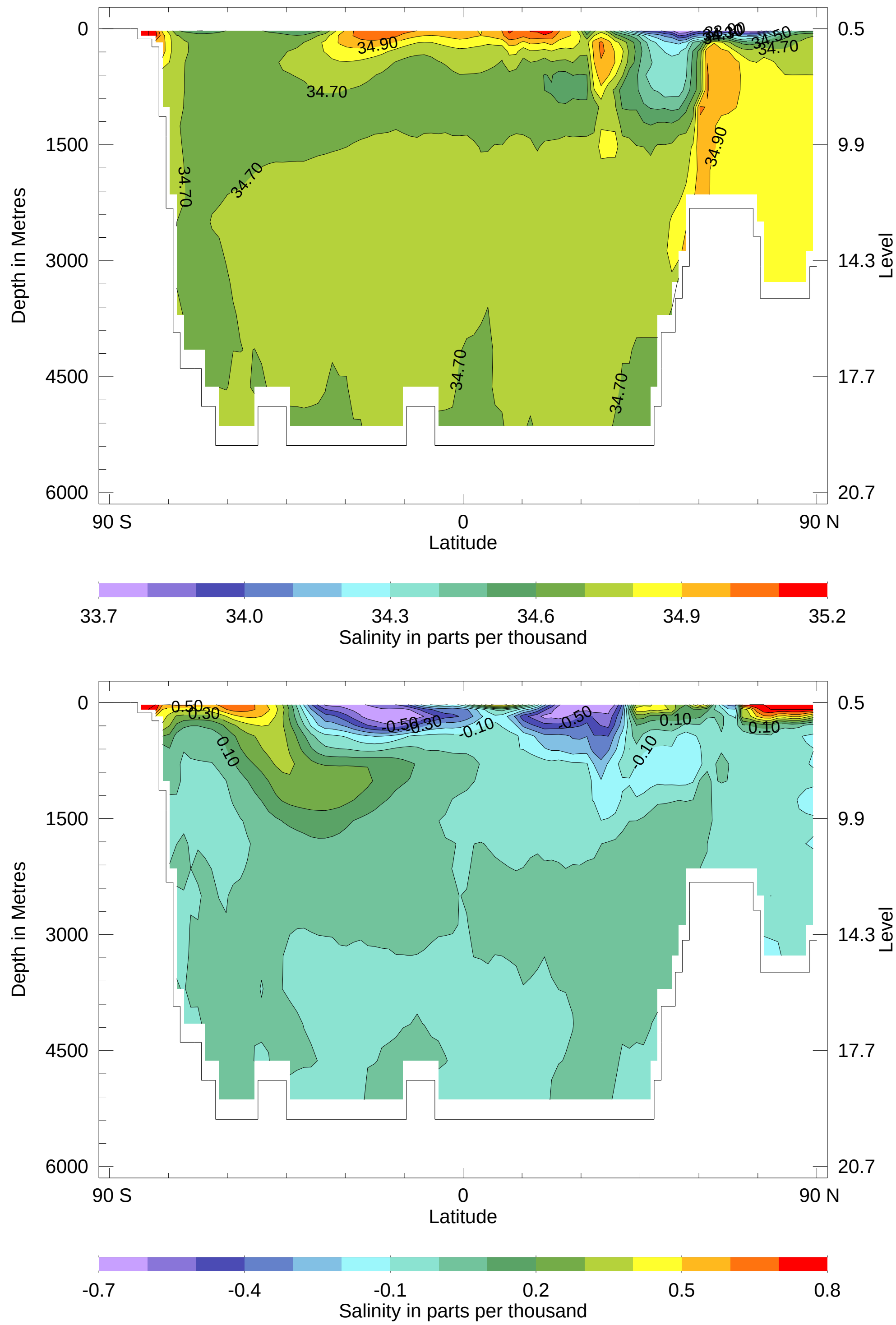

Figure 17: Annual mean zonally averaged ocean salinity from a) model and b) model-Levitus climatologies.

The meridional overturning in the Atlantic (Fig. 18a) indicates that about 18 Sv of NADW formation occurs in the model, although, as noted earlier, there is a tendency for it to form too far south. About 12 Sv of this NADW is transported across the Equator into the South Atlantic. AABW (Fig. 18b), formed in the Ross and Wedell Seas, extends to about 30°N, filling the deep North Atlantic up to a depth of about 3000 m.

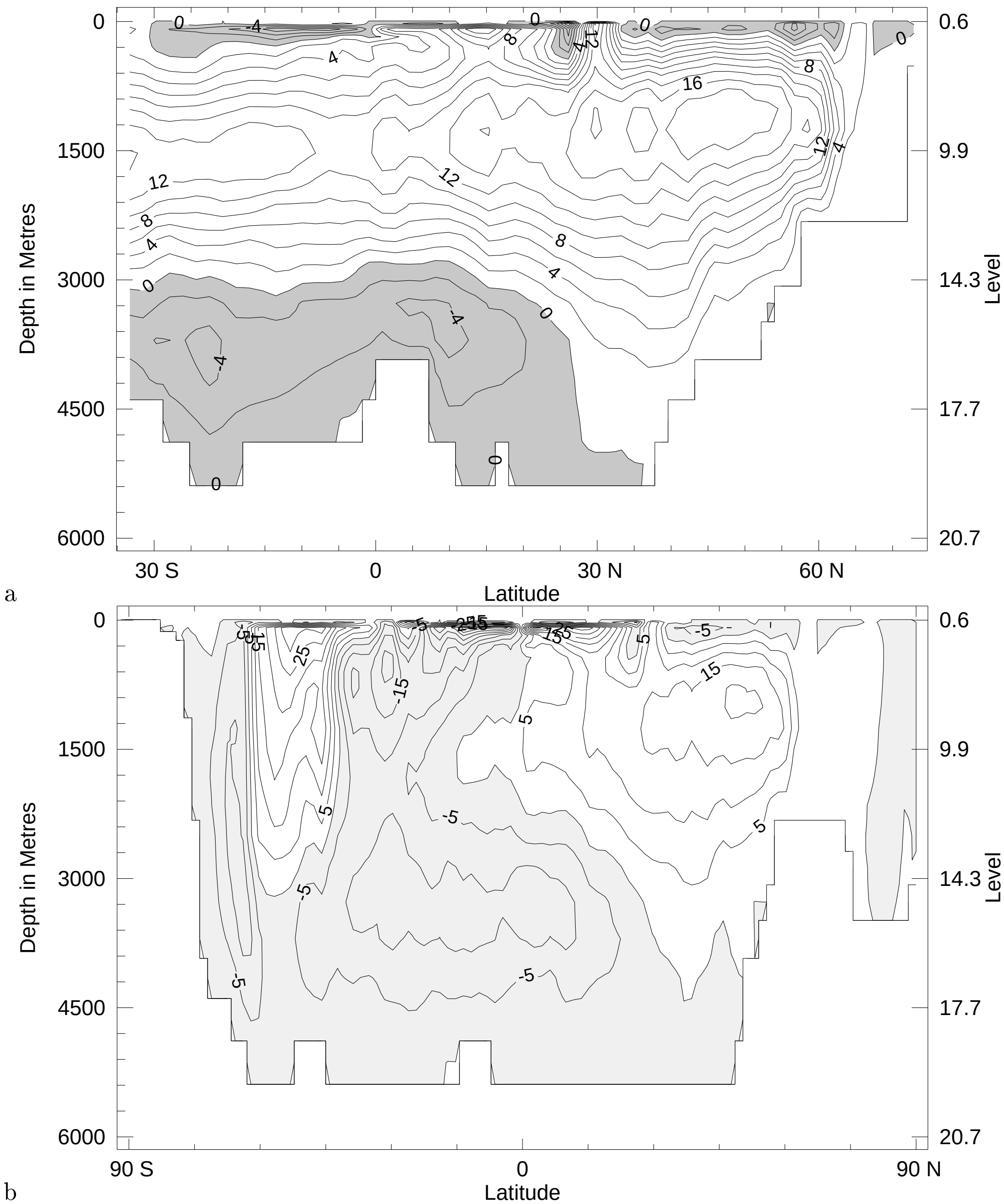

Figure 18: Annual mean meridional overturning streamfunction (Sv) for the a) North Atlantic and b) global oceans.

3.3 Sea Ice

Even in its standard form, the sea ice model used in the UVic ESCM is quite sophisticated when compared to those in use in most coupled atmosphere-ocean GCMs. When compared to these same models (Table 3), the resulting seasonal climatology of the UVic ESCM ranks very high (for both sea ice and snow cover combined and considered separately). Even so, the fact that NADW forms too far south (Fig. 18a) leads to a sea ice cover that extends too far south in the North Atlantic, especially in winter (Fig. 19). Winds in the Arctic cause the sea ice to pile up on the northern coast of Canada and northwest Greenland where a maximum thickness of slightly over 4 m is simulated. Averaged over the entire Arctic Ocean, sea ice is about 1 m thick. In the Southern Hemisphere, sea ice typically forms to a thickness of 20 cm, consistent with observations, although it is thicker near the coast. Very little sea ice forms off the coast of Antarctica south of Australia due to the Antarctic Circumpolar Current being steered too far south by the Kerguelen plateau and bringing relatively warm waters poleward.

Table 3: Coupled model simulations of hemispheric ice and snow cover (10^6 km^2) ranked by the average absolute error from observations Gates et al. (1996).

Northern Hemisphere ice cover		Northern Hemisphere snow cover		Southern Hemisphere ice cover			
DJF	JJA	DJF	JJA	JJA	DJF	Error	Model
14.8	10.7	44.7	7.8	16.4	6.2	-	observed
14.0	7.1	42.2	12.2	14.7	8.1	2.5	UVic*
11.0	8.3	41.2	2.5	12.4	6.4	3.2	GISS*
9.7	7.1	42.9	11.5	12.2	7.5	3.3	CCC
10.2	5.3	35.3	5.1	18.0	5.9	4.0	UKMO
19.1	11.5	34.3	2.9	11.6	3.1	4.7	MRI
13.6	0.5	41.4	2.1	5.3	0.5	6.2	NCAR*
9.3	1.6	53.4	12.1	4.0	3.7	7.1	COLA*
16.0	12.7	64.4	10.0	24.7	16.0	7.2	GFDL
16.6	14.5	37.5	11.6	21.1	18.9	7.3	CSIRO
18.9	16.7	62.0	28.4	0.5	0.5	*11.6*	BMRC*

*indicates a model without flux adjustments

3.4 Water Mass Formation

Here we extend the analysis of Duffy et al. (1999) by examining the advection and diffusion of three passive 'age' tracers in a version of the model that now incorporates the Duffy and Caldeira (1997) and Duffy et al. (1999 2001) parametrisation of brine rejection due to sea ice growth, the Gent and McWilliams (1990) parametrisation for mixing associated with mesoscale eddies, and five sea ice categories (plus open water) (Bitz et al. 2001). The purpose of this experiment is to examine the major pathways of the global oceanic circulation within our model, and specifically to determine to what extent the model is able to capture the formation and recirculation of the NADW, AAIW, and AABW water masses. Another issue of interest is to see whether or not the model can

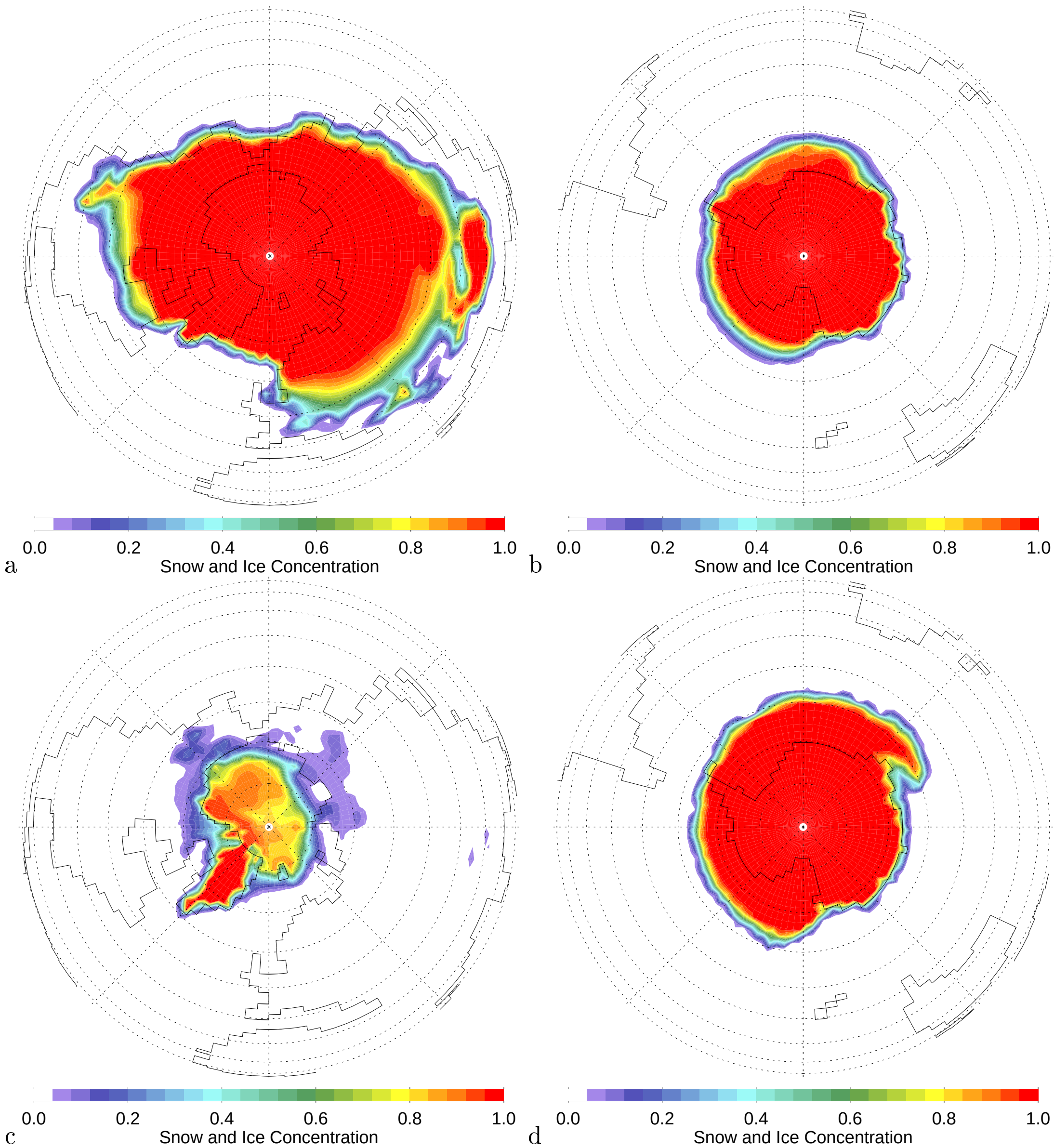

Figure 19: Maximum sea ice concentration. a) and c) show northern hemisphere polar projections in the boreal winter and summer, respectively. b) and d) show southern hemisphere polar projections in the austral summer and winter, respectively. Over the land, the contours indicate maximum concentration in snow coverage. The plots show the average concentration for the three month period covering the summer (July – September) and winter (January–March). As such, they emphasise the maximum extent during any particular season.

simulate the so-called 'cold route' of the NADW return path through Drake Passage (Gordon 1986 1997) in the form of intermediate water, recently inferred from hydrographic data and inverse methods (Rintoul 1991).

A novel feature of the model in this simulation is the parametrisation of brine rejection due to sea ice growth after Duffy et al. (1999), generalised for the case of a multi-category sea ice. In the generalisation we spread the brine under each sea ice category according to its (thermodynamic) growth, after which both potential temperature and salinity are convectively mixed, under the category, if instability is detected. The resultant potential temperature and salinity profiles under each category within the grid cell (including open water) are averaged according to their areas to form mean grid cell profiles. Further details are given in Saenko et al. (2001).

The 'age' tracers (T_r) are governed by the same dynamics as potential temperature and salinity, except for an additional term (Q), i.e.,

$$\frac{\partial T_r}{\partial t} = -advective(T_r) + diffusive(T_r) + convective(T_r) + Q \tag{51}$$

The Q term takes the following form

$$Q = -\frac{T_r}{\tau} \quad \text{for regions of tracer release} \tag{52}$$

$$Q = \frac{1}{y_r} \quad \text{otherwise} \tag{53}$$

where the relaxation parameter τ is set to 30 days and y_r is a non-dimensional parameter set to be numerically equal to the number of seconds in a year, so that T_r corresponds to time in years since tracer release. The boundary conditions applied to Eq. 51 are zero flux at all boundaries, including the ocean-air interface, and initially T_r is set to zero over the whole ocean domain. In the ocean model, the vertical, isopycnal and isopycnal thickness diffusivities were set to $k_v = 0.7 \times 10^{-4}$, $k_i = 2.0 \times 10^3$, $k_t = 2 \times 10^3$ m^{2}s^{-1}, respectively. In the Duffy and Caldeira (1997) and Duffy et al. (1999 2001) approach to parametrise vertical mixing of brine associated with sea ice formation, rejected salt is spread uniformly to a depth defined by a specified potential density difference between the level of salt spreading and the surface. In this experiment we choose this specified potential density difference as $\Delta\rho = 0.2$ kgm^{-3}. A complete description of the generalisation of this scheme to multi-category sea ice, as well as a sensitivity analysis of our model to the choice of $\Delta\rho$, can be found in Saenko et al. (2001).

The model was initially spun up for 2000 years until a statistical equilibrium was reached. At this point, three age tracers were released in the GIN Sea, North Pacific and Ross/Wedell Seas, respectively (Fig. 20), and the model integration was continued for a further 500 years. The results are illustrated through the 27°W section plots (through the Atlantic Ocean) of Fig. 21. Due to the nature of the boundary conditions on the age tracer, regions where the age tracer has not penetrated are indicated by the 500 year contour.

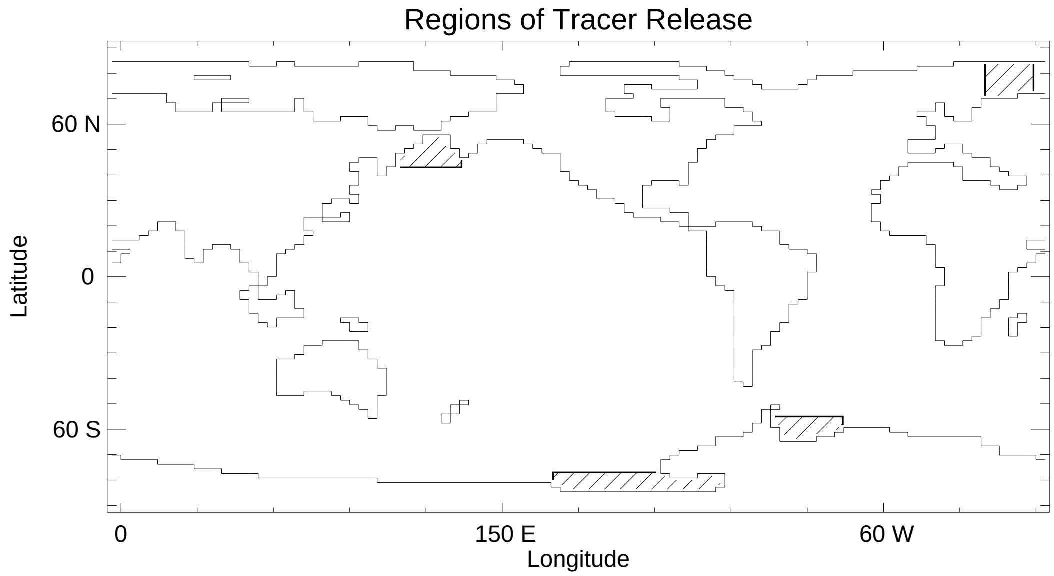

Figure 20: Model domain. Dashed lines in the GIN Sea, North Pacific, and Weddell and Ross Seas indicate where the passive "age" tracers where released.

The model clearly simulates the sinking and spreading of NADW below the permanent thermocline to a depth of about 3000 m and above the AABW (Fig. 21a,b). A detailed analysis indicates that the NADW flows into the Antarctic Circumpolar Current, primarily in a deep western boundary undercurrent, crosses the Indian Ocean with much of it entering the deep Pacific through two paths (one on either side of New Zealand) where it upwells. The remainder proceeds with the Antarctic Circumpolar Current to recirculate through the Drake Passage. The waters which upwell in the North Pacific can be tracked by the North Pacific age tracer release experiment shown in Fig. 21c. Surface waters of the North Pacific leave the basin through two routes: the first and most important is via the Indonesian throughflow while the second is through Drake Passage. In the latter case, these North Pacific waters enter the South Atlantic in the form of Antarctic Intermediate water which supports the results of the inverse modelling study of Rintoul (1991). Furthermore, as indicated in Fig. 21c, most of this intermediate water then converts into thermocline water as it moves northward into the North Atlantic. The remainder, however, converts into deep and bottom water in the South Atlantic and then exits towards the Indian Ocean, in further agreement with observational-based results of Rintoul (1991). As such, it appears that the model supports both the warm and cold water routes of Gordon (1986) and Rintoul (1991).

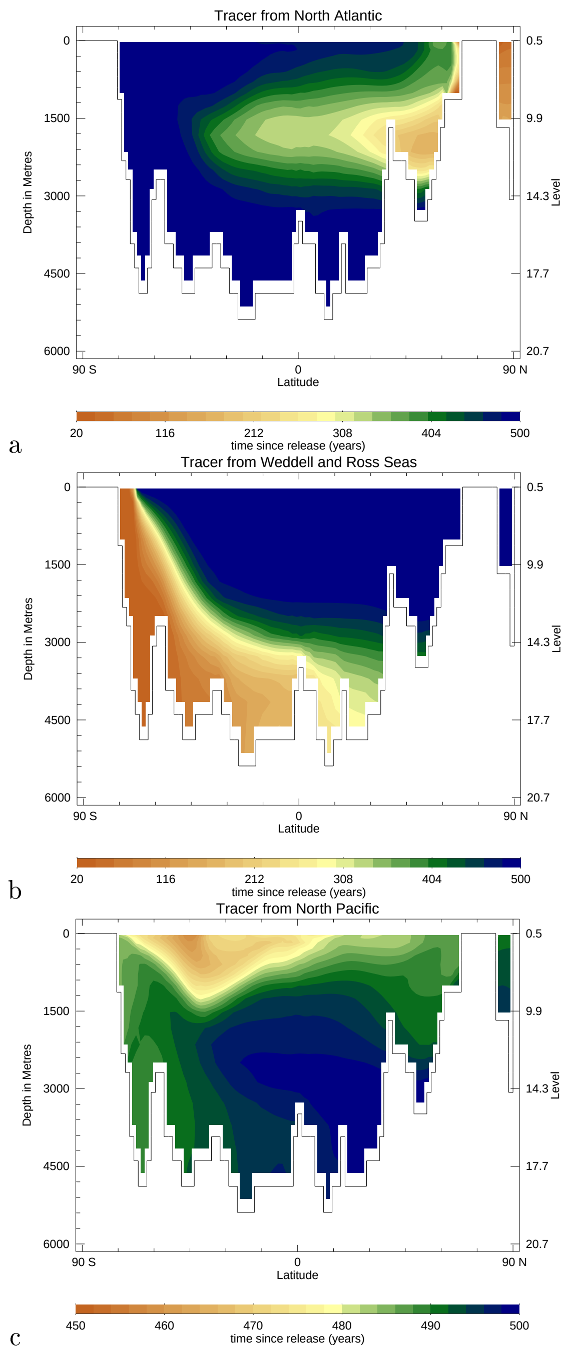

Figure 21: A latitude-depth section at 27°W for the "age" tracer released from GIN Sea (a), Weddell and Ross Seas (b), and North Pacific (c).

3.5 Inorganic Ocean Carbon Cycle

As a first step towards incorporating a comprehensive carbon cycle model into the UVic ESCM (see section 8), we have included an inorganic ocean carbon model. This allows us to evaluate our model against those participating in the IGBP Ocean Carbon-Cycle Model Intercomparison Project (OCMIP). We have implemented the inorganic carbon component by closely following the protocols set out by OCMIP (Orr et al. 1999). Dissolved inorganic carbon (DIC) is modelled as a passive tracer subject to the following conservation equation (c.f. Eq: 45):

$$\frac{\partial DIC}{\partial t} + L(DIC) = \frac{\partial}{\partial z}\left(k_v \frac{\partial DIC}{\partial z}\right) + \nabla(k_h \nabla DIC) + J + J_v \tag{54}$$

where the source/sink term J represents the air-sea flux of CO_2 and the virtual source/sink term J_v represents the changes in DIC due to evaporation, precipitation and runoff. The air-sea gas-exchange flux is modelled using the following equation:

$$F = k_w(C_{atm} - C_{surf}) \tag{55}$$

where C_{atm} and C_{surf} are calculated using the partial pressures of CO_2 in both the atmosphere and ocean surface layer, respectively. The CO_2 transfer velocity k_w is modified from Wanninkhof (1992) and is given by:

$$k_w = (1 - \gamma_{ice}) 0.337 |\mathbf{V}_s|^2 \left(\frac{S_c}{660}\right)^{0.5} \tag{56}$$

where γ_{ice} is the fractional sea ice cover (varying between 0.0 to 1.0). We assume that there is no gas exchange through the ice. The wind speed $|\mathbf{V}_s|$ is as discussed in section 2.1.1, and the Schmidt number (S_c) is a function of model SST (Wanninkhof 1992).

To illustrate the quasi- equilibrium surface fluxes of CO_2 in our model, we use the same version as in section 3.4 but with only one ice category (plus open water) i.e., the model incorporates the Duffy and Caldeira (1997) parametrisation of brine rejection due to sea ice growth and the Gent and McWilliams (1990) parametrisation for mixing associated with mesoscale eddies. The model is initialised with a prescribed preindustrial atmospheric pCO_2 of 280 ppm and integrated for 1440 years. The resulting quasi-equilibrium air-sea fluxes (Fig. 22) show a net-flux of CO_2 into the atmosphere occurring as a broad-banded feature about the equator and along the western coasts of South America and Africa, in areas of near-shore upwelling. This outgassing also occurs in regions off the Argentinian and southeastern Australian coasts. Our use of isopycnal mixing reduces spurious deep convective plumes in the Southern Ocean leading to a fairly homogeneous region of CO_2 uptake between

50–65° S. High uptake also occurs in the North Atlantic and to some extent in the North Pacific and well as off the southwestern coast of Africa.

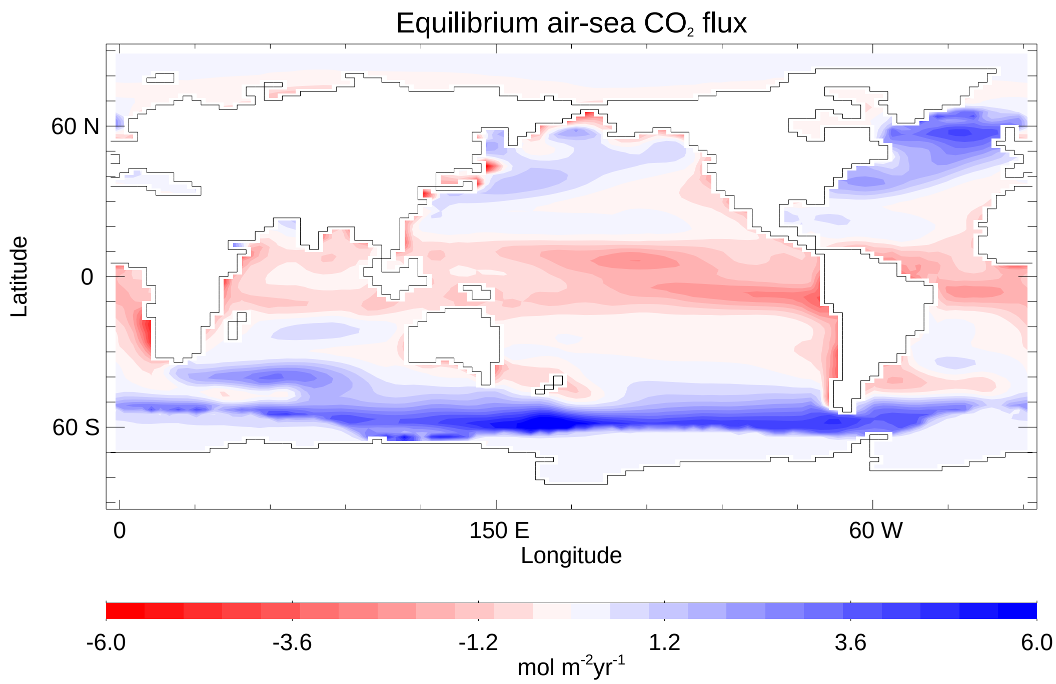

Figure 22: Air-sea flux (Moles $m^{-2}yr^{-1}$) of inorganic carbon after 1440 years of integration. Blue regions indicate areas of carbon uptake by the ocean whereas red areas indicate where the ocean is outgassing.

3.6 Summary

In this section we have tried to demonstrate that the UVic ESCM, in its standard representation, provides a reasonable simulation of the current climate. We have alluded to, and explicitly shown how certain shortcomings can be improved through the inclusion of more sophisticated and realistic parametrisation of sub grid scale processes. While we believe the precipitation field is one of the major weaknesses of the diffusive moisture transport formulation of our atmospheric model, we still conclude that the ESCM serves as a useful tool with which to investigate the importance of climate processes in past, present and future climate simulations (see sections 6 and 7). Of course, a caveat that we need to add concerning our comparison with coupled atmosphere-ocean GCMs (Tables 1-3) is that the indices we used represent relatively simple, albeit important, measures of model performance. In addition, most coupled modelling groups are currently using newer versions of their models than those evaluated in Gates et al. (1996). Finally, the simple atmospheric component of our model does not allow for internal variability, unlike more comprehensive coupled atmosphere-ocean GCMs.

In the next section, through the inclusion of advection in the treatment of moisture transport, we will show how the model leads to an extremely good simulation of the present-day precipitation field and surface salinity field, without compromising the climatology of the other fields discussed above. When combined with the wind feedback option, we will further determine (in section 5) how the change of moisture transport from a diffusive to an advective formulation affects the response of the climate system in global warming experiments.

4 Moisture Advection

As noted in section 3, the precipitation field simulated by the coupled model when diffusive transport is used has serious limitations, especially near the intertropical convergence zone where moisture transport in nature is up gradient. To improve our precipitation field, we exploit the observation that most of the atmospheric moisture transport happens within the planetary boundary layer, allowing us to use the surface wind field to accomplish advection. In this section we discuss the rather dramatic improvements that arise when we include moisture advection in our coupled model. In section 4, we examine what effects this has in global warming simulations where the wind feedback is also allowed to operate.

In order to include moisture advection we rewrite Eq. 8 as

$$\rho_a h_q \left\{ \frac{\partial q_a}{\partial t} - \nabla \cdot (\kappa \nabla q_a) + \beta \nabla \cdot (\mathbf{u} q_a) \right\} = \rho_o (E - P) \tag{57}$$

where the new parameter β relates the vertically-averaged advective moisture transport to the surface advective transport ($\beta = 0.4$) and $\mathbf{u}$ is the surface wind. In the absence of the representation of explicit cloud processes, another parametrisation must be included in order to limit the local release of latent heat during strong precipitation events in regions of converging winds. Rather than locally changing the planetary albedo and reducing incoming solar radiation (associated with deep clouds for example) we adopted a modified thermal diffusive coefficient $\nu + \nu^*$ so that the atmospheric heat transport (Eq. 2), becomes:

$$Q_T = \rho_a h_t c_{pa} \nabla \cdot ((\nu + \nu^*) \nabla T_a) \tag{58}$$

The effect of the ν^* term in Eq. 58 is to balance the latent heat associated with condensation arising from convergence of moisture by advection. We parametrise ν^* as

$$\nu* = \begin{cases} 0 & P < P_{min} \\ \nu_0 \frac{P - P_{min}}{P_{max} - P_{min}} & P_{min} \le P \le P_{max} \\ \nu_0 & P > P_{max} \end{cases} \tag{59}$$

where $\nu_0 = 60 \times 10^6$ m^2 /s, $P_{min} = 2.0$ m/yr and $P_{max} = 4.0$ m/yr are empirical constants. This localised diffusive process is only active with the advective transport of moisture option and is only evoked in regions of strong moisture convergence. The use of moisture advection also necessitates the use of a larger thermal diffusive transport coefficient ν in tropical regions, due to enhanced latent heat release, although the coefficient of moisture diffusion is substantially reduced (Fig. 23).

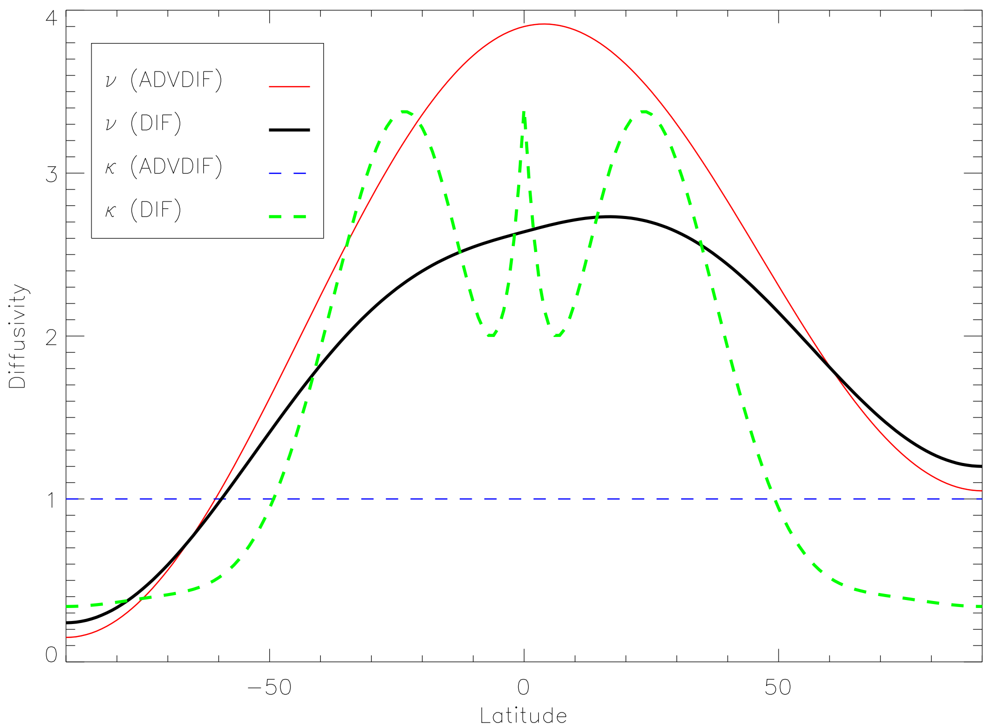

Figure 23: Latitudinal profile of the heat ν (solid curves) and moisture κ (dashed curves) diffusion coefficients (in 10^6 m^2/s) for the simulations using only diffusive moisture transport (DIF) and diffusive + advective moisture transport (ADVDIF).

When moisture advection is included in the model, the representation of precipitation (Fig. 24) is substantially improved over the case where moisture transport is only accomplished through diffusion (Fig. 11). The most notable improvements occur near the intertropical convergence zone, where moisture transport is up gradient, and near monsoon regions. The midlatitude North Atlantic and Pacific are regions where the precipitation is still slightly underestimated, although the spatial pattern of precipitation over the ocean is more realistic there. Our precipitation over land, within the coupled model, still remains troublesome in tropical regions, most likely due to our lack of land surface processes. Nevertheless, all precipitation over land in these regions is instantaneously returned to the ocean as runoff.

Evaporation minus precipitation (Fig. 25) is also substantially improved over the case in which moisture transport is only accomplished by diffusion (Fig. 13). The global zonally-averaged field reasonably reproduces the NCEP climatology at most latitudes. The mid-latitudes in the northern hemisphere have too much net evaporation, although at these latitudes the two-dimensional field bears fine resemblance with the NCEP climatology.

The climatology of the coupled model is not changed dramatically from that presented in section 3. For

a

b

c

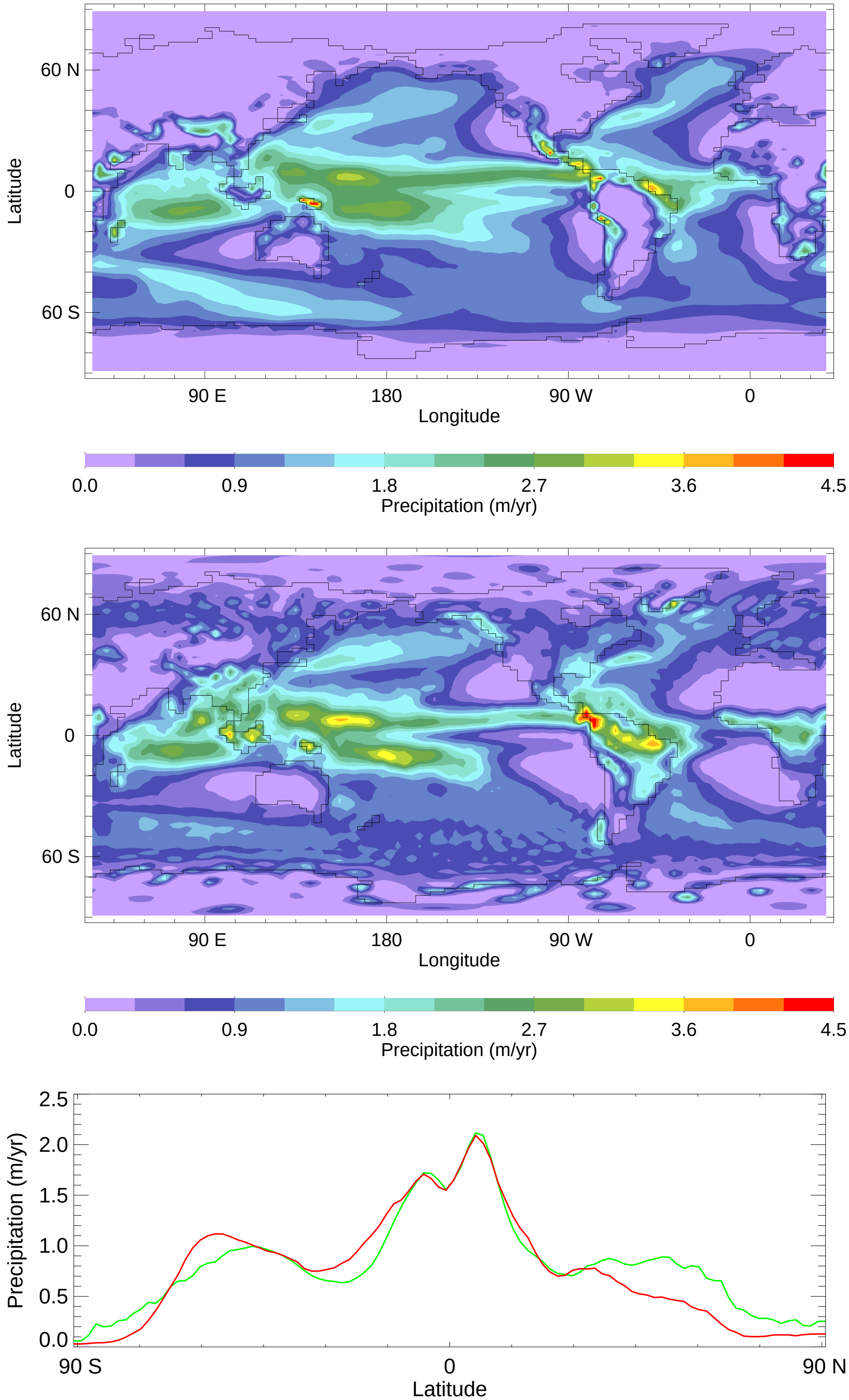

Figure 24: Annual mean precipitation (m/yr) for a) model, b) NCEP climatologies: c) The zonally-averaged model (red) and NCEP (green) climatologies.

a

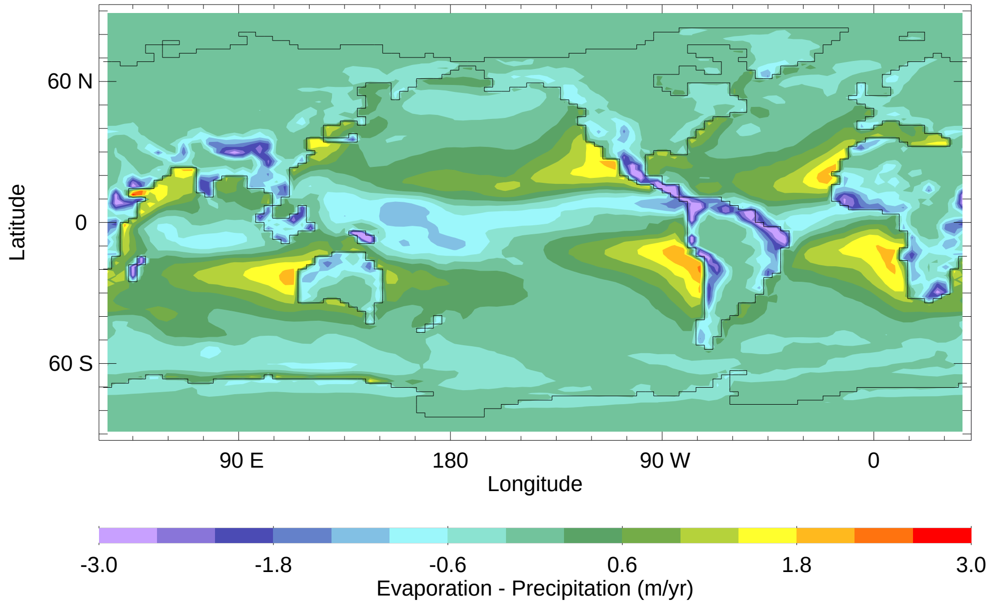

b

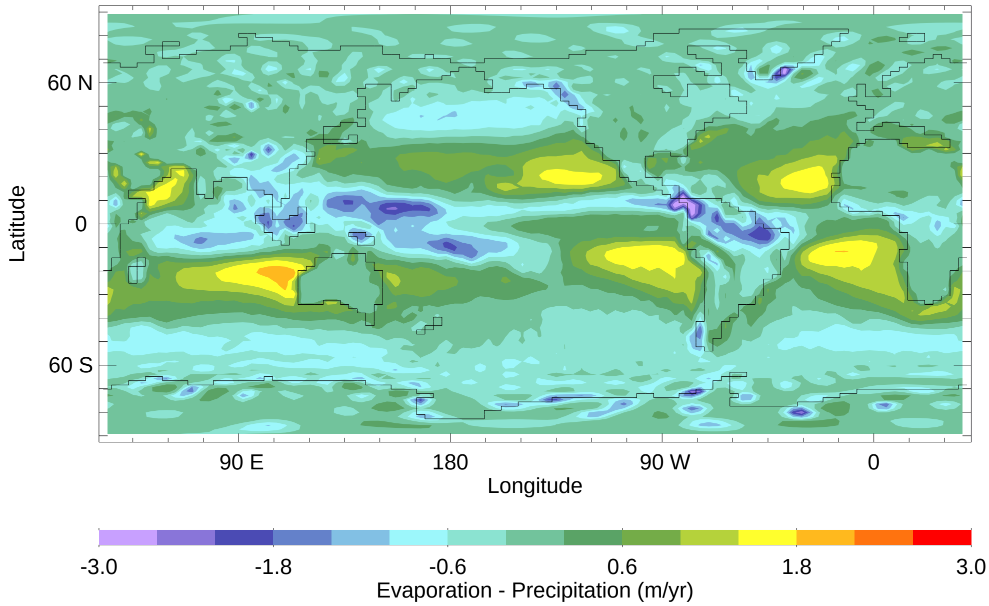

c

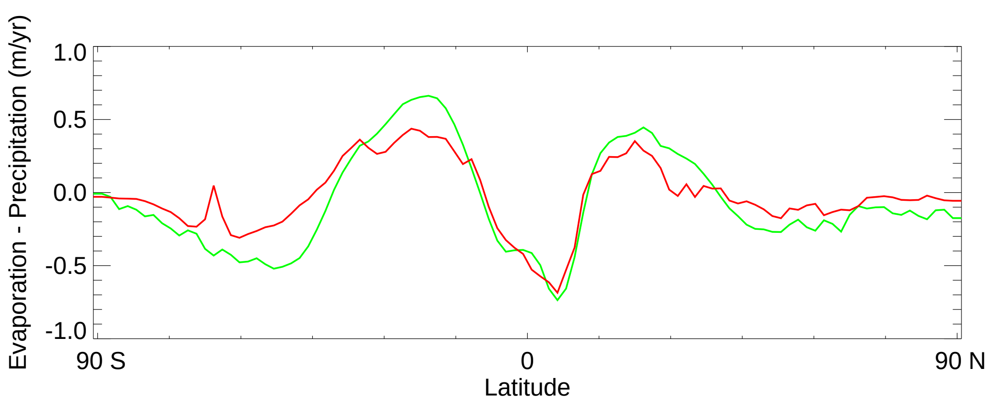

Figure 25: Annual mean evaporation minus precipitation (m/yr) for a) model, b) NCEP climatologies: c) The zonally-averaged model (red) and NCEP (green) climatologies.

example, the SAT map (Fig. 26a) is very similar to the analogous diffusive version (Fig. 26b), as well as the NCEP reanalysis data (Fig. 10b). The differences between the SAT fields obtained under the advective and diffusive treatments of moisture transport (Fig. 26b) are largely confined to regions where large differences exist in latent heat release in the atmosphere. The advective model tends to cause the monsoon and intertropical convergence zone regions to be slightly warmer, as precipitation is increased there, and the ocean desert regions of the eastern flanks of the subtropical gyres to be slightly cooler, as descending air from above causes divergent surface winds.

The same features seen in the SAT field are reflected in the SST field (Fig. 27), leading to a much better agreement with the Levitus and Boyer (1994) observations (Fig. 14b). Notable areas of discrepancy between observed and modelled SST fields in section 3 were found in the Southern Indian Ocean and along the eastern boundary, near the mid-latitude coasts of the Pacific and Atlantic, where simulated SSTs were too warm, as well as the Gulf of Alaska and the Greenland-Iceland-Norwegian (GIN) Seas which were too cold. While the western boundary separation points of the Kuroshio and Gulf Stream have not changed, the SSTs over much of the North Atlantic have cooled. In fact, in most of the global ocean the subtropical gyre regions, and particularly their eastern edge, have cooled bringing the simulated fields in better agreement with observations.

The improved representation of both precipitation and evaporation minus precipitation naturally reflects itself in a better distribution of the SSS field (Fig. 28). The SSS field obtained without advection for moisture transport (section 3) did not readily reveal local maxima in the subtropical gyre regions of the world oceans nor did it show much east-west asymmetry in the Pacific (Fig. 15). When moisture transport is accomplished through advection, salinity maxima develop in the subtropical gyre regions and the observed east-west tropical Pacific asymmetry develops, with a relatively fresh western equatorial Pacific and a relatively saline eastern subtropical Pacific.

The water mass structure of the global oceans remains similar to that found in section 3, although the potential temperature and salinity properties of the different water masses have changed slightly. Generally, the thermocline region is slightly colder through subduction arising in the now colder subtropical regions, in the advective case (Fig. 29a) and the deeper ocean is slightly warmer. Very little change is seen in the zonally-averaged salinity field (Fig. 29b). Once more, AAIW is not well represented using the horizontal/vertical representation of mixing — see our earlier discussion and Duffy et al. (1999 2001).

The generally colder surface ocean in the North Atlantic (Fig. 27), and the warmer, deep ocean seen in Fig. 29a counteracts the slightly increased overturning in the North Atlantic in the advective case (Fig. 30a,c), to give only a slight decrease in the northward heat transport in the North Atlantic Ocean. While the large scale features of the meridional overturning are only slightly changed upon moving to advective moisture transport, the increase in NADW formation comes at the expense of a slight decrease in AABW intrusion into the deep

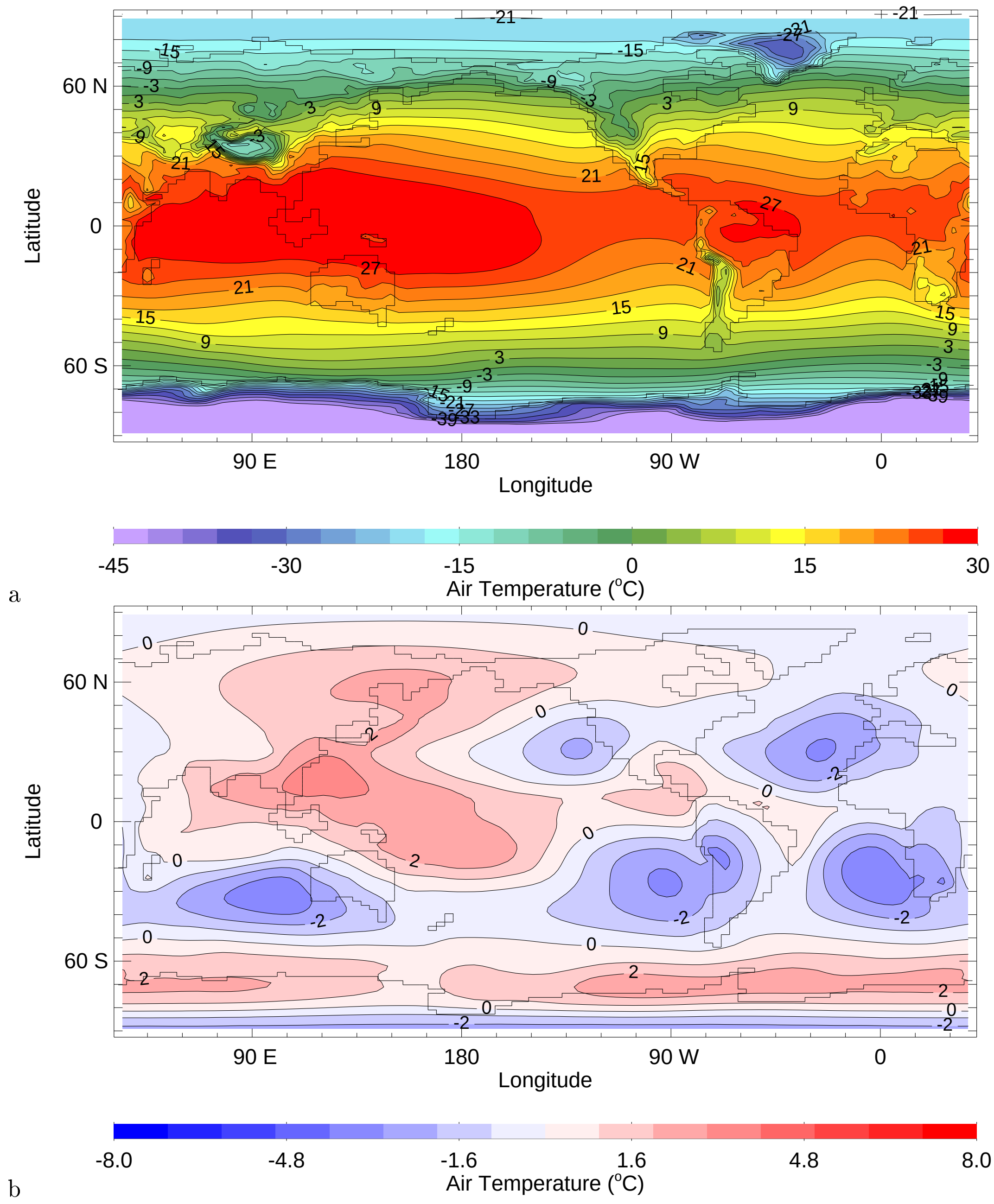

Figure 26: a) Annual mean equilibrium surface air temperature (°C) using advection for moisture transport. b) The difference between a) and that obtained for purely diffusive moisture transport (Fig. 10a).

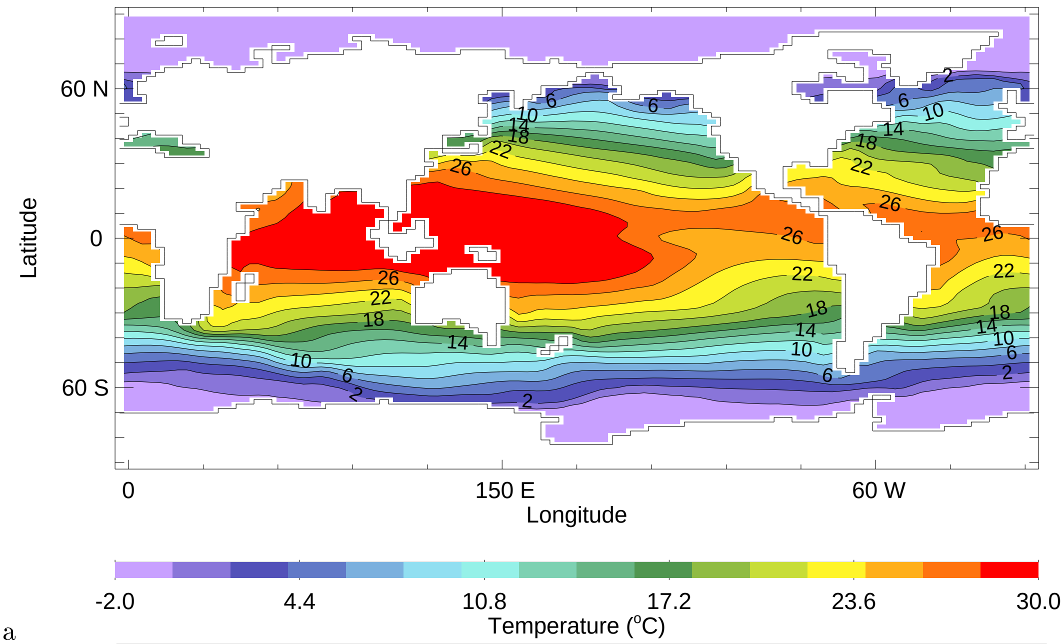

a

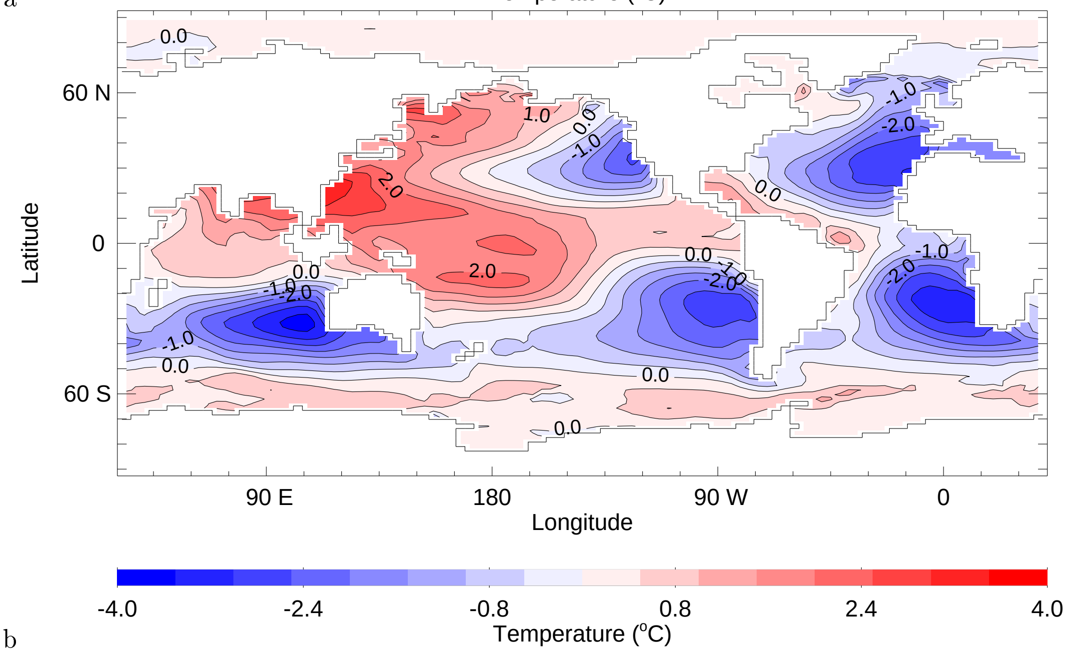

b

Figure 27: a) Equilibrium sea surface temperature (°C) using advection for moisture transport. b) The difference between a) and that obtained for purely diffusive moisture transport (Fig. 14a).

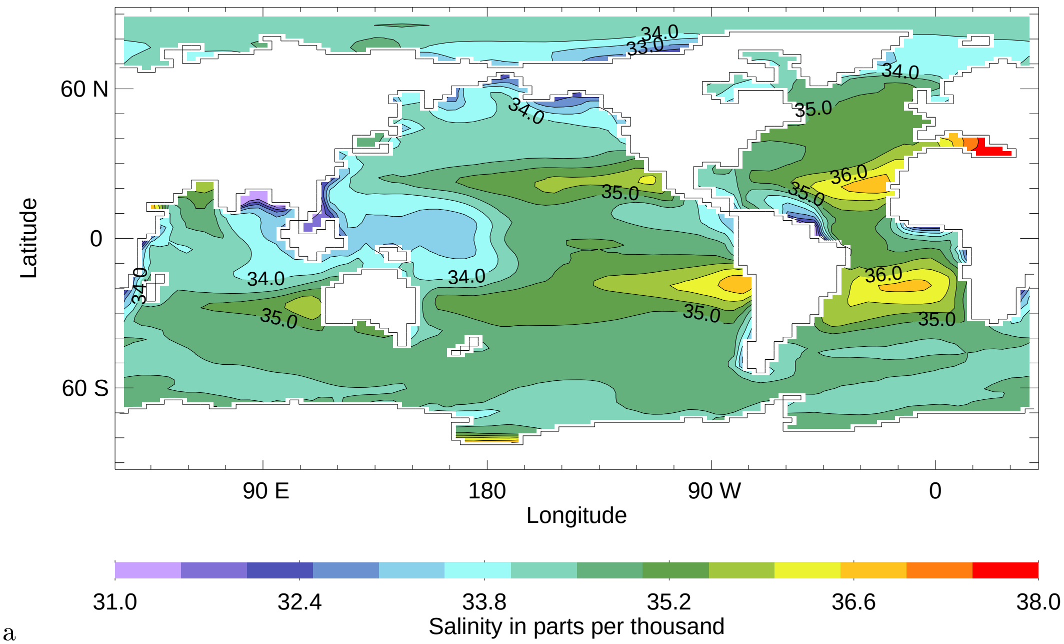

a

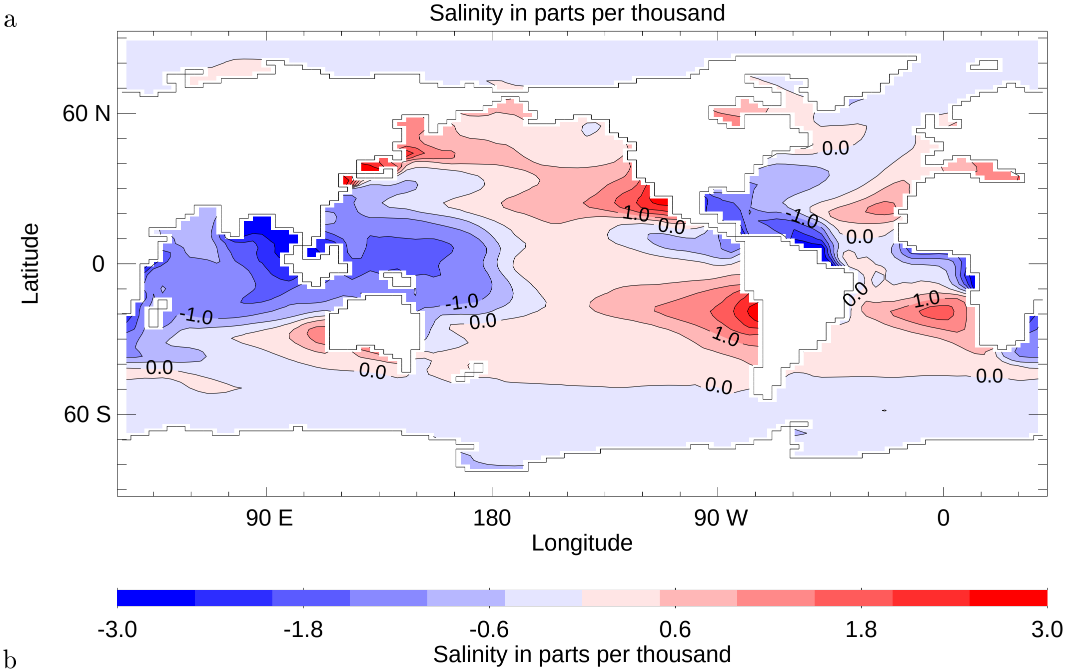

b

Figure 28: a) Equilibrium sea surface salinity (psu) using advection for moisture transport. b) The difference between a) and that obtained for purely diffusive moisture transport (Fig. 15a).

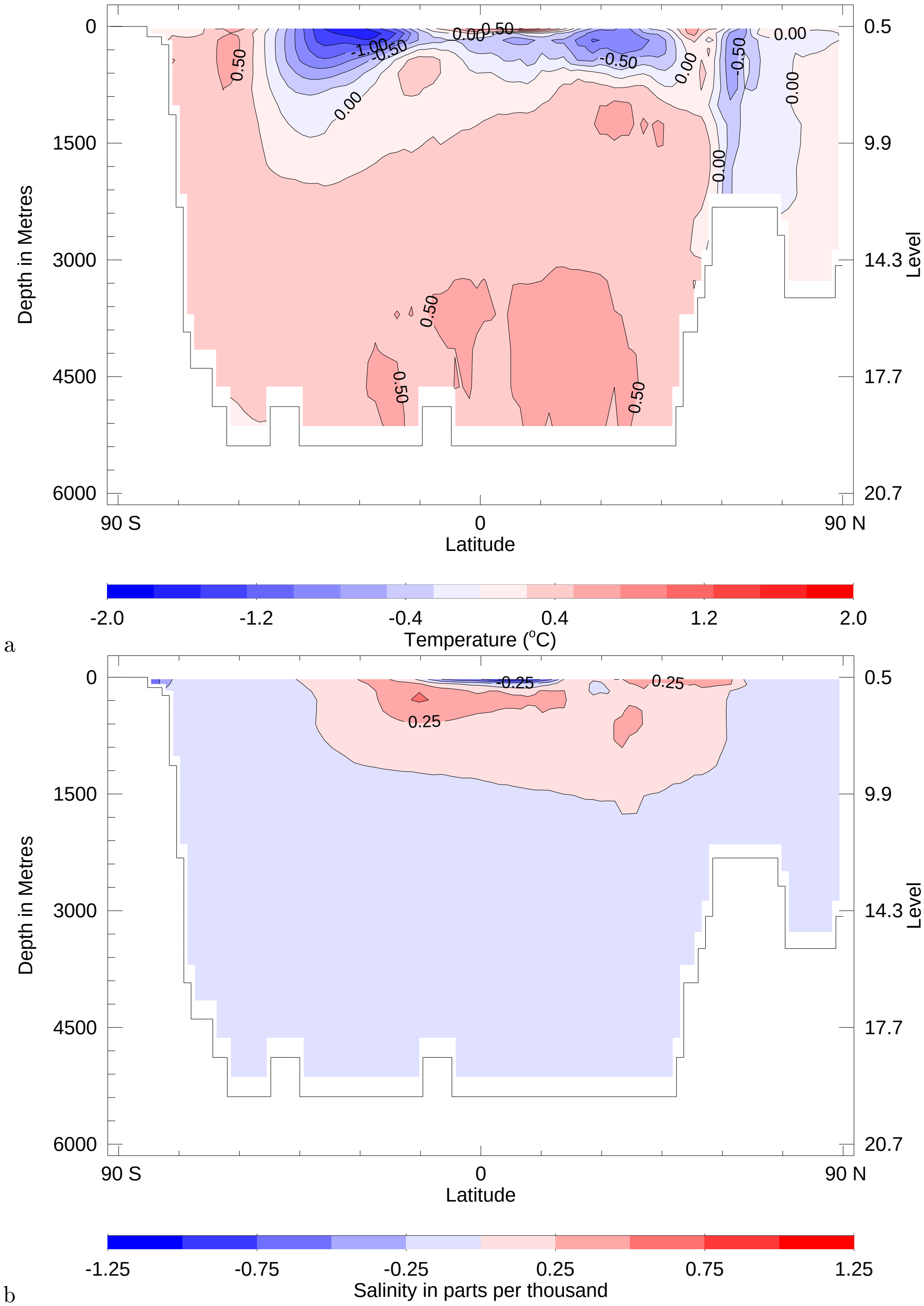

Figure 29: The difference (advective minus diffusive) between the equilibrium global zonally-averaged a) potential temperature (°C) and b) salinity (psu) obtained under advective and diffusive representations of moisture transport.

North Atlantic. The Deacon Cell in the Southern Ocean, which is a prominent feature of both this experiment and the diffusive case, is not a feature of our coupled model when we include isopycnal mixing and the Gent and McWilliams (1990) representation of mixing associated with mesoscale eddies, as expected from the earlier analyses of Danabasoglu et al. (1994) and Robitaille and Weaver (1995).

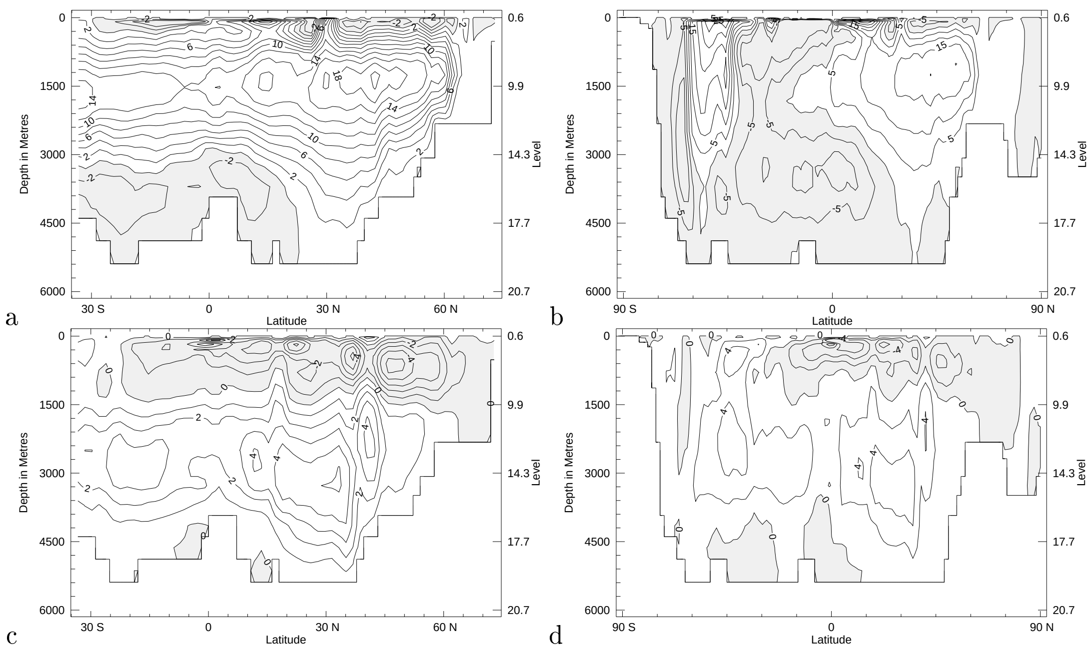

Figure 30: Meridional overturning streamfunction (Sv) for the a) North Atlantic and b) global oceans at equilibrium for the case where advection is used for moisture transport. c) and d) show differences [a) minus Fig. 18a and b) minus Fig. 18b)] from when only diffusive moisture transport is used. The contour interval is 1 Sv in c), 2 Sv in a) and d), and 5 SV in b).

Taken together, the improvements realised when moisture transport is parametrised through advection by winds far outweigh the small increase in computational expense. As such, future versions of our coupled model will include moisture advection as the standard option. In the next section we show how the moisture advection option can be combined with the wind stress feedback parametrisation to provide for a first order feedback accounting for changing moisture advection in a changing climate.

5 Global Warming and the Role of Moisture Advection

In the previous section we demonstrated how the inclusion of moisture advection substantially improved the climatology of our ESCM. In this section we now determine whether or not the improved parametrisation of moisture transport has any effect on the transient behaviour of the system. In particular, we conduct four global warming sensitivity experiments using both diffusive and advective treatments of moisture transport with and without the wind feedback parametrisation of section (2.1.1).

The initial condition of the four experiments was the 1998 equilibrium climatology discussed in sections 3 and 4 for diffusive and advective treatments of moisture transport, respectively. The atmospheric level of CO_2 was increased at a rate of 1% per year until 4×present day CO_2 was reached, at which point atmospheric concentrations were held fixed for 500 years of total integration.

Both the transient and quasi-equilibrium warming in all four experiments are nearly identical (Fig. 31a), suggesting very similar climate sensitivities of about 3.0°C (for a doubling of atmospheric CO_2), in all cases. After 500 years the warming relative to the initial condition in the four experiments is: 1) Advective moisture transport — 6.00°C; 2) Advective moisture transport with wind feedback — 6.01°C; 3) Diffusive moisture transport — 6.23°C; 4) Diffusive moisture transport with wind feedback — 6.26°C. The overall horizontal pattern of the warming is similar in all the experiments, with the exception of the region around the North Atlantic and over the subtropical gyre regions of the ocean (Fig. 32). All experiments show a tendency for more warming over land than over the ocean and an amplification of the warming at high latitudes. In all experiments the overturning in the North Atlantic initially weakens, although it re-establishes once the radiative forcing is held fixed (Fig. 31b).

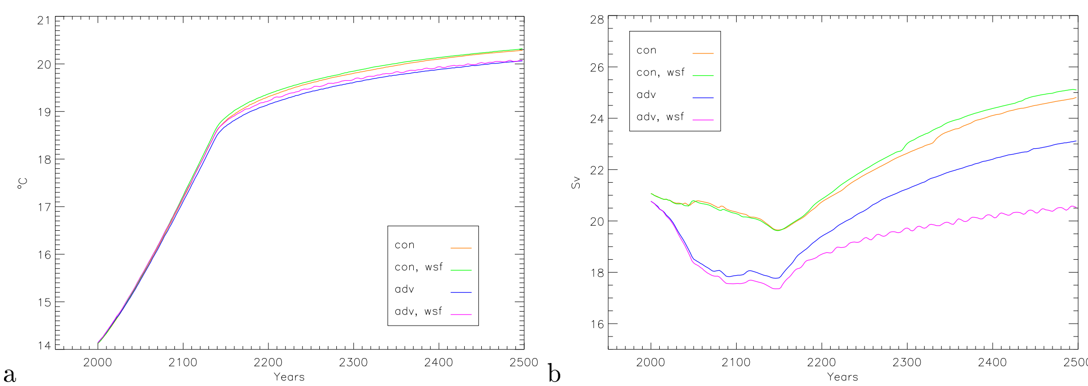

Figure 31: Time series of a) global mean surface air temperature (°C) and b) maximum North Atlantic meridional overturning streamfunction (Sv) for the four experiments. Moisture transport is either diffusive ('con' in the legend; yellow, green) or advective ('adv' in the legend; blue, pink) and the wind feedback is either on ('wsf' in the legend; green, pink) or off (yellow, blue).

In the two diffusive moisture transport experiments, the thermohaline circulation in the North Atlantic eventually re-established to a strength that was stronger than the 1998 initial condition, consistent with the results of Wiebe and Weaver (1999), obtained using an older version of our model. In the case of advective moisture transport, without the wind feedback, the thermohaline circulation declined further, in the transient phase, but also reequilibrated to a value slightly higher than in the 1998 initial condition. The advective moisture transport case with the wind feedback included closely tracked the analogous case without the feedback, while the radiative forcing was changing, but re-established to a value that was almost identical to its initial condition (Fig. 31b). The differences seen in Fig. 32 in the northern North Atlantic are therefore simply explained by the different behaviour of the thermohaline circulation in the four experiments. In the diffusive transport case, where the overturning equilibrates at a stronger value, there is more melt back of sea ice leading to a subsequent positive albedo feedback on surface warming. In addition, there is an enhanced oceanic heat loss to the atmosphere due to the removal of the insulating sea ice cover. In the case where the overturning equilibrates to a level similar to its initial condition, there is no additional positive feedback on the sea ice to further enhance the warming locally.

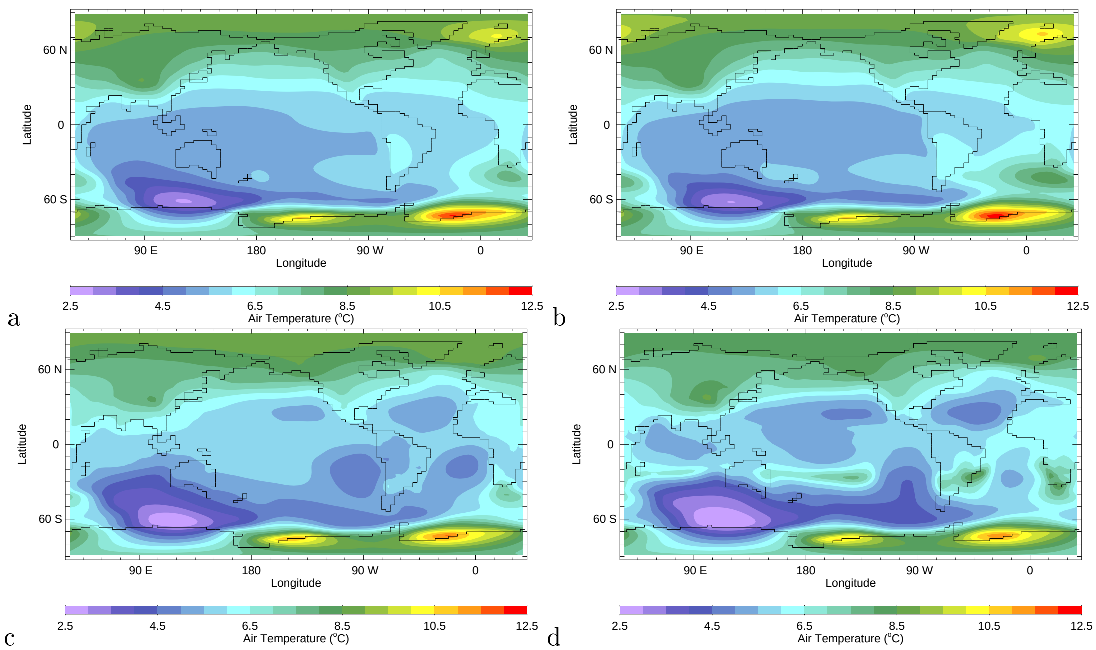

Figure 32: Surface air temperature change at year 500 (relative to 1998) for the $4\times CO_2$ equilibrium integrations. a)- Diffusive moisture transport; b)- Diffusive moisture transport with wind feedback; c) Advective moisture transport; d) Advective moisture transport with wind feedback.

A fundamental question then remains as to what is the physics responsible for the re-establishment of the thermohaline circulation to different strengths in the different experiments. As shown by Hughes and Weaver (1994), the strength of the overturning in the North Atlantic is proportional to the meridional gradient in the zonally-averaged depth-integrated steric height (DISH) from the tip of Africa to the latitude at which deep water formation occurs. Indeed, the overturning is also proportional to the meridional DISH gradient along the western boundary which is balanced by a current flowing down the meridional DISH gradient in a frictional boundary layer. As suggested in Hughes and Weaver (1994), perturbations to either the hydrological cycle (e.g., Fig. 33), heat balance or wind field which cause the DISH to change in either the northern or southern hemisphere, subsequently cause the overturning circulation to change.

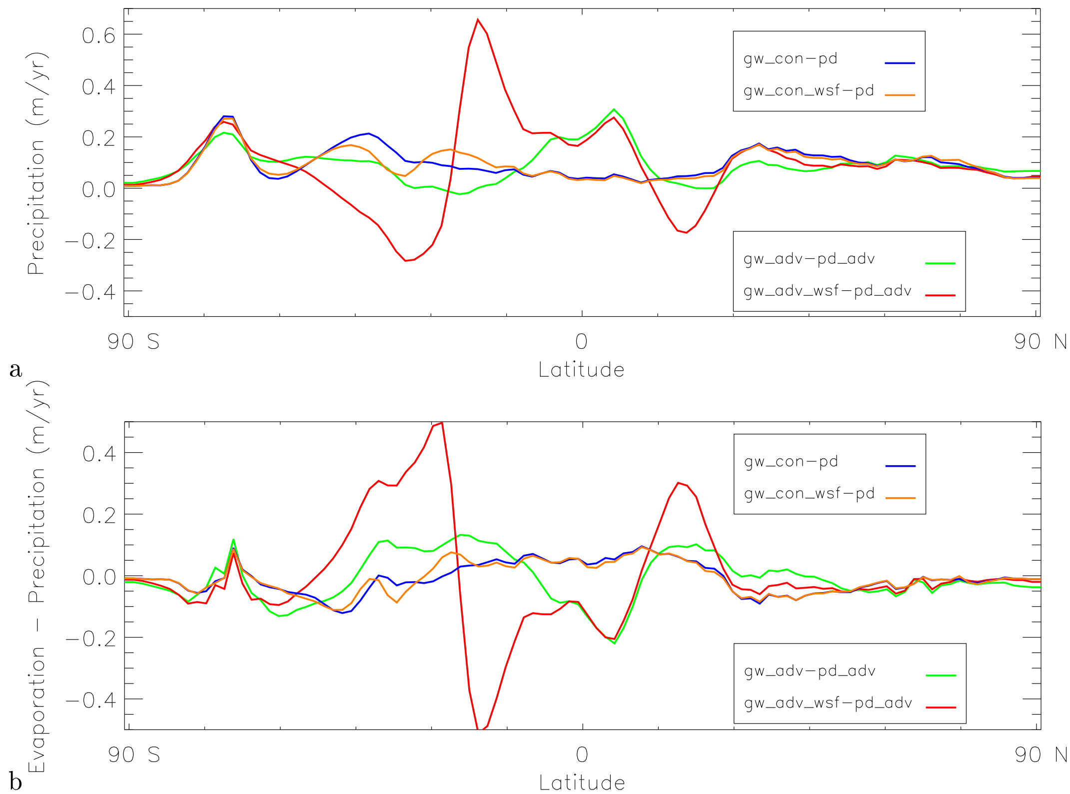

Figure 33: Zonally-averaged a) precipitation and b) evaporation minus precipitation at year 500 (relative to 1998; ’pd’ in legend) for the 4×CO_2 equilibrium global warming (’gw’ in legend) integrations. Moisture transport is either diffusive (’con’ in legend; blue, orange) or advective (’adv’ in legend; green, red) and the wind feedback is either on (’wsf’ in legend; red, orange) or off (blue, green).

Wiebe and Weaver (1999), using the Fanning and Weaver (1996) version of this model in which moisture transport was parametrised through diffusion, conducted very similar experiments to those performed here. They too found that the North Atlantic overturning re-established to a strength greater than the initial condition and quantitatively analysed why this was so. In the transient case, they found that the initial increase in high latitude precipitation (as seen in Figs. 33a and 34), and subsequent reduction of DISH gradient, was the cause of the initial thermohaline weakening (see Fig. 31b). As time went on, low latitude and South Atlantic heating increased the DISH and hence its meridional gradient so that the thermohaline circulation began to intensify to a new equilibrium that was stronger than its initial case (see also Manabe and Bryan (1985)).

Our two cases with a diffusive representation of moisture transport yield results that are very similar to those of Wiebe and Weaver (1999). When moisture advection is used without the wind feedback, the thermohaline circulation still equilibrates to a level which is slightly stronger than its initial condition. The fact that this

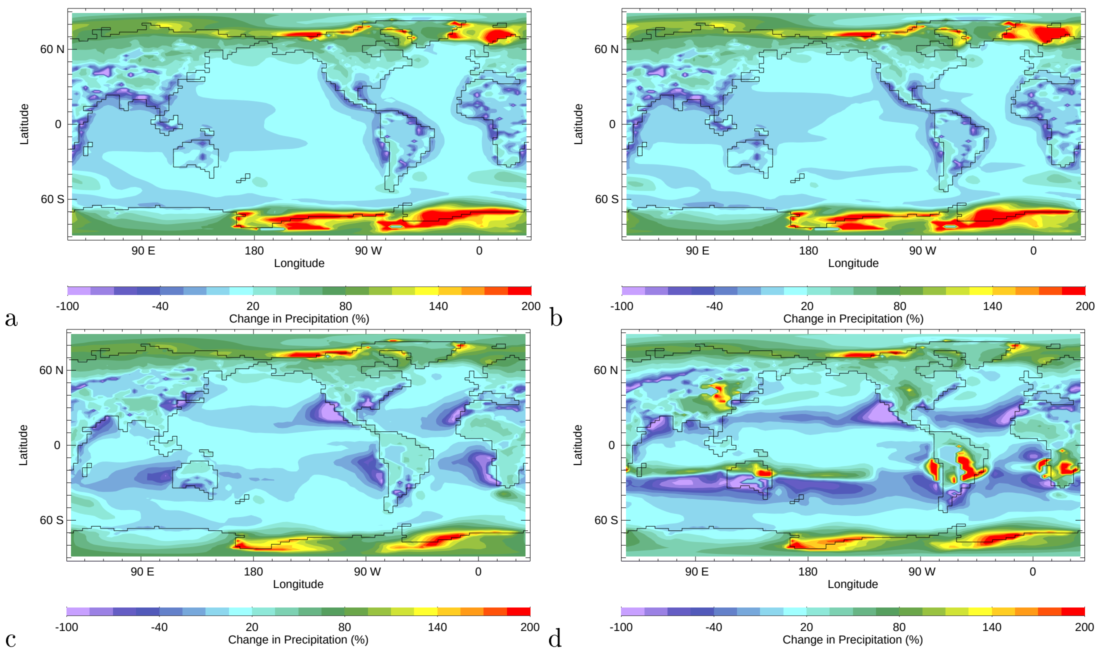

Figure 34: Percentage change in precipitation at year 500 (relative to 1998) for the $4\times CO_2$ equilibrium integrations. a)- Diffusive moisture transport; b)- Diffusive moisture transport with wind feedback; c) Advective moisture transport; d) Advective moisture transport with wind feedback.

is not the case when the wind feedback is used must arise from the improved representation of hydrological processes and their feedbacks in the atmosphere and ocean models. Figure 35a shows the meridional profile of the zonally-averaged DISH in the Atlantic Ocean for all the global warming runs and their respective initial conditions, relative to 1257 m. The difference between the zonally-averaged DISH at the latitude of the tip of Africa and the latitude of deep water formation is also shown as a function of the equilibrium overturning rate in Fig. 35b. The linear relationship between the strength of the overturning rate and the meridional gradient in the DISH is verified in our present experiments except perhaps for the experiment in which moisture transport is accomplished through advection and the wind feedback is included. This is particularly interesting as both the experiment with advective moisture transport without the wind feedback and the experiment with diffusive moisture transport with the wind feedback follow the same linear relationship. At this stage we are unaware why the combination of both advective moisture transport and wind feedback appears to lead to a scenario where the linear relationship breaks down.

The inclusion of moisture advection and the wind feedback brings the results of our model more in line with those found in coupled atmosphere-ocean models where a re-establishment to the initial condition is most often seen (e.g. Kattenberg et al. (1996); Manabe and Stouffer (1999)). This is a very encouraging feature as it provides additional indirect validation of our wind feedback parametrisation of section 2.1.1. Nevertheless, we are left with the puzzle as to why the simple linear relationship between the meridional DISH gradient in the North Atlantic

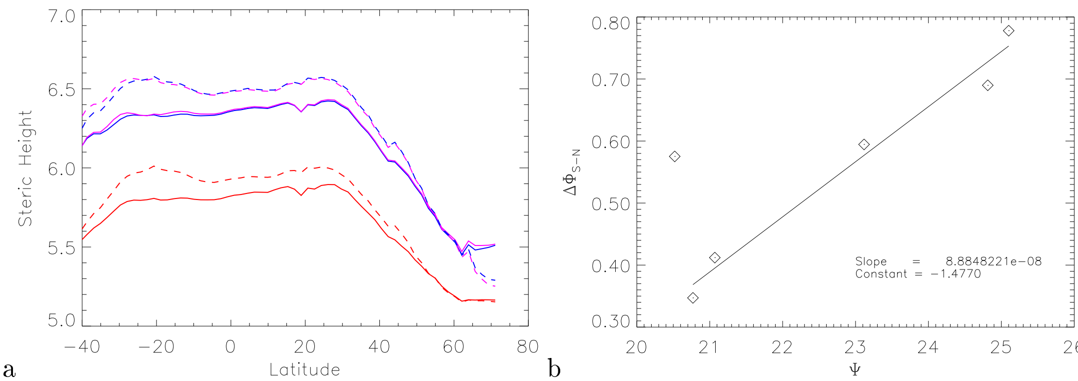

a b

Figure 35: a) Annual mean, zonally-averaged depth-integrated steric height in the Atlantic Ocean relative to level 9 of the model (1257 m). The dashed lines represent the integrations with diffusive moisture transport and the solid lines with advective moisture transport. Red curves are for the equilibrium present-day integrations whereas blue and purple lines are at year 500 (relative to 1998) for the global warming and global warming with wind feedback integrations, respectively. Units are in 10^{-6}kgm^{-1}. b) Difference between the zonally-averaged depth-integrated steric height in a) at the latitude of the tip of Africa (40°S) and the latitude of deep water formation (60°N), as a function of equilibrium overturning rate in Sv for all experiments. The equilibrium overturning rate for each experiment is taken from Fig. 31b, with the present day (red curves above) being represented by the 1998 initial conditions. The one outlier is for the experiment with moisture advection and the wind feedback. The straight line gives a least squares fit of all points except the one outlier.

and the strength of the conveyor appears to break down in this case. It is of course entirely possible that the small range of ψ found in Fig. 35b overemphasises any single point, and that had we examined the DISH/ ψ relationship from many more equilibria, the outlier would have been included within expected scatter around the best linear fit (as in Hughes and Weaver (1994); Thorpe et al. (2001)). We are currently designing a number of diagnostics to try and elucidate this issue and to put our results within the theoretical framework of Gnanadesikan (1999). At this stage it does not appear to be related to changes in the strength of the southern hemisphere winds (Toggweiler and Samuels 1995) since differences in the wind strength, and hence Ekman transport, between the two experiments with the wind feedback included are relatively small.

6 The Climate of the Last Glacial Maximum

As noted in the introduction, early CLIMAP Project Members (1976 1981) attempts to reconstruct SSTs for the LGM around 21 KBP have suggested that relative to the present, global SSTs were on average 1.7°C cooler in August and 1.4°C cooler in February. These reconstructions further suggested that tropical SSTs were similar to those of the present climate whereas in the North Atlantic, SSTs were substantially colder. While recent alkenone evidence (Sikes and Keigwin 1994; Bard et al. 1997; Lyle et al. 1992) also supports tropical SSTs only slightly cooler at the LGM, additional evidence is contradictory. For example, coral records from Barbados (Guilderson et al. 1994) and the southwest Pacific (Beck et al. 1997), ice core records from Peru (Thompson et al. 1995), noble gas measurements in Brazil (Stute et al. 1995) and ocean core records from the western equatorial Atlantic (Curry and Oppo 1997) suggest LGM tropical temperatures were significantly below those at present.

Modelling studies of the LGM have provided conflicting results concerning the issue of tropical cooling. Most early simulations used atmospheric general circulation models with either fixed SSTs or mixed layer ocean models at the lower boundary (Manabe and Broccoli 1985; Hansen et al. 1984; Lautenschlager and Herterich 1990; Kutzbach and Guetter 1986; Crowley and Baum 1997; Webb et al. 1997; Broccoli 2000). Webb et al. (1997) obtained tropical SSTs that were about 5.5°C cooler than today (averaged over the region 16°N to 16°S), substantially larger than CLIMAP estimates, using an AGCM in which present day oceanic heat transports were maintained. Broccoli (2000), on the other hand, obtained tropical SSTs that were 2.0°C cooler than present (averaged over the region 30°N to 30°S). Two previous studies using climate models of intermediate complexity (Ganopolski et al. 1998; Weaver et al. 1998) found their tropical temperatures to be cooler than CLIMAP, consistent with tropical alkenone reconstructions, but not as cool as some of the other reconstructions cited above. Bush and Philander (1998) on the other hand, using a coupled atmosphere-ocean GCM under LGM forcing, albeit for a short (15 year) integration by which time the deep ocean was still far from equilibrium, suggested 5°C tropical sea surface cooling.

Through a comprehensive analysis of the existing proxy record, Crowley (2000) questioned the validity of SST records obtained from ice-age coral proxies. In addition, he argued that small changes (on the order of 20%) in the assumed constant lapse rate, through which snow line proxies are projected to infer SSTs, could reconcile even CLIMAP data with tropical snow line proxies. Both he and Weaver et al. (1998) argue for more stable tropical SSTs which are colder than CLIMAP Project Members (1976 1981), consistent with alkenone reconstructions (Sikes and Keigwin 1994; Bard et al. 1997; Lyle et al. 1992), but not as cold as the borehole, coral and other reconstructions (Guilderson et al. 1994; Beck et al. 1997; Thompson et al. 1995; Stute et al. 1995; Curry and Oppo 1997) mentioned above. He proposed a mid-range LGM climate sensitivity of 3.0 °C for a doubling of CO_2, leading to a 2.5 °C reduction in ice-age tropical SSTs relative to the present. Both of these are almost exactly as inferred in Weaver et al. (1998).

In this section we reexamine the issue of LGM tropical cooling using our ESCM. This should be viewed as an extension of the analysis of Weaver et al. (1998) in which an older and less sophisticated version of the model was used. In our first experiment we set the orbital parameters to 21 KBP values and lower the level of atmospheric CO_2 to 200 ppm. The topography on land was also raised through the use of the Peltier (1994) ICE4G reconstruction, and wherever continental ice sheets were present, the planetary coalbedo was locally reduced by 0.18. The coupled system was then integrated for 2000 years until an equilibrium was reached, using the present-day climate of section 3 as the initial condition .

The global mean cooling for the LGM relative to the present is 3.6 °C, of which 0.4 °C arises solely due to the increased elevation associated with the prescribed ice sheet thickness. The SAT difference (Fig. 36) shows a pronounced cooling around the region of the North Atlantic, where the prescribed ice sheets are present, that is amplified due to a weakening and shallowing of the meridional overturning, the southward expansion of sea ice and the subsequent sea-ice albedo feedback over the ocean. On average the northern hemisphere is 4.6 °C colder than the present, whereas in the southern hemisphere, where there are fewer areas of land and ice sheets, this cooling is only 2.6 °C. Our global cooling estimate lies within the range spanned by other AGCM and coupled model studies (e.g. (Hansen et al. 1984; Lautenschlager and Herterich 1990; Kutzbach and Guetter 1986; Broccoli and Manabe 1987; Broccoli 2000; Hyde et al. 1989; Ganopolski et al. 1998; Bush and Philander 1998)).

As in Weaver et al. (1998), the equilibrium LGM North Atlantic overturning (Fig. 37a) is reduced in intensity and shallower in depth compared to the present-day climatology (Fig. 18a). For example, the maximum overturning at the LGM is ∼10 Sv, about half of the 19-20 Sv found in the present-day equilibrium climate (Fig. 37b), and the base of the NADW layer is on average a few hundred metres shallower south of 25°N. Antarctic Bottom Water, originating in the Southern Ocean, penetrates further northward to about 25°N in the LGM case (Fig. 37a), filling the void left behind by the shallower NADW layer. The actual location of NADW formation did not change noticeably and North Pacific Intermediate Water (NPIW) did not intensify, consistent with Weaver et al. (1998).

The sea-ice distribution in the LGM experiment (solid line in Figs. 36d,e) shows a rather dramatic seasonal variation in ice cover over the North Atlantic. In the winter, sea ice covers the Labrador Sea and extends across the North Atlantic to Great Britain (see Crowley and North (1991) p.49). In the summer, much of this sea ice melts away leaving most of the North Atlantic ice free, in accord with Hebbein et al. (1994). The maximum sea ice extent at any time of the year (Fig. 38) shows that although we include a much more sophisticated dynamical/thermodynamical sea ice model (section 2.2.1), results are quite similar over the ocean to those of Weaver et al. (1998). In the southern hemisphere, our maximum sea ice extent agrees well with the Crosta et al.

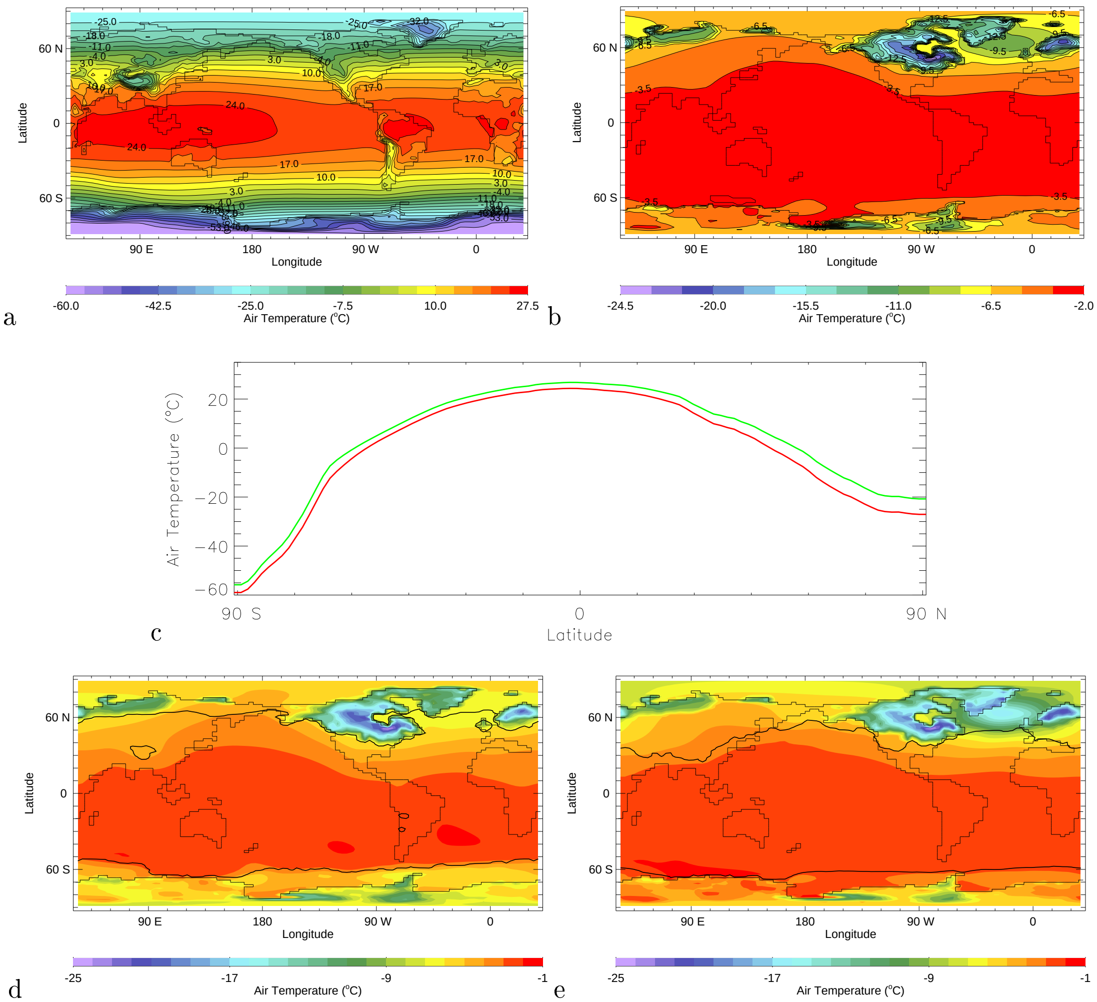

Figure 36: Equilibrium annual mean surface air temperature for the a) LGM, b) LGM minus present day (Fig. 10a) climatologies. c) zonally-averaged annual mean LGM (red) and present-day (green) surface air temperature profiles. d) Summer (July through September) and e) Winter (January through March) mean average surface air temperature differences for the LGM relative to the present day climatology. The solid black line in d) and e) indicate the seasonal average 10% concentration of sea ice over the ocean and snow coverage over land.

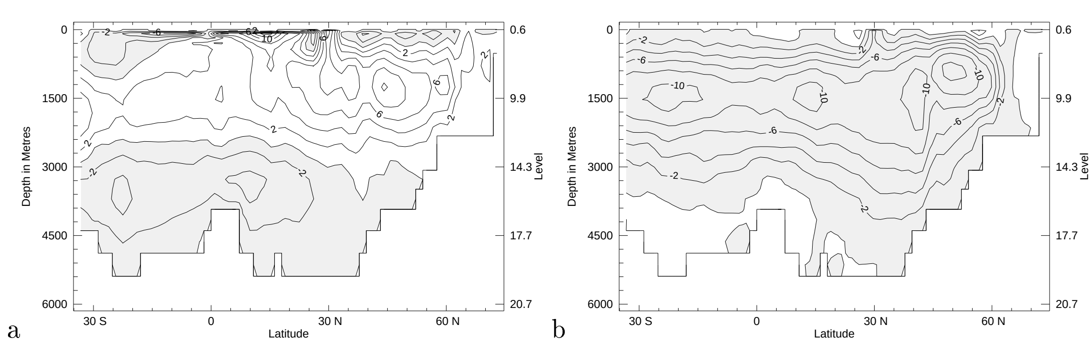

Figure 37: a) North Atlantic meridional overturning streamfunction for the LGM equilibrium climate. b) Difference between a) and that obtained for the present-day climate (Fig. 18a). The contour interval is 2 Sv.

(1998ab) proxy data, although we appear to have too little sea ice between Antarctica and Australia. As noted in section 3.3, very little sea ice forms in this region in our model due to the Antarctic Circumpolar Current being steered too far south by the Kerguelen plateau and bringing relatively warm waters poleward.

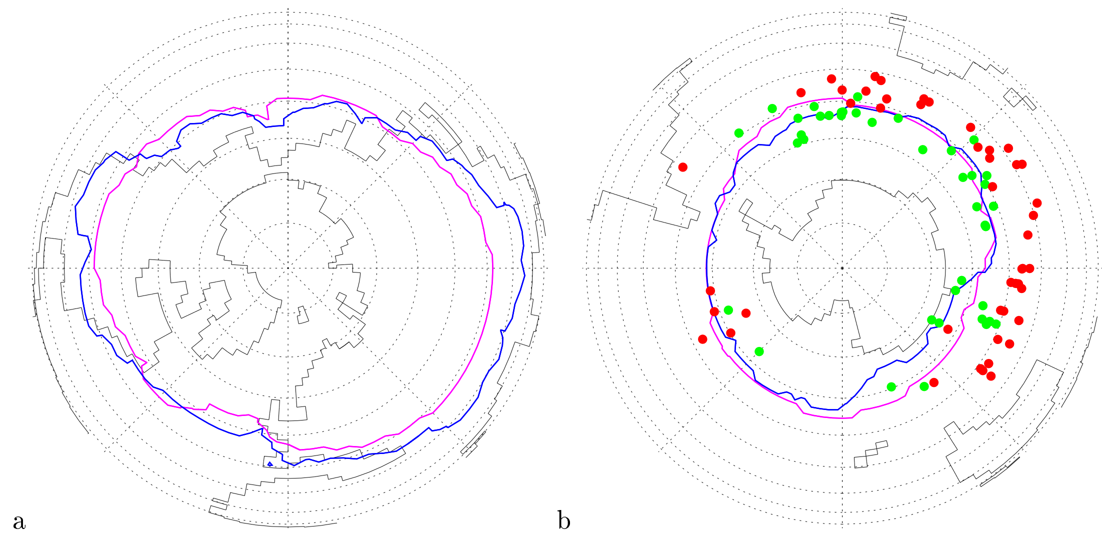

Figure 38: Maximum equilibrium annually-averaged extent of sea ice (over the ocean) and snow (over the land) for the LGM climatology (blue) in the a) northern and b) southern hemispheres. The pink line represents the same field for Weaver et al. (1998). In the southern hemisphere, the dots indicate where the Crosta et al. (1998ab) paleo reconstruction of maximum sea ice extent suggests the presence (green) and absence (red) of sea ice.

The LGM SST field (Fig. 39a) and its difference from the present day climate (Fig. 39b), show cooling everywhere in the ocean with a global and annual mean amount of 2.1°C. Averaged between 20°S and 20°N, tropical cooling is also 2.1°C, which is colder than that suggested by CLIMAP Project Members (1976 1981), yet consistent with alkenone reconstructions (Sikes and Keigwin 1994; Bard et al. 1997; Lyle et al. 1992; Rostek et al. 1993), but not as cold as the borehole, coral and other data mentioned earlier. The tropical cooling varies within and between basins in the 20°N–20°S band, with range from 2.9-1.7°C in the Atlantic Ocean, 1.9-2.3°C in the Indian Ocean, and 1.8-2.6°C in the Pacific Ocean. The tropical Pacific is particularly interesting as there is an east-west asymmetry to the cooling with western tropical Pacific SSTs only about 1.8-1.9°C cooler and eastern tropical Pacific SSTs 2.2-2.3°C cooler than today, suggesting that LGM Pacific SSTs are similar to permanent La Niña conditions. The LGM SST cooling is amplified in the North Atlantic, associated with a weakening and shallowing of the conveyor, with a maximum cooling of 8.0°C. Generally, the global SST fields are qualitatively similar to those found in Weaver et al. (1998) and are in excellent agreement with those inferred from alkenone reconstructions (Sikes and Keigwin 1994; Bard et al. 1997; Lyle et al. 1992; Rostek et al. 1993; Ikehara et al. 1997; Schneider et al. 1995; Chapman et al. 1996).

The reduction and shallowing of the overturning in the North Atlantic, together with the surface cooling, leads to a redistribution of water mass properties in the global ocean. For example, the more northward penetration

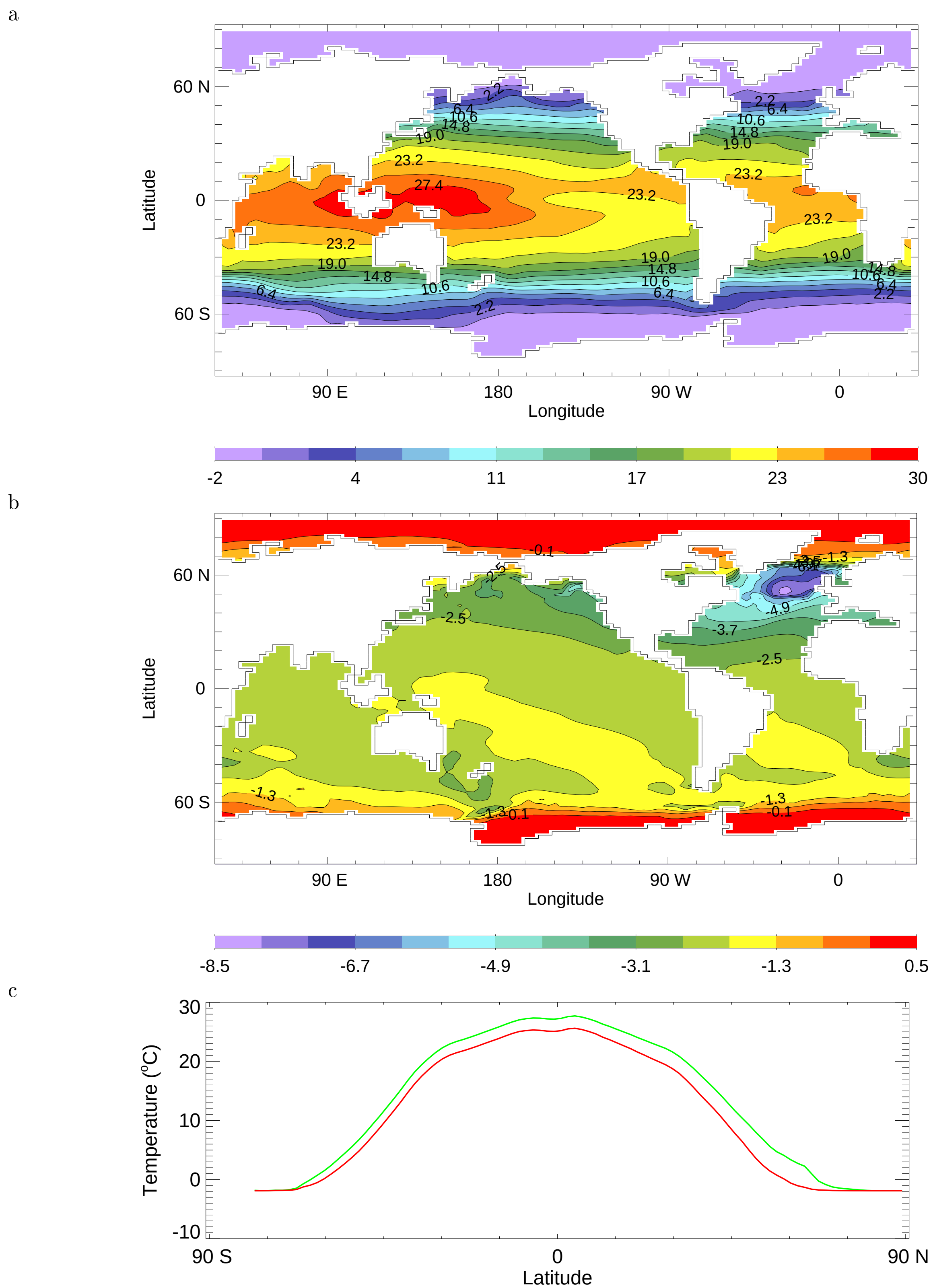

Figure 39: Equilibrium annually-averaged sea surface temperature for a) the LGM, b) the difference between the LGM and the present (LGM - PD). c) zonally-averaged LGM (red) and PD (green) equilibrium sea surface temperature climatologies.

of AABW, which is cold relative to the displaced NADW, leads to a local maximum in cooling in the deep North Atlantic around 30°N (Fig. 40b). Maximum cooling, of course, occurs in the thermocline regions of the global oceans (Fig. 40a), although most of the deep ocean is still 0.7-0.9°C cooler than for the present day climatology.

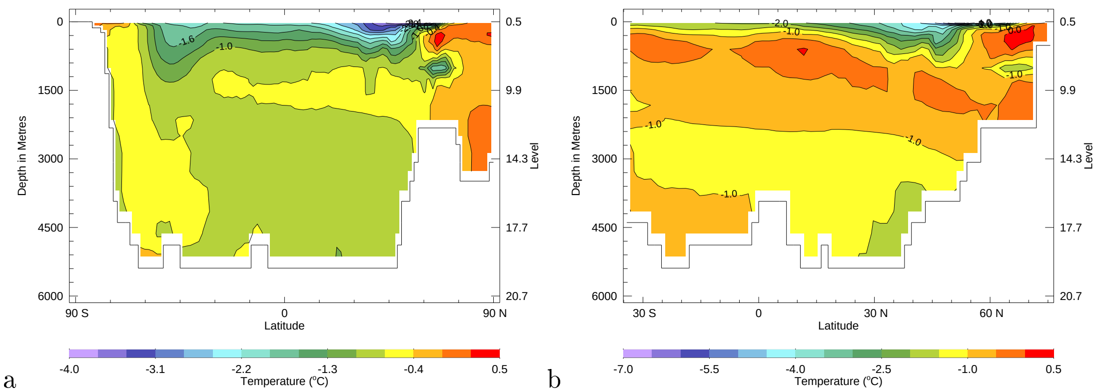

Figure 40: LGM minus present-day annual zonally averaged ocean temperature difference (°C) a) global and b) North Atlantic.

In the region of the NADW water mass (Fig. 40b), there appears to be a minimum in the zonally-averaged cooling relative to water masses below and above. Figure 41 shows the rather fascinating result that the minimum is the result of a cooling anomaly in the eastern Atlantic, up to 4.4°C at 600 m, being balanced by warm anomalies (up to 0.9°C) in the western Atlantic, most notably in the Labrador Sea and near equatorial regions. The analysis of the LGM fields suggests that the warm anomaly that develops in the Labrador Sea is due to the sea ice cover insulating the ocean from the atmosphere. As such, convection is reduced relative to the present and relatively warm subsurface waters are not mixed with relatively cold surface waters, leaving a warm anomaly behind. In the equatorial region, there is a substantial drop in the cross-equatorial transport (see near vertical contours in Fig. 37a in the upper 2000m near the Equator) of heat and salt. Relatively warm subsurface equatorial waters are therefore not efficiently transported out of the region towards the North Atlantic, leaving a warm anomaly behind. This same process leads to the local maximum in cooling in the eastern Atlantic, as the reduced thermohaline circulation and hence Gulf Stream and North Atlantic drift, does not bring in as much heat to the region.

In order to compare model-derived and CLIMAP SST estimates, we subtract the CLIMAP present day and LGM reconstructions for February (winter) and August (summer), and do the same for the model fields (here winter and summer are defined as January through March and July through September, respectively). The difference between these proxy and model difference fields (Fig. 42) reveals that in both the summer and the winter, we find significantly more cooling in the subtropical North and South Pacific and South Atlantic. These subtropical gyre regions are in fact places where CLIMAP data suggests a modest LGM warming relative to the present. Over much of the North Atlantic our model-derived LGM SST cooling is less than that inferred by CLIMAP, although a portion of this difference is certainly related to the slightly cooler SSTs in our present-day

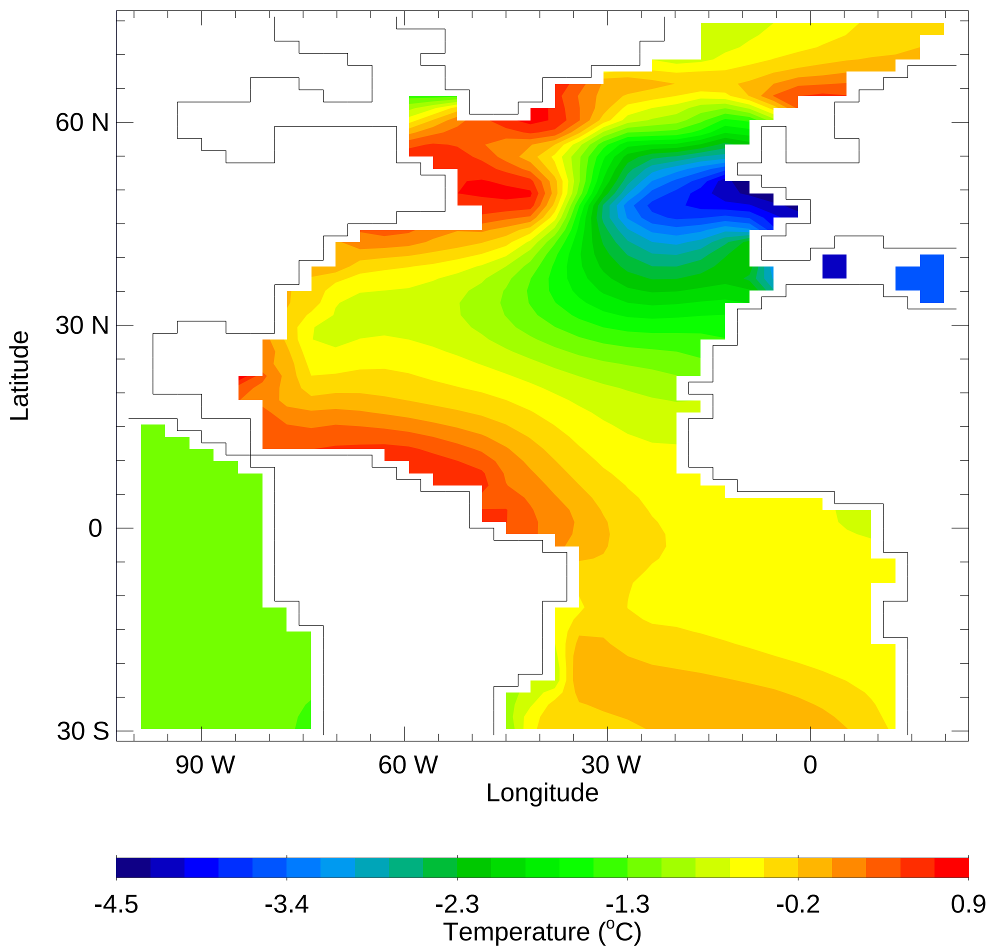

Figure 41: Difference between LGM and present day potential temperature at a depth of 600 m.

climate (Fig. 14b). This follows since the possible LGM cooling is bounded below by the freezing point of water, and over much of the high latitude North Atlantic sea ice is present at least in the winter. In the Southern Ocean we also find a general tendency for the model to yield less cooling than CLIMAP, although there are large regions where the model fields are in fact cooler than CLIMAP. Averaged over the band 20°S to 20°N, our model-derived SSTs are 0.9°C colder than CLIMAP in the summer and 1.5°C cooler in the winter.

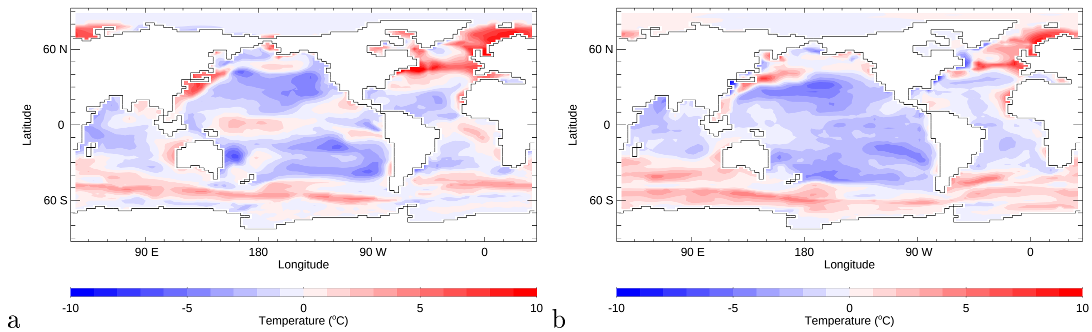

Figure 42: Anomaly maps showing the difference between the model and CLIMAP Project Members (1976 1981) sea surface temperature changes between the LGM and the present. a) Summer; b) Winter.

In order to see whether or not the ICE4G reconstruction was a stable initial condition within our coupled model, an additional integration was performed in which the specified ice sheets were allowed to melt or grow. Snow was allowed to accumulate to a maximum of 10m on top of the existing ice sheet and any further increase in snowfall raised the height of the ice sheet by the additional amount. Similarly, once all the snow on the ice sheet melted, the ice sheet was also allowed to melt at the same melting rate (section 2.2). As we did not include ice sheet dynamics in this experiment (but see section 2.2.6 and Yoshimori et al. (2001)), the ice sheet was not allowed to grow any more than the ICE4G reconstruction and snow was not allowed to accumulate to more than 10 m. Any excess snow fall on the ice sheet was directly passed to the ocean through the appropriate river drainage basin. Freshwater fluxes associated with ice sheet growth and melt were not passed to the ocean model as we were focussed solely on thermodynamical feedbacks, although snow melt/accumulation was accounted for in the freshwater budget (as discussed in section 2.2).

When the ice sheet is allowed to adjust, as discussed above, it reduces in extent in many regions. Most notably, the Laurentide ice sheet in Central North America melts back slightly, whereas the northern Eurasian ice sheet almost completely disappears. With respect to the latter, there has been some question as to whether or not the ICE4G reconstruction of Peltier (1994) is in fact realistic there (e.g. Sher (1995)). The LGM global mean SAT cooling, relative to the present, drops by 0.6 °C to 3.0 °C from the case where the ice sheet is held fixed for two reasons. First, in regions where the ice sheet melts away, the surface temperature drops through elevation effects (accounting for 0.25°C of the decrease). In addition, in regions where ice sheets existed year round, there was a continual albedo feedback which would not be present in the summer; for example, if the ice sheet were to melt away (accounting for 0.35°C of the decrease). Nevertheless, it is reassuring that the major portions of both the Laurentide and Fennoscandian ice sheets, as well as the Greenland and Antarctic ice sheets, remain stable. The timescale for ice sheet evolution is, of course, many thousands of years so we should not expect the ICE4G reconstruction to be in equilibrium with the LGM radiative forcing, but rather to be in a continual state of adjustment as it moves towards the last glacial termination. As such, we would not expect our equilibrium climatology to agree precisely with the Peltier (1994) reconstruction.

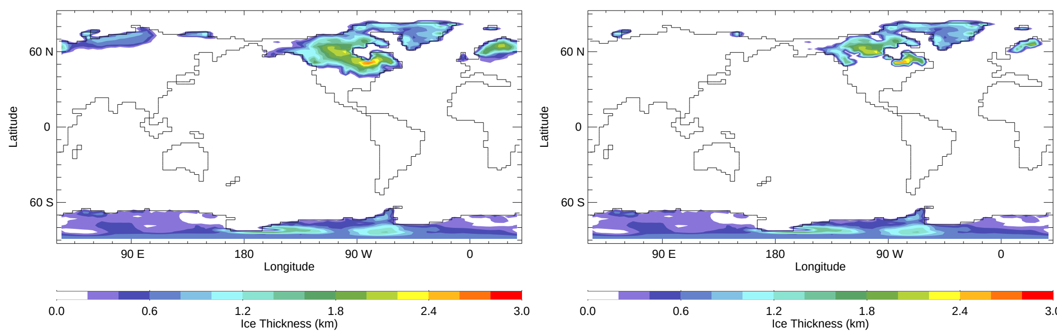

Figure 43: LGM annually-averaged land ice thickness greater than the present day bed topography a) initial condition (reconstruction) and b) at equilibrium after release from the initial condition.

For completeness we now test what role, if any, the inclusion of the wind feedback parametrisation has on the LGM climate. To accomplish this task we calculate SAT anomalies, defined as departures from the present-day SAT field (Fig. 10a), in an experiment that starts at the end of the LGM experiment with prescribed ice sheets. The coupled model is integrated to a new equilibrium with the wind feedback continually being calculated (section 2.1.1). The equilibrium wind stress anomaly field (Fig. 44a) reveals enhanced westerlies in the midlatitude belt of the southern hemisphere, arising from a greater meridional surface pressure gradient, and an anticyclonic anomaly centred over the North Atlantic. The anticyclonic anomaly develops in response to local cooling associated with a reduced overturning as in (Manabe and Stouffer 1988; Fanning and Weaver 1997b). Globally, the resulting wind anomalies have negligible effect on LGM cooling (Fig. 44b) contributing only an additional 0.03 °C. A similar negligible effect was found by Weaver et al. (1998).

While the present model is much more sophisticated than the one used by Weaver et al. (1998), there are still many feedbacks which have not been accounted for in our simulations. For example, the radiative forcing associated with atmospheric aerosols and clouds are both ignored. In the case of aerosols, it is not clear what the spatial pattern nor sign and magnitude of this radiative forcing would be in terms of both aerosol type and distribution. Estimates from Peru (Thompson et al. 1995) suggest that LGM atmospheric dust levels may have been 200 times the present whereas in Antarctica they may have been 4-6/10-30 times the present for marine/continental aerosols, respectively (Petit et al. 1981). In the case of clouds, one would expect a reduced cloud cover in the drier LGM atmosphere (Hansen et al. 1984), although the incorporation of this effect in our

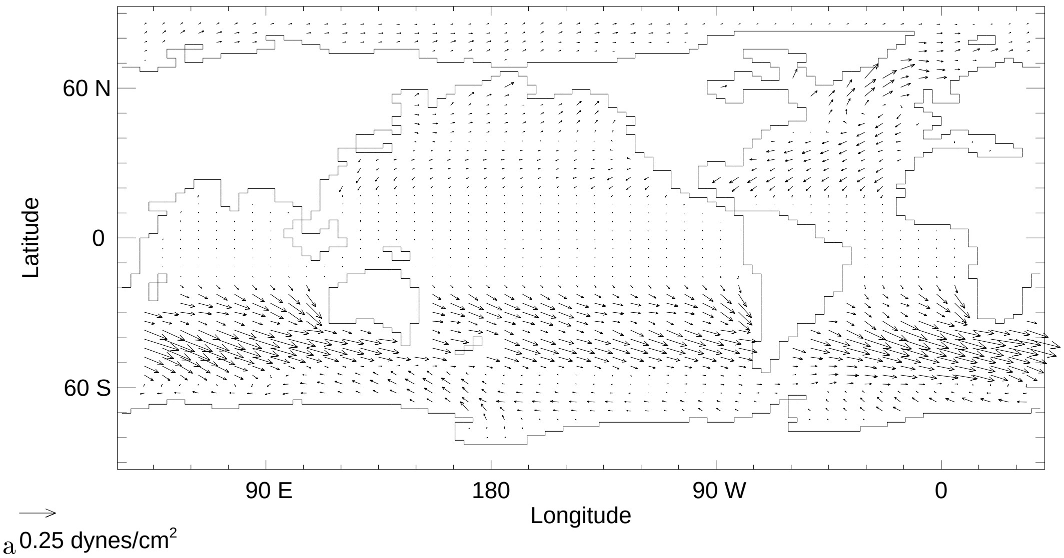

a

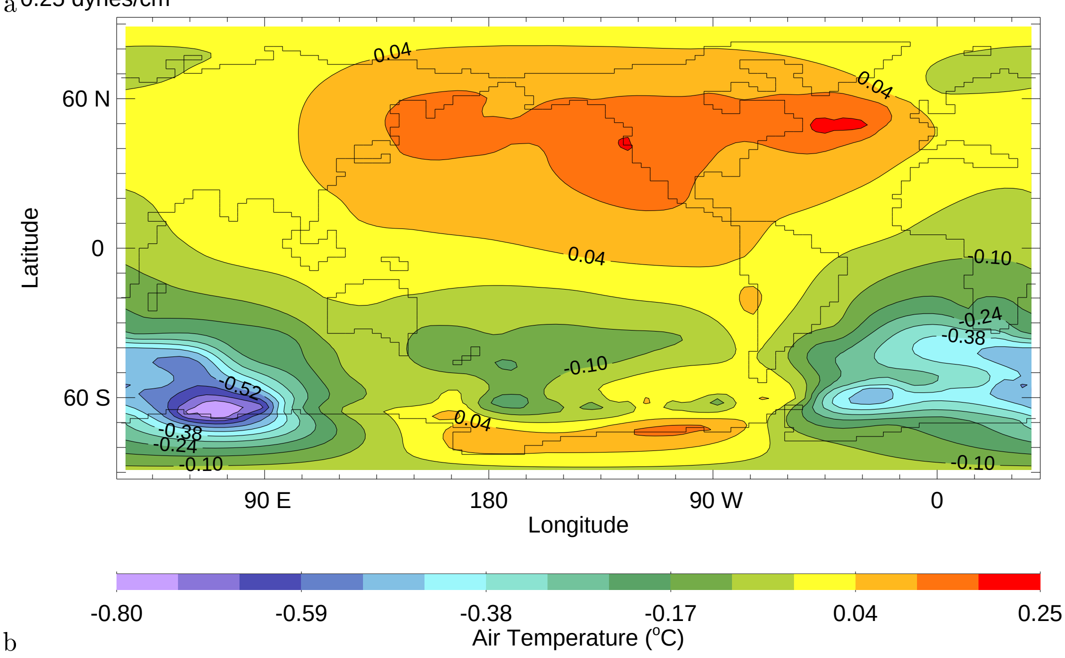

b

Figure 44: a) Equilibrium LGM wind stress anomaly from the parametrisation of section 2.1.1 and b) the equilibrium annually-averaged surface air temperature difference between a model with the parametrisation and one without. Every second vector is shown in a).

model would be difficult and perhaps inconsistent with its present level of sophistication. Vegetation feedbacks and subsequent albedo changes through the expansion of dryland vegetation in Australia and Africa and the conversion of conifer to tundra in Europe and Siberia have also been suggested to enhance the cooling there (Crowley and Baum 1997). As noted in section 8, we are presently attempting to incorporate land surface and dynamic vegetation subcomponent models into our ESCM of intermediate complexity, but it is not yet possible to account for their effects. Finally, we have not accounted for the estimated 121 ± 5 m drop in sea level at the LGM (Fairbanks 1989) through our use of present-day land-sea geometry in all experiments. This was done intentionally, however, so that we might perform a clean comparison with analogous present-day integrations. The LGM global mean salinity increase of about 1 psu arising from the reduced sea level, has been shown to have little effect on the climate of the LGM Weaver et al. (1998).

Nevertheless, with these limitations in mind, our LGM experiments serve as a useful validation tool for the ESCM. Several paleo proxy studies (Boyle and Keigwin 1987; Lea and Boyle 1990) have inferred a shallowing and others (Curry and Lohmann 1983; Oppo and Fairbanks 1987; Charles and Fairbanks 1992; Charles et al. 1996) a weakening of NADW at the LGM, both of which are borne out in the model results. In addition, a recent study (Rutberg et al. 2000) has inferred a reduced flux of NADW into the Southern Ocean, a feature also seen in our model solutions.

Our LGM climate cooling of 3.6°C relative to the present is within the range spanned by previous modelling studies. If we also account for the fact that global sea level was about 120 m lower than today (Fairbanks 1989), and note that our model incorporates a specified lapse rate of 6.5°C/km, then our LGM SAT cooling over land is 4.4°C , so our global SAT cooling is 3.8°C. Averaged between 30°S and 30°N, tropical cooling is about 2.1°C over the oceans, and again, if we account for the sea level drop, 3.6°C over the land. These are generally cooler than CLIMAP estimates, but not as cool as some other reconstructions. Globally our model SSTs are in good agreement with alkenone reconstructions and are generally cooler than those of CLIMAP in the tropical ocean, while not as cool in the North Atlantic. Our model results also suggest that CLIMAP estimates in the subtropical gyres may be in error, especially since they infer a net LGM warming there relative to the present. As noted by Crowley (2000) and Weaver et al. (1998) it is possible for us to reconcile a more stable tropics (colder than CLIMAP, consistent with alkenone reconstructions but not as cold as the borehole, coral and other reconstructions mentioned earlier) with the results of our, and other, modelling studies if the climate sensitivity in nature is low-to-moderate and CLIMAP temperatures represent a slight underestimation of LGM cooling.

7 Climate Model Evaluation and the Long Timescale Memory of the Ocean

The most common way of evaluating an ocean or coupled climate model is to spin it up under perpetual present-day forcing and subsequently to compare the model climatology with present-day observations. Implicit in this approach is the assumption that the present-day observations are in equilibrium with the present-day forcing. The validity of this assumption is questionable as it is well known that the ocean, with its large thermal inertia, takes hundreds to thousands of years to equilibrate to its prescribed surface forcing. As such, changes in radiative forcing over recent Earth history are likely to have a signature in at least the deep ocean.

Weaver et al. (2000) provided some support for this notion through the analysis of integrations conducted using an earlier version of our coupled model. They compared the results from a transient integration forced by time-varying atmospheric CO_2 and orbital forcing, starting at 6 KBP, with equilibrium simulations obtained under perpetual 1850 (preindustrial) and 1998 (present-day) atmospheric CO_2 concentrations and orbital parameters. Substantial differences were found between the equilibrium climatologies and the transient simulation, even at 1850 (in weakly ventilated regions), prior to any significant changes in atmospheric CO_2. When compared to the present-day equilibrium climatology, differences were large: the global mean SATs and SSTs were $\sim$0.5°C and $\sim$0.4°C colder, respectively, deep ocean temperatures were substantially cooler, southern hemisphere sea ice cover was 38% larger, and the North Atlantic conveyor 16% weaker in the transient case. These differences were due to the long timescale memory of the deep ocean to climatic conditions which prevailed throughout the late Holocene, as well as to its large thermal inertia.

The coupled modelling community has in some sense realised this potential problem, although it has been framed within a different context. It has been shown that climate models which do not account for the 20th century build up of atmospheric CO_2 through long integrations from, say, 1850, suffer from a cold start problem (Fichefet and Tricot 1992; Hasselmann et al. 1993; Cubasch et al. 1994; Keen and Murphy 1997), whereby the initial rate of warming is slower than it should otherwise be (see Kattenberg et al. (1996)). This follows since the initial conditions for such experiments are in radiative equilibrium with their forcing, whereas a transient experiment starting from preindustrial times has a warming commitment (Keen and Murphy 1997), as it has yet to reach radiative equilibrium. Using the same earlier version of our model, Weaver et al. (2000) also demonstrated that a cold start global warming simulation (starting from a 1998 equilibrium climatology) underestimates the global temperature increase at 2100 by $\sim$10%.

In this section we extend the analysis of Weaver et al. (2000) in two ways. First, we allow for changes in solar forcing through the use of the Lean et al. (1995) reconstruction of solar irradiance; second we conduct the experiments with an improved model that includes more sophisticated sea ice and atmospheric components. In particular, as sea ice plays an important role in amplifying the response of the climate system to radiative forcing perturbations, we are able to quantify whether or not the analysis of Weaver et al. (2000) is sensitive to the representation of sea ice processes.

7.1 Experimental Design

Seven experiments were conducted with the coupled model (Table 4). The first three experiments consisted of spinning up the model from rest to equilibrium under 6 KBP, 1850 and 1998 orbital parameters and atmospheric CO_2 levels, and a solar constant of 1368 Wm^{-2}. Atmospheric CO_2 levels of 280 ppm (Barnola et al. 1987) were used in the preindustrial 6KBP and 1850 cases, while a modern level of 365 ppm was used in the 1998 case. The radiative forcing associated with the orbital parameters at the three time slices (Fig. 45) shows insignificant changes between 1850 and the present. As mentioned earlier, variations over longer timescales do not greatly affect the annual mean insolation but rather have more impact on the seasonal and latitudinal distribution of this insolation (Fig. 45). These seasonal and latitudinal changes can then be amplified within the climate system through, for example, changes in the intensity and location of wintertime oceanic convection, and changes in sea ice extent (and subsequent albedo feedback). Increased northern hemisphere insolation and decreased southern hemisphere insolation in the northern hemisphere summer and winter, respectively, are apparent at 6KBP relative to the present. Atmospheric CO_2 levels, on the other hand, have a more substantial influence on the annual mean radiative forcing. These three experiments are hereafter referred to as 6KBP, PI and PD, respectively (Table 4).

The PD and PI equilibrium climatologies were used as initial conditions for two global warming experiments representing the cold start (GWcs in Table 4) and what we term the 'luke warm' start (GWlws in Table 4), respectively. In the case of the luke warm start, the atmospheric CO_2 concentration $C(t)$ was increased according to

$$C(t) = C_{PI} e^{k(t-1850)^a} \tag{60}$$

where $C_{PI} = 280$ ppm, $k = 7.944 \times 10^{-8}$, $a = 3.0058$ and t is the year. This exponential fit was obtained from a two parameter fit (k and a) using the observed 1850-1990 increase in atmospheric CO_2 and other greenhouse gases that was used by Mitchell et al. (1995) in UKMO global warming simulations. The parameter a was subsequently retained although k was recalculated by demanding that the CO_2 levels at 1998 matched observations (365 ppm). The GWlws experiment, as well as the GWcs experiment were both extended out to year 2500 with atmospheric CO_2 increasing at 1%/year, until it reached levels 4 times the present (about year 2138), upon which time atmospheric CO_2 levels were held fixed. The wind feedback of section 2.1.1 was used in all these experiments.

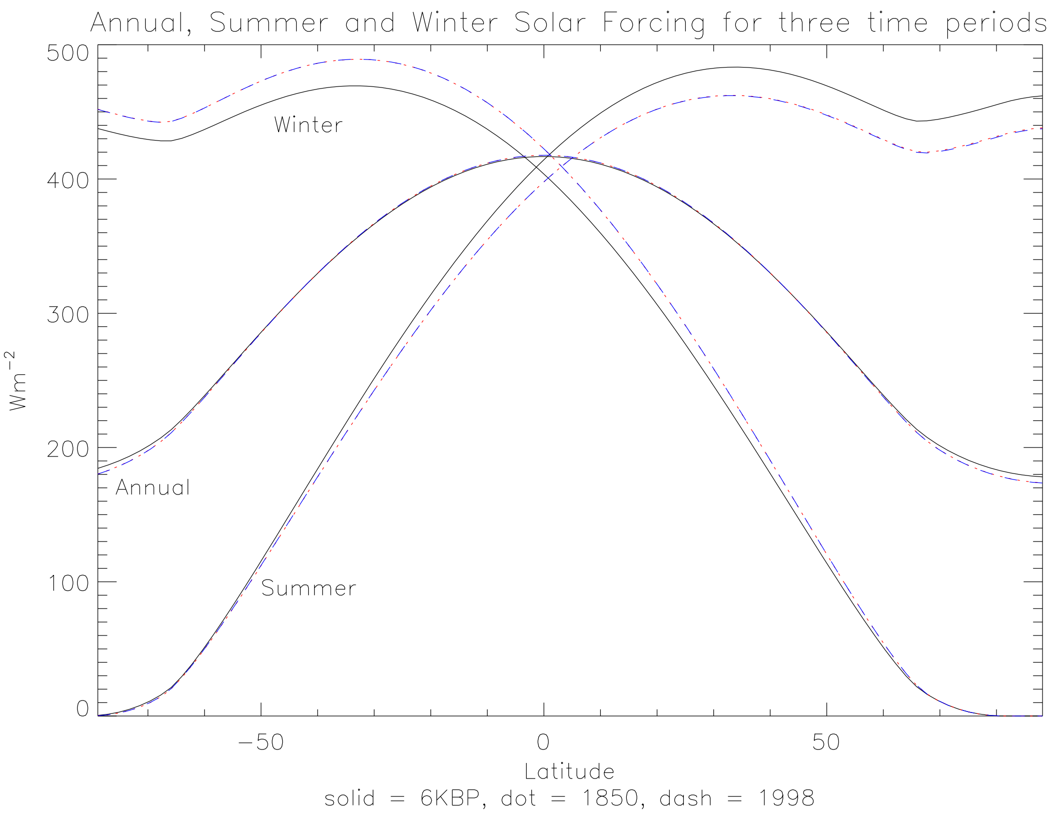

Figure 45: Zonally-averaged annual, summer and winter mean profiles of top of the atmosphere incoming solar radiation (W m^{-2}) at 6KBP (solid black), 1850 (red dotted), 1998 (blue dashed).

#	Experiment	Global Mean T (°C)	Atlantic Mean T (°C)	Atlantic Mean S (psu)	Global Mean SST (°C)	Global Mean SAT (°C)	Maximum Atlantic Ψ (Sv)	NH ice area 10^6 km^2	SH ice area 10^6 km^2
1	6KBP	3.41	5.3	34.85	17.38	12.73	20.84	11.21	13.92
2	PI (I850)	3.43	5.33	34.85	17.44	12.76	20.51	14.03	11.64
3	PD (1998)	4.00	5.96	34.87	18.38	14.08	20.96	10.55	11.09
4	PItr-PI	-0.02	0.011	.0020	-0.02	-0.01	-0.09	-0.07	0.18
5	$\triangle S_0$	-0.09	-0.083	.0025	-0.24	-0.30	0.04	0.22	0.69
6	PDtr-PD	-0.50	-0.53	-0.011	-0.45	-0.61	-1.27	0.49	2.15
7	$\triangle S_0$	-0.57	-0.62	-0.013	-0.55	-0.74	-1.09	0.59	2.49
8	GWcs-GWtr	0.37	0.35	0.0028	0.22	0.30	0.70	-0.17	-1.76
9	$\triangle S_0$	0.41	0.41	0.0044	0.26	0.35	0.81	-0.03	-0.21
10	GWlws-GWtr	0.012	0.001	-0.0010	0.0032	0.0018	-0.01	-0.01	-0.03
11	$\triangle S_0$	0.059	0.056	.00059	0.038	0.053	0.10	-0.03	-0.21
12	GWcs-PD	0.41	0.40	0.01	2.24	3.05	-0.81	-2.30	-3.39
13	GWlws-PDlws	0.54	0.58	0.02	2.47	3.35	-0.30	-2.63	-3.79
14	GWtr-PDtr	0.55	0.58	0.02	2.47	3.35	-0.24	-2.62	-3.77
15	$\triangle S_0$	0.57	0.61	0.02	2.54	3.44	-0.53	-2.69	-3.94

Table 4: Summary of diagnostics from the model experiments. The second column gives the experiment while subsequent columns portray results from the equilibrium simulations (rows 1 through 3; the row number is given in the first column) as well as differences between the transient and the equilibrium experiments at 1850 (row 4) and 1998 (row 6). Rows 5 and 7 are analogous to rows 4 and 6 except solar forcing is allowed to vary. Row 8 shows the difference at 2100 between the cold start experiment (GWcs) and the continuation of the transient experiment to year 2100 (GWtr), while row 9 shows the same thing but for the case with varying solar forcing. Rows 10 and 11 are the same as rows 8 and 9 but for the 'luke warm' start experiment (GWlws). The cold start, luke warm start, and transient experiment differences from their initial condition (PD, PDlws and PDtr, respectively) at 2100 are given in rows 12 -14, respectively. Row 15 is the same as row 14 but for the case with varying solar forcing. Global and Atlantic mean potential temperature and salinity are given in columns 2 through 4. As salinity is conserved in the coupled model, changes in global mean salinity are small and hence not shown. Minor differences would be reflected in northern (column 9) and southern (column 10) hemisphere sea ice areas or changes in atmospheric storage. The global mean sea surface and surface air temperatures are listed in columns6 and7 while the maximum value of the North Atlantic overturning streamfunction is given in column 8. Note that in column 2, experiments with PI, PD, or GW as a prefix imply results are taken at year 1850, 1998 and 2100, respectively.

The results from these experiments are compared at year 2100 with those obtained from two transient experiments which began at 6KBP. From 6KBP to 1610, these two transient experiments were identical with atmospheric CO_2 fixed at 280 ppm and orbital forcing varying according to Berger (1978). At 1610 they diverged with one retaining a fixed solar constant and the other allowing it to vary (Fig. 46). From 1850 to 1998 both experiments allowed atmospheric CO_2 to vary according to Eq. 60. The transient constant and varying solar forcing experiments at 1850 (PItr and PItr ΔS_0, respectively) as well as at 1998 (PDtr and PDtr ΔS_0, respectively) were subsequently compared to the equilibrium climatologies PI and PD in order to determine to what extent the climate system retains a memory to prior radiative forcing. These two experiments were also integrated to 2100 with CO_2 increasing as in GWlws and GWcs and are denoted GWtr and GWtr ΔS_0 in Table 4, respectively. In the case of GWtr ΔS_0, the solar constant after year 1998 was held fixed at 1368 Wm^{-2}, while in both cases, the wind feedback was once more in effect. The GWtr run was further extended to year 2500, as in the case of GWlws and GWcs, with atmospheric CO_2 increasing at 1%/year, until it reached levels 4 times the present (about year 2138), at which time atmospheric CO_2 levels were held fixed.

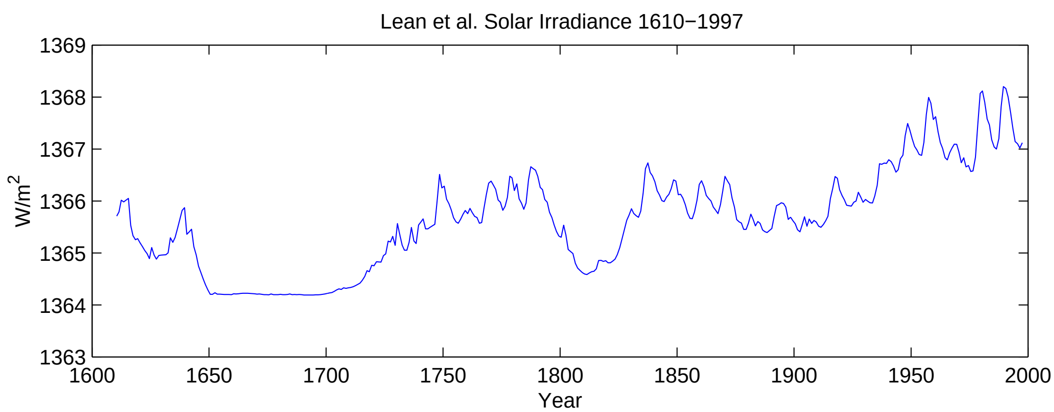

Figure 46: Lean et al. (1995) Solar irradiance (1610-1997) used in the transient integration with varying solar forcing.

7.2 Transient versus Equilibrium Climatologies at 1850 and 1998.

Rather than repeat the analysis of Weaver et al. (2000) in full detail, we briefly describe the differences that arise from the use of our new model as well as the varying solar constant. All the major conclusions of Weaver et al. (2000) hold for the present experiments, although the exact magnitude of changes between the transient and equilibrium climatologies are slightly different.

In the case of constant solar forcing, the SAT differences at 1850 and 1998 between the transient and equilibrium climatologies (Fig. 47a,b) are similar to those found in Weaver et al. (2000) (their Fig. 3b,c) even though the models used are quite different. At 1850, the transient climatology is only 0.01°C cooler than the equilibrium climatology (Table 4), increasing to 0.61 °C cooler at 1998. These compare with analogous values of 0.04°C and 0.46°C, respectively, found in Weaver et al. (2000). In all cases the differences are largest at high latitudes, due to amplification by the ice albedo feedback. In addition, changes are much larger in 1998 than in 1850 due to the fact that the climate system has yet to equilibrate to the build up of atmospheric CO_2 over the 20$^{\mathrm{th}}$ century.

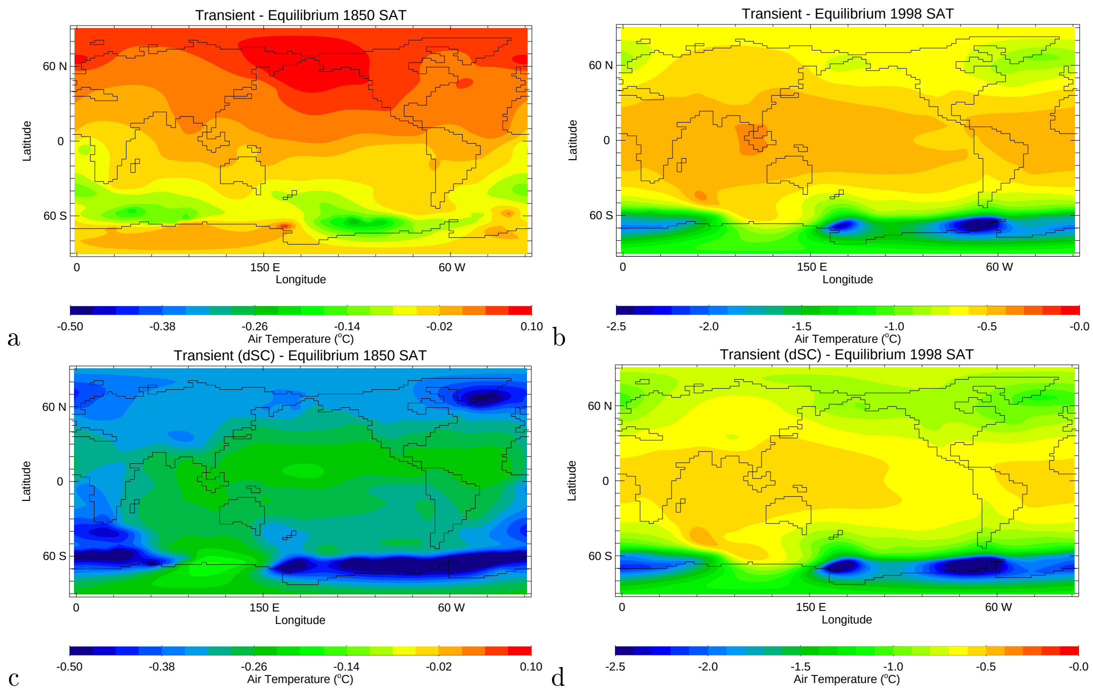

Figure 47: a) Surface air temperature (°C) difference between the transient (without varying solar forcing) and equilibrium model simulations at 1850. b) as in a) but at 1998. c), d) As in a), b), respectively, but with the inclusion of varying solar forcing.

When solar forcing is allowed to vary (Fig. 47 c,d), the differences at 1850 are much larger. In the equilibrium PI experiment, a solar constant of 1368 Wm^{-2} was used, whereas for the period 1610-1850, the Lean et al. (1995) reconstruction gives a constant which at all times is between 1364 and 1367 Wm^{-2}(Fig. 46). As such, the climate during the entire period is colder than the corresponding transient integration with a fixed solar constant, so that at 1850, the PItr ΔS_0 experiment is 0.30°C cooler than PI and 0.29°C cooler than PItr (Table 4; Fig. 48a). The difference between PItr ΔS_0 and PItr reduces by 1998 as the solar constant increases from the end of the Little Ice Age through to the end of the 20$^{\mathrm{th}}$ century (Fig. 48c). Once more, differences are largest at high latitudes where sea ice is present. The general reduction in the differences between the two transient experiments (PItr ΔS_0 and PItr) from 1850 and 1998 is also reflected in the SST field (Fig. 48b,d). Once more, the largest differences tend to be associated with regions near sea-ice boundaries where strong feedbacks exist.

The generally cooler transient climate tends to support more extensive sea ice in both the northern and southern hemispheres, as well as a slightly reduced overturning in the North Atlantic (Fig. 49; Table 4), consistent

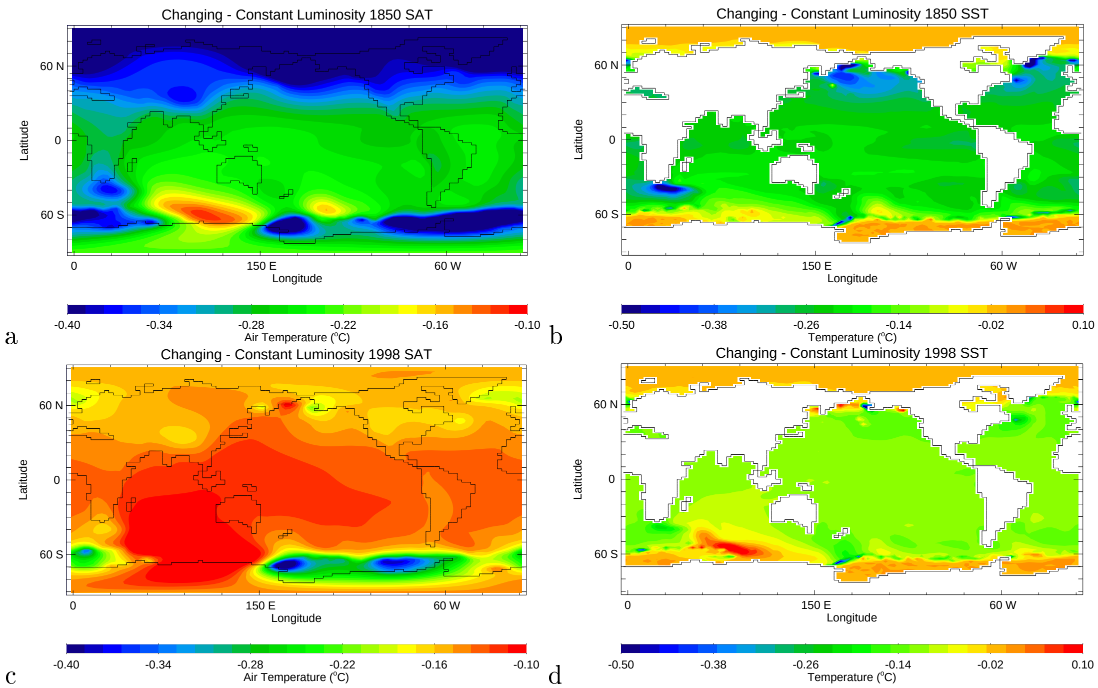

Figure 48: Differences (°C) between the two transient integrations with and without solar forcing. a) Surface air temperature at 1850; b) Sea surface temperature at 1850; c) Surface air temperature at 1998; d) Sea surface temperature at 1998.

with the results of Weaver et al. (2000). In the case of the meridional overturning, however, it is interesting to note that the conveyor remains remarkably stable in all experiments through the 6000 years of integration. Differences between the 6KBP, 1850 and 1998 equilibria are small, as are the differences between the corresponding transient and equilibrium cases (Fig. 49).

As was the case in Weaver et al. (2000), the most significant differences between the 1850 and 1998 equilibrium and transient experiments are associated with sea ice processes and deep ocean convection. These differences are greatest at 1998, by which time the radiative forcing associated with atmospheric CO_2 has increased substantially, relative to preindustrial times. Deep ocean water mass properties (Fig. 50), which retain a memory of the radiative forcing throughout the late Holocene, emphasise the differences between the transient and equilibrium cases especially in the presence of a time varying solar constant.

In summary, our transient versus equilibrium results tend to support the conclusions of Weaver et al. (2000). The inclusion of more sophisticated representations of both sea ice and the atmosphere tended slightly to reduce differences, relative to those found by Weaver et al. (2000), when the solar constant was held fixed. Allowing the solar constant to vary over the last 400 years, however, tended to accentuate the differences between transient and equilibrium integrations, especially at 1998. Taken together, our analysis underlines a potential problem in the evaluation of present day ocean only and coupled atmosphere-ocean general circulation models. In developing

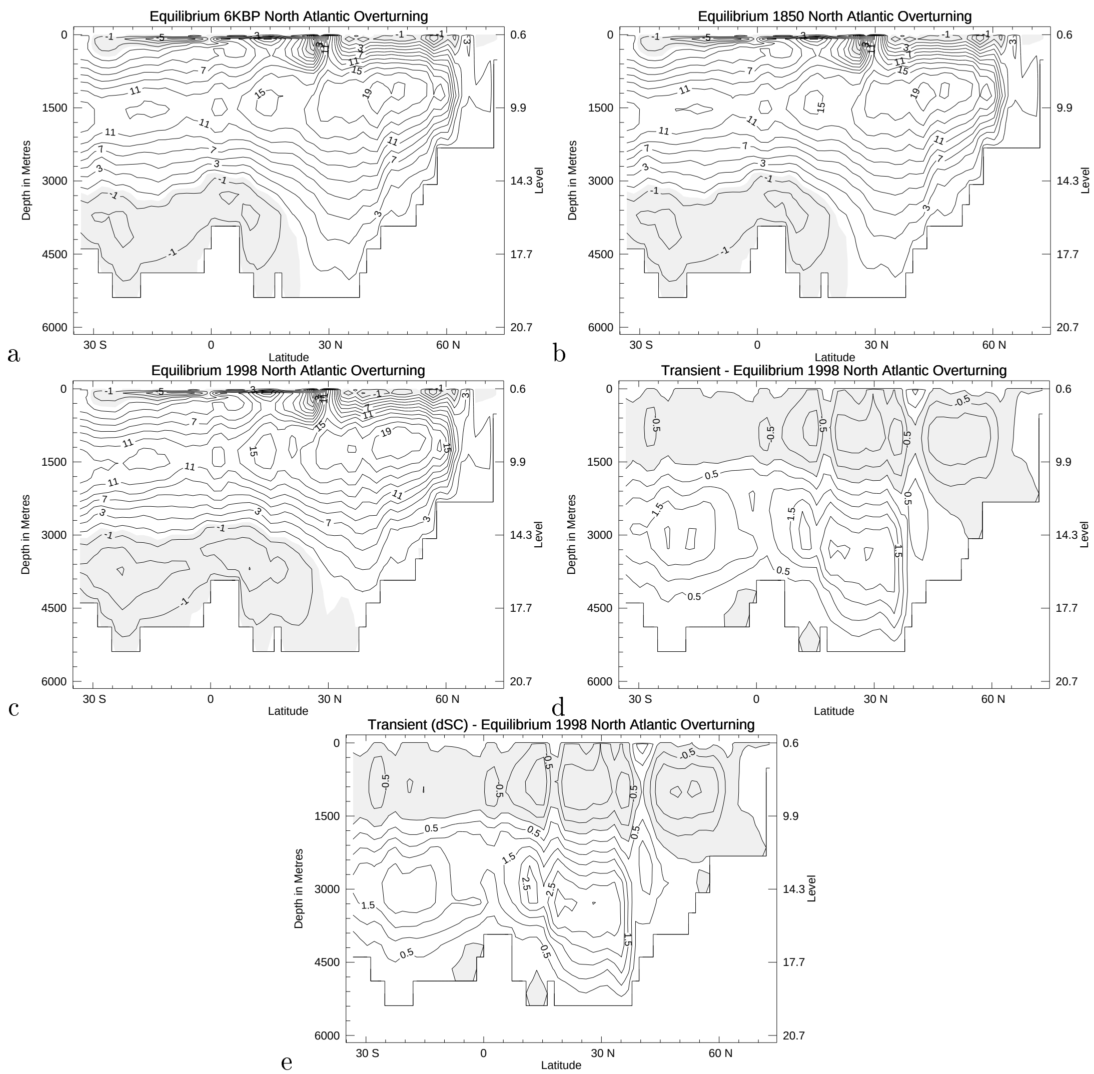

Figure 49: Meridional overturning streamfunction (Sv) in the North Atlantic for. a) Equilibrium 6 KBP climate; b) Equilibrium 1850 climate; c) Equilibrium 1998 climate; d) Transient (no varying solar forcing) minus equilibrium 1998 climate; e) Transient (with solar forcing) minus equilibrium 1998 climate. The contour interval is 2 Sv in a)-c) and 0.5 Sv in d)-e).

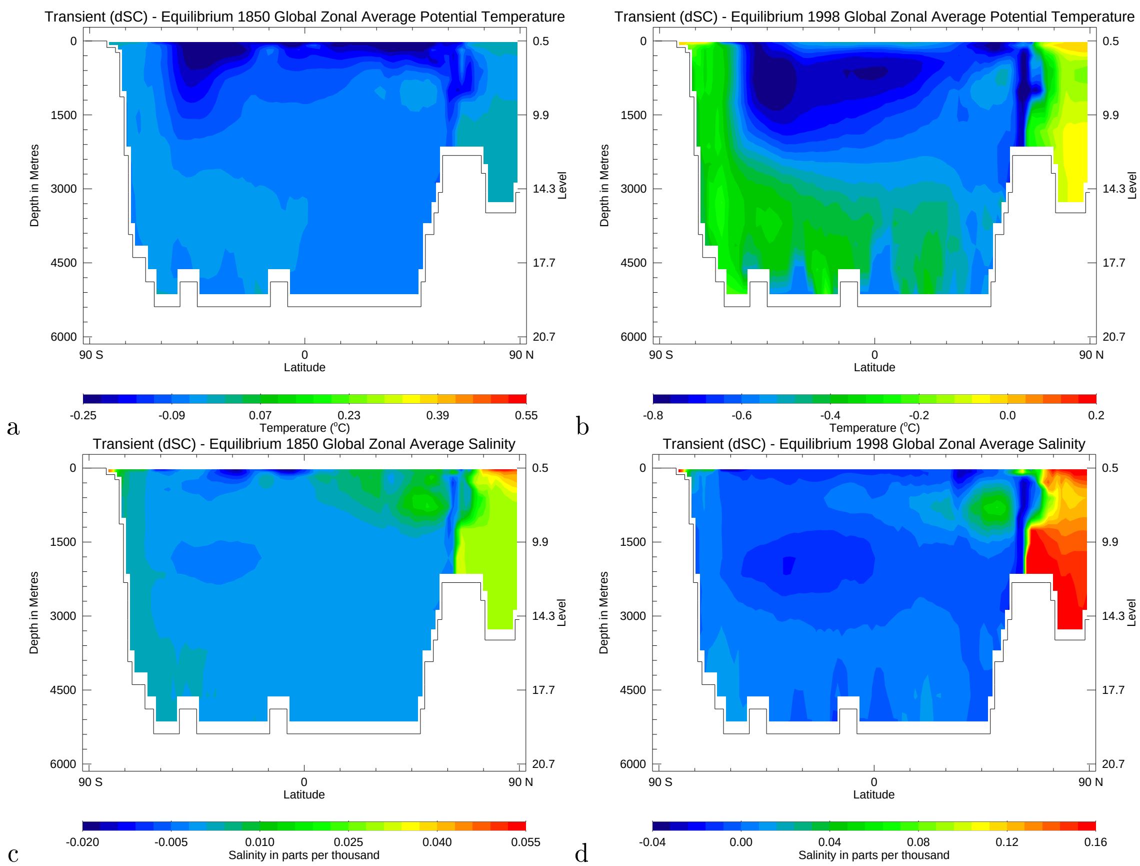

Figure 50: Global zonally-averaged potential temperature (°C). a)- transient (with varying solar forcing) minus equilibrium 1850 climate; b) transient (with varying solar forcing) minus equilibrium 1998 climate. c), d)- As in a), b) but for global zonally-averaged salinity (psu).

these models, it is common to integrate them to equilibrium under present day radiative forcing (in the case of coupled atmosphere-ocean models) or using present day surface boundary conditions (in the case of ocean only models). The evaluation process then involves a detailed comparison of model results with present-day observations. Since the ocean, and especially its deep and weakly ventilated regions, have a long adjustment period to changes in radiative forcing, the present-day oceanic observations are not in equilibrium with the present forcing. Even if the ocean or coupled model were perfect, it would therefore not be possible to reproduce these observations under perpetual present- day model forcing.

7.3 Global warming simulations

We now determine whether or not global warming simulations are sensitive to the approach used to initiate them. Four experiments were performed starting at either the PD (cold start—GWcs), PI (luke warm start—GWlws), PDtr (warm start—GWtr) or PDtr ΔS_0 (warm start—GWtr ΔS_0) initial conditions. The latter two can be viewed as an extension of the transient integration starting at 6KBP, although in the PDtr ΔS_0 case, the solar constant was held fixed at 1368 Wm^{-2}. These four experiments were all integrated out to year 2100 with atmospheric CO_2 increasing at a rate of 1% per year. Only the GWtr and GWcs were further extended to year 2500 (under a $4\times CO_2$ stabilisation scenario).

The projected results at year 2100 for the GWtr, GWtr ΔS_0 and GWlws experiments reveal globally-averaged SATs and SSTs (Fig. 51), sea ice coverage (Fig. 52), steric sea level rise (Fig. 53) and strength of the North Atlantic overturning (Fig.54), that are nearly indistinguishable from each other. The actual change relative to their respective initial conditions (Table 4), further reveals that the GWlws and GWtr experiments lead to almost identical projected changes at the year 2100. The GWtr ΔS_0 experiment, on the other hand, leads to a slightly greater projected warming and reduction in sea ice extent as the initial condition at 1998 was slightly cooler than in the GWlws and GWtr cases. During the further 102 years of integration, some of the warming commitment inherent in the GWtr ΔS_0 case is realised (recall that from 1610 to 1998 the solar constant was almost always below 1368 Wm^{-2} and that after 1998 it was held fixed at 1368 Wm^{-2}). These initial results suggest that projections of global warming conducted by international modelling groups are not affected, at least to first order, by the fact that they have not accounted the radiative forcing prior to 1850. Nevertheless, these same results suggest that were changes in solar variability accounted for, future projections of global warming would be slightly higher than if they were not.

Since the GWtr, GWtr ΔS_0 and GWlws experiments lead to similar results, we only extended the GWtr experiment out to 2500 for comparison with the GWcs experiment. The differences between the cold start and long transient runs are initially much larger than those documented earlier, although by the year 2500, much of

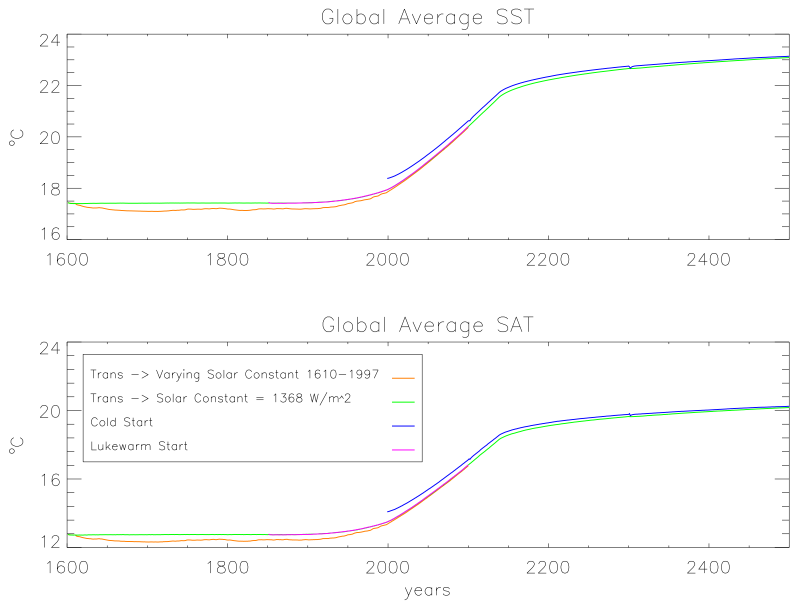

Figure 51: Globally-averaged sea surface temperature (top) and surface air temperature (bottom) as a function of time for the transient integrations with varying (orange) and constant (green) solar forcing. The luke warm start integration (pink) and cold start integration (blue) are also shown.

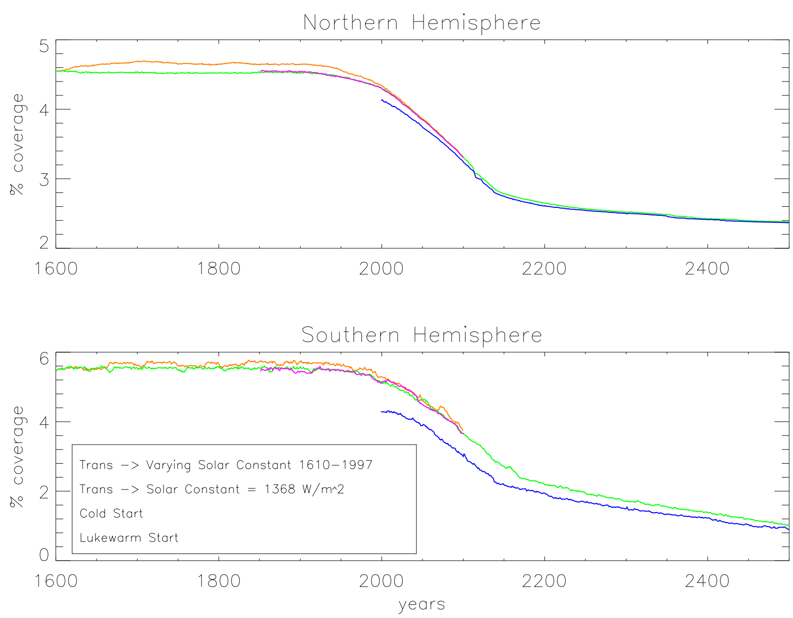

Figure 52: Northern (top) and Southern (bottom) hemispheric sea ice coverage expressed as a fraction of the total hemispheric area for the transient integrations with varying (orange) and constant (green) solar forcing. The luke warm start integration (pink) and cold start integration (blue) are also shown.

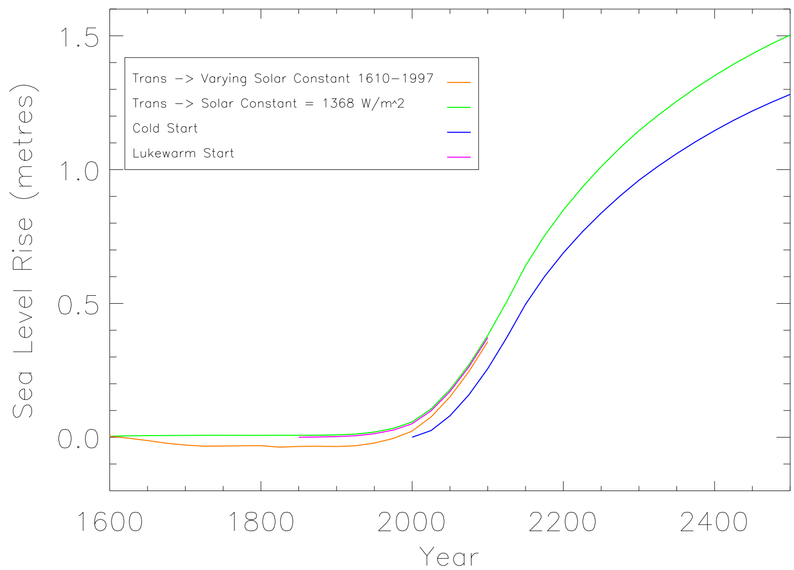

Figure 53: Sea level rise (m) due to thermal expansion relative to the initial condition as a function of time for the transient integrations with varying (pink) and constant (blue) solar forcing. The luke warm start integration (green) and cold start integration (red) are also shown.

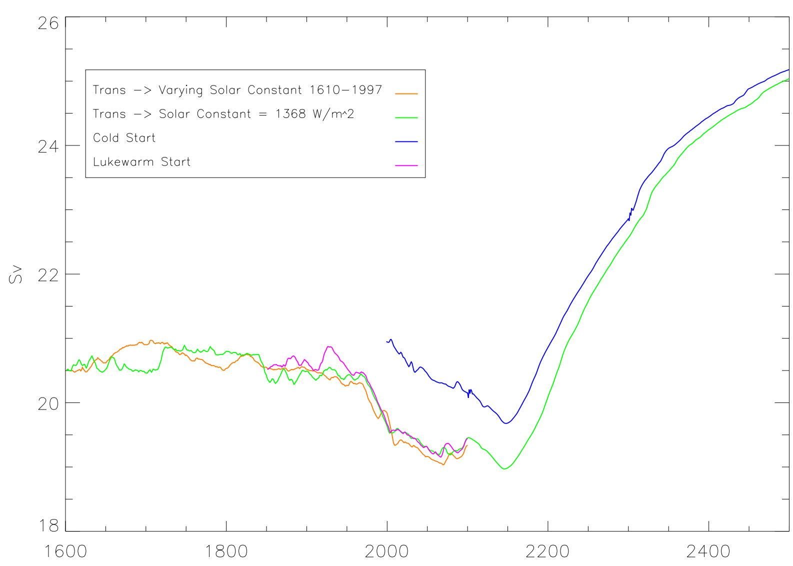

Figure 54: North Atlantic meridional overturning streamfunction (Sv) as a function of time for the transient integrations with varying (pink) and constant (blue) solar forcing. The luke warm start integration (pink) and cold start integration (blue) are also shown.

the warming potential inherent in the long transient run is realized (Fig. 51, 52). The fact that the deep ocean is in equilibrium with the 1998 radiative forcing in GWcs greatly reduces the thermal expansion of the ocean by the year 2500 relative to the GWtr case (Fig. 53). This follows since the timescale for equilibration of the deep ocean to radiative forcing perturbations is on the millennial diffusive timescale. The net result is that the GWtr case produces a projected greater warming, loss of sea ice and sea level rise than the GWcs case (Table 4), due to the warmer initial condition of GWcs.

The meridional overturning streamfunction remains relatively stable in all cases (Figs. 54, 55), with only a $\sim$1Sv weakening occurring during the phase of the integration where the radiative CO_2 forcing was changing. Once the forcing is held fixed, the North Atlantic overturning re-equilibrates to a magnitude slightly larger than its initial condition (Fig. 54). As noted in section 5 and Wiebe and Weaver (1999), this arises from an eventual increase in the zonally-averaged meridional gradient of the depth-integrated steric height in the North Atlantic. As further noted in section 5, the inclusion of wind feedback together with the treatment of moisture transport by advection, causes the overturning to equilibrate to a value similar to its initial condition.

The projected strength of the overturning at the year 2100 is shown in Figs. 55a-d for the GWcs, GWlws, GWtr and GWtr ΔS_0 experiments, respectively. Evidently, the magnitude of the differences between the experiments is small (Figs. 55e-h) in all cases, suggesting a rather passive role of the ocean in terms of local feedbacks to the climate warming. Sea ice feedbacks between the cold start and different transient runs, however, lead to substantial differences in the SAT change at year 2100 (Fig. 56).

The cold start case (GWcs) leads to global mean surface SATs and SSTs at 2100 that are 0.30°C and 0.23°C warmer, respectively, (Fig. 56c; Table 4) than for the corresponding transient case (GWtr). As a consequence, there is less sea ice in both the southern and northern hemispheres in GWcs relative to GWtr (Table 4). In terms of a global mean SAT change at 2100 relative to their respective initial conditions, GWcs produces a $\sim$10% smaller perturbation (3.05°C — Table 4; Fig. 56a) than GWtr (3.35 °C — Table 4) and GWtr ΔS_0 (3.44 °C — Table 4; Fig. 56b). Ironically, the cold start experiment starts from a warmer initial condition and leads to a warmer projected climate than does the warm start experiment. Nevertheless, the resulting projection of global mean SAT change in GWcs is less than the projected change in GWtr and GWtr ΔS_0, due to the warming commitment present in the latter experiment which is partially realised in the future. The differences in the projected global mean SAT anomalies between GWcs and GWtr ΔS_0 (or GWtr) are fairly uniform over the globe (Fig. 56d), although there are a few local maxima present. These occur exclusively near the Antarctic sea ice and Agulhas Retroflection regions.

In summary then, the new version of the model leads to very similar results to those found by Weaver et al. (2000), although some subtle differences exist due to the improved representation of sea ice in the present model.

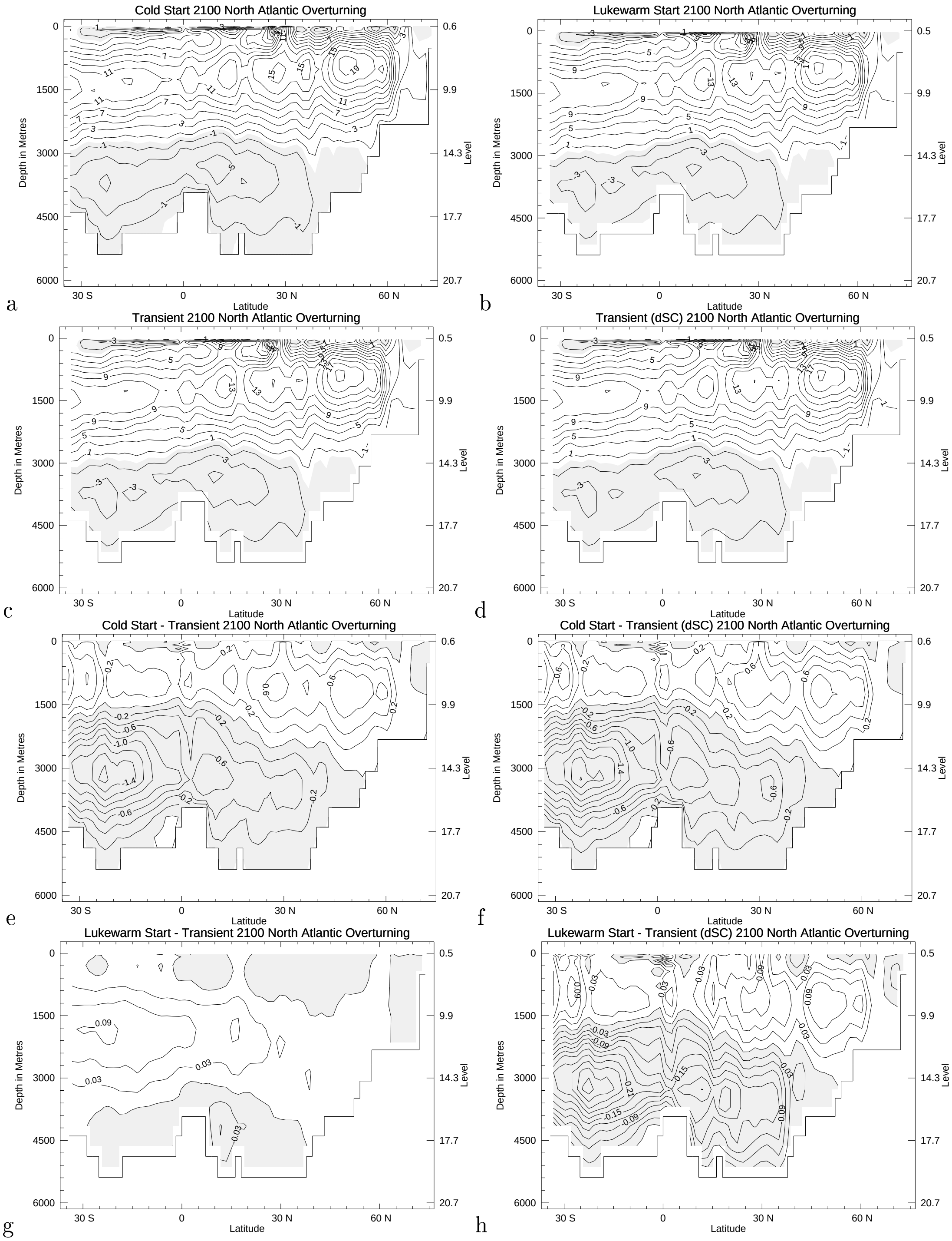

Figure 55: North Atlantic meridional overturning streamfunction (Sv) at 2100 for the global warming experiments. a) Cold start; b) Lukewarm start; c) Transient integration (constant solar forcing); d) Transient integration (varying solar forcing); e) Difference between a) and c); f) Difference between a) and d); g) Difference between b) and c); h) Difference between b) and d). The contour interval is 2 Sv in a)-d, 0.2 Sv in e)-f), and 0.03 Sv in g)-h)

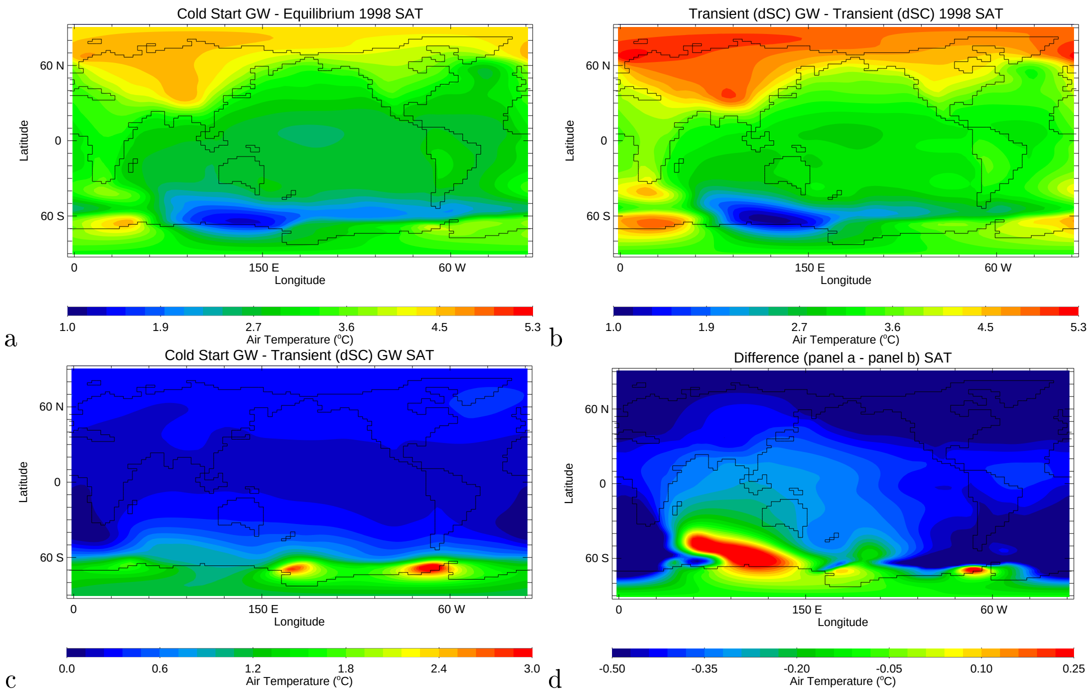

Figure 56: Surface air temperature difference (°C) at 2100 relative to 1998 for a) the cold start experiment and b) the transient experiment with varying solar forcing. c) The difference between the year 2100 cold start and transient climates. d) Panel a) minus panel b) which shows the difference in projected global warming relative to 1998.

Consistent with the results of others (Fichefet and Tricot 1992; Hasselmann et al. 1993; Cubasch et al. 1994; Keen and Murphy 1997; Weaver et al. 2000), we found that the initial rate of warming is slower in 'cold start' global warming experiments than in analogous experiments that start with preindustrial levels of atmospheric CO_2. This follows since the initial conditions for such experiments are in radiative equilibrium with their forcing (e.g., PD), whereas a transient experiment starting from preindustrial times (e.g., PDtr) has a warming commitment (Keen and Murphy 1997), as it has yet to reach radiative equilibrium. As demonstrated by our global warming experiments, SATs at 2100, obtained by starting from the PD (equilibrium 1998) case (GWcs), are generally warmer than in the case where we extended the PDtr (transient 1998) integration (GWtr). This follows since the initial condition is warmer as it is in radiative equilibrium with the forcing. Nevertheless, the global warming relative to 1998 is ∼10% less at 2100 in the cold start case (3.05°C) than in the warm start case (3.35°C), as the latter has a warming commitment which is slowly being realised.

When the effects of varying solar forcing are incorporated into the model, the projected change at 2100 in global mean SAT is larger than in the case where solar forcing is held fixed. This follows since the initial 1998 state of the transient model is colder, in the case where solar forcing is allowed to vary, as it has not reached radiative equilibrium with the solar forcing that slowly increased from preindustrial times through to the late 20th century. In the subsequent 102 years of integration, some of the extra warming commitment inherent in this experiment is therefore realised. This result suggests that those coupled modelling groups that do not account for solar forcing changes over the 20$^{\text{th}}$ century may slightly underestimate (3% in our model) the projected warming by the year 2100.

8 Summary

The UVic ESCM has evolved substantially from its early form as the coupled energy-moisture balance model/OGCM of Fanning and Weaver (1996). It now contains sophisticated sea ice and land ice subcomponent models and an improved representation of the atmosphere. By building the ESCM in a systematic fashion, in which all parameters are consistent between all subcomponent models and careful attention is given to the averaging of fluxes between coupling timesteps, we ensure that energy and moisture are conserved exactly. In this paper we have documented all these subcomponent models, as well as the technique used to couple them, and evaluated the climatology of our model against observations.

The model is able to capture the pathways of intermediate, deep and bottom waters as revealed through simulations involving the release of passive tracers. Also, the model simulates both the cold and warm water routes (Gordon 1986; Rintoul 1991) by which the upper layer water returns to the Atlantic Ocean to compensate for NADW production and export. The global distribution of sea and land ice also compares favourably with observations. This model evaluation procedure also clearly demonstrates the importance of including the process of moisture transport through advection instead of diffusion. When this is done, the simulated evaporation, precipitation and evaporation minus precipitation fields bear reasonable agreement with NCEP reanalysis data.

The inclusion of moisture advection, together with our new parametrisation for wind feedbacks, has a significant influence on the transient response of our model to increasing greenhouse gases. In previous experiments conducted with our model using the diffusive approach for moisture transport, we found that the North Atlantic thermohaline circulation re-established to a level in the future which was stronger than its initial present-day rate. With the aforementioned parametrisation included, the model re-establishes to the same rate as in the present-day climate, consistent with the results from coupled AOGCMs.

When applied to the LGM we find a global mean cooling of 3.8°C, with tropical cooling over the oceans of about 2.1°C and over the land of about 4.4°C. Over the ocean this cooling is in line with recent alkenone reconstructions, although it is cooler than CLIMAP. In the North Atlantic we find less cooling than CLIMAP and a conveyor which is both weaker and shallower than in the present, again consistent with recent reconstructions.

The ESCM was also used to re-examine the issue of climate model initialisation. Our integrations with varying solar constant demonstrated the importance of solar changes during the last few centuries in projecting future climate change. Due to an inherent additional warming commitment, experiments which account for solar forcing changes lead to a greater projected global mean temperature change by 2100.

The examples given in this paper are both interesting from a scientific perspective as well as illustrative of the type of problems that can be addressed with our model. Our philosophy in building this model has been to develop a tool with which to understand processes and feedbacks operating within the climate system on long timescales. We believe that this approach is complementary to that of major coupled AOGCM centres, and that our model fills an important gap within the hierarchy of climate models (Claussen et al. 2000; Shackley et al. 1998). In fact, our model has been used, and is still being used, as a tool with which to examine the sensitivity of a particular process or subcomponent model across a wide range of parameters, in order to streamline the process of improving certain components of the CCCma coupled AOGCM.

We have not yet included a parametrisation for clouds and their feedbacks in our model although given both the lack of understanding of their basic physics, as well as the simplicity of our atmospheric model, it is difficult to see how any meaningful scheme could be incorporated. Clouds have an important role in climate both through their absorption of long wave radiation and through scattering incoming solar radiation back to space. Even the vertical distribution of clouds is important as low clouds, in general, act to cool the planet and high clouds, in general, act to warm it. Different climate models use different approaches to parametrise clouds, many of which are crude at best, leading to cloud feedbacks that vary between models. For example Cess et al. (1996) summarise the cloud feedback from a wide range of atmospheric models. Some models give a positive feedback in global warming experiments (whereby longwave effects dominate), and some give a negative feedback (whereby shortwave effects dominate). While 10 out of the 18 models considered had a net positive feedback, the fact that its sign is largely uncertain is suggestive that our approach is a sensible one. Other caveats of course also apply to our model. In particular, our simple wind feedback scheme is at best a very crude approximation and we do not currently have a land surface scheme in our model. In addition, the fact that we do not explicitly capture atmospheric 'weather' and its chaotic nature means that we are missing an internal stochastic forcing of the complex climate system.

Our model development phase is not yet complete. We are currently in the process of implementing a biotic ocean carbon cycle model into our ESCM following OCMIP guidelines. In addition, we are in the process of incorporating new land surface, terrestrial carbon cycle and dynamic vegetation models. The land-surface scheme used will be a simple, one layer model, computing the energy, moisture and snow balance at the surface as recently developed by P. Cox and K. Meisner. The terrestrial carbon cycle and dynamic vegetation model that we are using is the Hadley Center TRIFFID (Top-down Representation of Interactive Foliage and Flora Including Dynamics; Cox et al. (2000); Cox (2001)). The immediate goal of our work is the development of a comprehensive ESCM with which to explore the mechanisms of Quaternary climate change/variability. Our ultimate goal is the development of a tool which, when coupled to socioeconomic models, forms the basis of an Integrated Assessment approach to exploring the inter-relationship between climate change and climate change policy.

Acknowledgements

Over the years the model development and its applied research have been supported by numerous grants.

We are grateful for funding support provided by the Natural Sciences and Engineering Research Council of Canada (NSERC) Strategic, Operating, WOCE, CSHD, Steacie and Equipment programs, the Meteorological Service of Canada (MSC)/Canadian Institute for Climate Studies (CICS) Canadian Climate Research Network (CCRN), the MSC/NSERC Operating/Strategic subvention program, the NOAA Scripps Lamont Consortium on the Ocean's Role in Climate, the International Arctic Research Center in Fairbanks, Alaska, an IBM Shared University Research Grant, and the Canadian Climate Change Action Fund. We are also grateful to our colleagues in the Canadian Centre for Climate Modelling and Analysis for many years of interesting discussions and to the University of Victoria for infrastructure support. This model is available to the community through http://climate.uvic.ca/climate-lab/model.html. We are grateful to Dr. Xavier Crosta for providing us with his LGM sea ice extent reconstruction data used in Fig. 38a.

Appendix A - Grid Rotation

Any spherical grid rotation can be specified by defining three solid body rotations. The angles which define the rotations are usually referred to as Euler angles (Goldstein 1950). First, define the Z axis to be through the poles such that the X-Y plane defines the equator and the X axis runs through the prime meridian. The angle Φ is defined as a rotation about the original Z axis. Angle Θ is defined as a rotation about the new X axis (after the first rotation) and angle Ψ is defined as a rotation about the final Z axis (Fig. 57).

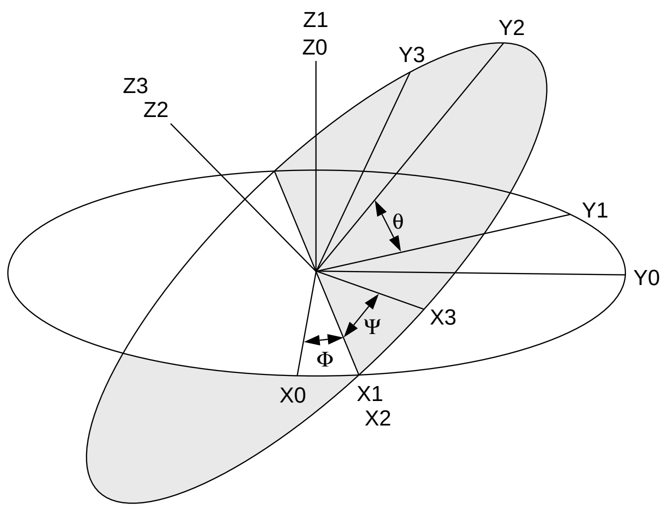

Figure 57: Euler angles

Consider a globe with a clear sphere surrounding it, with only grid lines of latitude and longitude. By moving the outer sphere, the grid poles can be moved to line up with different points on the globe. Once the new poles are located, two of the rotation angles can be defined as follows. The definition for Φ is 90° minus the geographic longitude of the new north pole. This rotates the Y axis under the new pole. To move the Z axis down, Θ is defined to be 90° minus the geographic latitude of the new north pole. This places the original Z axis though the new north pole position.

To completely define the grid, a third rotation about the new Z axis, must be specified. The rotated grid longitude of any point on the geographic grid is still undefined. To specify this last rotation, choose a point on the geographic grid (the globe) to locate the rotated grid's prime meridian. Set angle Ψ to zero and calculate the longitude of this point on the rotated grid. This longitude is the final angle Ψ, the angle needed to rotate the point back to the prime meridian. The definition of Ψ is usually not very important since the new grid longitude is arbitrary, but it does make a difference in defining exactly where the new grid starts. This may be important if it is desirable to line up grids for nesting. It may appear that all of the angle definitions are of the opposite sign to what they should be, but this comes from thinking about rotating the axes rather than rotating the rigid body.

Having defined the angles of rotation, an orthogonal transformation matrix can be written. The first rotation through an angle Φ about the z axis (counterclockwise looking down the Z0 axis) is given by:

$$D = \begin{pmatrix} \cos\Phi & \sin\Phi & 0 \\ -\sin\Phi & \cos\Phi & 0 \\ 0 & 0 & 1 \end{pmatrix}$$

The second rotation through an angle Θ about the new x axis (counterclockwise looking down the X1 axis) is given by:

$$C = \begin{pmatrix} 1 & 0 & 0 \\ 0 & c\cos\Theta & s\sin\Theta \\ 0 & -\sin\Theta & c\cos\Theta \end{pmatrix}$$

and the final rotation through an angle Ψ about the new z axis (counterclockwise looking down the Z2 axis) is given by

$$B = \begin{pmatrix} \cos\Psi & \sin\Psi & 0 \\ -\sin\Psi & \cos\Psi & 0 \\ 0 & 0 & 1 \end{pmatrix}$$

Note that a total rotation matrix can be written as the product of the three rotations BCD (ordering is important). The total rotation matrix A is

$$\begin{pmatrix} \cos\Psi\cos\Phi - \cos\Theta\sin\Phi\sin\Psi & \cos\Psi\sin\Phi + \cos\Theta\cos\Phi\sin\Psi & \sin\Psi\sin\Theta \\ -\sin\Psi\cos\Phi - \cos\Theta\sin\Phi\cos\Psi & -\sin\Psi\sin\Phi + \cos\Theta\cos\Phi\cos\Psi & \cos\Psi\sin\Theta \\ \sin\Theta\sin\Phi & -\sin\Theta\cos\Phi & \cos\Theta \end{pmatrix}$$

Transforming points from the unrotated system to the rotated system (marked by primes) follows from

$$\begin{pmatrix} x' \\ y' \\ z' \end{pmatrix} = A \begin{pmatrix} x \\ y \\ z \end{pmatrix}$$

and transforming points from the rotated system (marked by primes) to the unrotated system follows from

$$\begin{pmatrix} x \\ y \\ z \end{pmatrix} = A^{-1} \begin{pmatrix} x' \\ y' \\ z' \end{pmatrix}$$

where the inverse transform A^{-1} is

$$\begin{pmatrix} \cos\Psi\cos\Phi - \cos\Theta\sin\Phi\sin\Psi & -\sin\Psi\cos\Phi - \cos\Theta\sin\Phi\cos\Psi & \sin\Theta\sin\Phi \\ \cos\Psi\sin\Phi + \cos\Theta\cos\Phi\sin\Psi & -\sin\Psi\sin\Phi + \cos\Theta\cos\Phi\cos\Psi & -\sin\Theta\cos\Phi \\ \sin\Theta\sin\Psi & \sin\Theta\cos\Psi & \cos\Theta \end{pmatrix}$$

Note that the inverse transform A^{-1} is equivalent to A with Ψ and Φ switched and all rotation angles made negative.

Appendix B - Operators in Spherical Coordinates

Tracer Diffusion

$$\begin{aligned}
\nabla \cdot (\xi \nabla \chi) = & \quad \frac{1}{r_e^2 \cos^2 \phi} \frac{\partial}{\partial \lambda} \left(\xi \frac{\partial \chi}{\partial \lambda} \right) \\
+ & \quad \frac{1}{r_e^2 \cos \phi} \frac{\partial}{\partial \phi} \left(\xi \cos \phi \frac{\partial \chi}{\partial \phi} \right)
\end{aligned}$$

Advection

$$\begin{aligned}
L(\xi) = & \quad \frac{1}{r_e \cos \phi} \left(\frac{\partial (u\xi)}{\partial \lambda} + \frac{\partial (v\xi \cos \phi)}{\partial \phi} \right) \\
+ & \quad \frac{\partial (w\xi)}{\partial z}
\end{aligned}$$

Momentum Viscosity

$$\begin{aligned}
\mathcal{F}(A_h, \xi, \chi) = & \quad \nabla \cdot (A_h \nabla \xi) + A_h \left(\frac{1 - \tan^2 \phi}{r_e^2} \right) \xi \\
- & \quad A_h \frac{2 \sin \phi}{r_e^2 \cos^2 \phi} \frac{\partial \chi}{\partial \lambda}
\end{aligned}$$

References

Alley, R. B., 1989: Water-pressure coupling of sliding and bed deformation: II. Velocity-depth profiles. *J. Glaciol.*, **35**, 119–129.

Bard, E., F. Rostek, and C. Sonzogni, 1997: Interhemispheric synchrony of the last deglaciation inferred from alkenone palaeothermometry. *Nature*, **385**, 707–710.

Barnola, J. M., D. Raynaud, Y. S. Korotkevich, and C. Lorius, 1987: Vostok ice core provides 160,000-year record of atmospheric CO_2. *Nature*, **329**, 408–414.

Beck, J. W., J. Récy, F. Taylor, R. L. Edwards, and G. Cabioch, 1997: Abrupt changes in early holocene tropical sea surface temperature derived from coral records. *Nature*, **385**, 705–707.

Berger, A. L., 1978: Long-term variations of daily insolation and Quaternary climate change. *J. Atm. Sci.*, **35**, 2362–2367.

Bitz, C. M., M. M. Holland, A. J. Weaver, and M. Eby, 2001: Simulating the ice-thickness distribution in a coupled climate model. *J. Geophys. Res.*, **106**, 2441–2464.

Bitz, C. M. and W. H. Lipscomb, 1999: An energy-conserving thermodynamic model of sea ice. *J. Geophys. Res.*, **104**, 15669–15677.

Bolton, D., 1980: The computation of equivalent potential temperature. *Mon. Wea. Rev.*, **108**, 1046–1053.

Boyle, E. A. and L. D. Keigwin, 1987: North Atlantic thermohaline circulation during the past 20,000 years linked to high-latitude surface temperature. *Nature*, **330**, 35–40.

Broccoli, A. J., 2000: Tropical cooling at the last glacial maximum: An atmosphere - mixed layer ocean model simulation. *J. Clim.*, **13**, 951–976.

Broccoli, A. J. and S. Manabe, 1987: The influence of continental ice, atmospheric CO_2, and land albedo on the climate of the last glacial maximum. *Clim. Dyn.*, **1**, 87–99.

Bryan, K., 1984: Accelerating the convergence to equilibrium of ocean-climate models. *J. Phys. Oceanogr.*, **14**, 666–673.

Bryan, K. and L. Lewis, 1979: A water mass model of the world ocean. *J. Geophys. Res.*, **84**, 311–337.

Bush, A. B. G. and S. G. H. Philander, 1998: The role of ocean-atmosphere interactions in tropical cooling during the last glacial maximum. *Science*, **279**, 1341–1344.

Cess, R. D., M. H. Zhang, W. J. Ingram, G. L. Potter, V. Alekseev, H. W. Barker, E. Cohen-Solal, R. A. Colman, D. A. Dazlich, A. D. D. Genio, M. R. Dix, V. Dymnikov, M. Esch, L. D. Fowler, J. R. Fraser, V. Galin, W. L. Gates, J. J. Hack, J. T. Kiehl, H. LeTreut, K. W. Lo, B. J. McAvaney, V. P. Meleshko, J. J. Morcette, D. A. Randall, E. Roeckner, J. F. Royer, M. E. Schlesinger, P. V. Sporyshev, B. Timbal, E. M. Volodin, K. E. Taylor, W. Wang, and R. T. Wetherald, 1996: Cloud feedback in atmospheric general circulation models: An update. *J. Geophys. Res.*, **101**, 12791–12794.

Chapman, M. R., N. J. Shackleton, M. Zhao, and G. Eglinton, 1996: Faunal and alkenone reconstructions of north atlantic surface hydrography and paleotemperature over the last 28 kyr. *Paleoceanogr.*, **11**, 343–357.

Charles, C. D. and R. G. Fairbanks, 1992: Evidence from Southern Ocean sediments for the effect of North Atlantic deep-water flux on climate. *Nature*, **355**, 416–419.

Charles, C. D., J. Lynch-Stieglitz, U. S. Ninnemann, and R. G. Fairbanks, 1996: Climate connections between the hemispheres revealed by deep sea sediment core/ice core correlations. *Earth Planet. Sci. Lett.*, **142**, 19–27.

Claussen, M., L. A. Mysak, A. J. Weaver, M. Crucifix, T. Fichefet, M. Loutre, V. A. Alexeev, A. Berger, A. Ganopolski, H. Goosse, G. Lohman, F. Lunkeit, I. Mohkov, V. Petoukhov, S. P., Z. Wang, and S. L. Weber, 2000: Earth system models of intermediate complexity: Closing the gap in the spectrum of climate system models. *Clim. Dyn.*. Submitted.

CLIMAP Project Members, 1976: The surface of the ice-age earth. *Science*, 1131–1137.

CLIMAP Project Members, 1981: Seasonal reconstructions of the earth's surface at the glacial maximum. Technical report, Geol. Soc. Am. Map Chart Ser. MC-36.

Cox, P. M., 2001: Description of the "TRIFFID" Dynamic Global Vegetation Model. Technical Report Technical Note, HCTN24, Hadley Centre.

Cox, P. M., R. A. Betts, C. D. Jones, S. A. Spall, and I. J. Totterdell, 2000: Acceleration of global warming due to carbon cycle feedbacks in a coupled climate model. *Nature*, **408**, 184–187.

Crosta, X., J. J. Pichon, and L. H. Burckle, 1998a: Application of modern analog technique to marine antarctic diatoms: Reconstruction of maximum sea ice extent at the last glacial maximum. *Paleoceanogr.*, **13**, 286–297.

Crosta, X., J. J. Pichon, and L. H. Burckle, 1998b: Reappraisal of antarctic seasonal sea ice at the last glacial maximum. *Geophys. Res. Lett.*, **25**, 2703–2706.

Crowley, T. J., 2000: CLIMAP SSTs re-visited. *Clim. Dyn.*, **16**, 241–255.

Crowley, T. J. and S. Baum, 1997: Effect of vegetation on an ice-age climate model simulation. *J. Geophys. Res.*, **102**, 16463–16480.

Crowley, T. J. and G. R. North, 1991: *Paleoclimatology*. Number 18 in Oxford Monographs on Geology and Geophysics. Oxford University Press. 339 pp.

Cubasch, U., B. D. Santer, A. Hellbach, G. Hegerl, H. Hoeck, E. Maier-Reimer, U. Mikolajewicz, A. Stössel, and R. Voss, 1994: Monte Carlo climate change forecasts with a global coupled ocean-atmosphere model. *Clim. Dyn.*, **10**, 1–19.

Curry, W. B. and G. P. Lohmann, 1983: Reduced advection into Atlantic Ocean deep eastern basins during last glacial maximum. *Nature*, **308**, 317–342.

Curry, W. B. and D. W. Oppo, 1997: Synchronous high-frequency oscillations in tropical sea surface temperatures and North Atlantic deep water production during the last glacial cycles. *Paleoceanogr.*, **12**, 1–14.

da Silva, A. M., C. Young, and S. Levitus, 1994: Atlas of Surface Marine Data 1994: Volume 3, Anomalies of Heat and Momentum Fluxes. Technical Report NOAA Atlas NESDIS 8, U. S. Dept. Commerce, NOAA. 413 pp.

Danabasoglu, G., J. C. McWilliams, and P. R. Gent, 1994: The role of mesoscale tracer transports in the global ocean circulation. *Science*, **264**, 1123–1126.

Duffy, P. B. and K. Caldeira, 1997: Sensitivity of simulated salinity in a three-dimensional ocean model to upper-ocean transport of salt from sea-ice formation. *J. Phys. Oceanogr.*, **27**, 498–523.

Duffy, P. B., M. Eby, and A. J. Weaver, 1999: Effects of sinking of salt rejected during formation of sea ice on results of a global ocean-atmosphere-sea ice climate model. *Geophys. Res. Lett.*, **26**, 1739–1742.

Duffy, P. B., M. Eby, and A. J. Weaver, 2001: Climate model simulations of effects of increased atmospheric CO_2 and loss of sea ice on ocean tracer uptake. *J. Climate*, **14**, 520–532.

Fairbanks, R. G., 1989: A 17,000-year glacio-eustatic sea level record on the Younger Dryas event and deep-ocean circulation. *Nature*, **342**, 637–642.

Fanning, A. F. and A. J. Weaver, 1996: An atmospheric energy-moisture model: Climatology, interpentadal climate change, and coupling to an ocean general circulation model. *J. Geophys. Res.*, **101**, 15111–15128.

Fanning, A. F. and A. J. Weaver, 1997a: On the role of flux adjustments in an idealized coupled climate model. *Clim. Dyn.*, **13**, 691–701.

Fanning, A. F. and A. J. Weaver, 1997b: Temporal-geographical meltwater influences on the North Atlantic conveyor: Implications for the Younger Dryas. *Paleoceanogr.*, **12**, 307–320.

Fichefet, T. and C. Tricot, 1992: Influence of the starting date of model integration on projections of greenhouse gas induced climate change. *Geophys. Res. Lett.*, **19**, 1771–1774.

Flato, G. M., G. J. Boer, N. A. McFarlane, D. Ramsden, M. C. Reader, and A. J. Weaver, 2001: The Canadian Climate Centre for Climate Modelling and Analysis global coupled model and its climate. *Clim. Dyn.*, **16**, 451–467.

Flato, G. M. and W. D. Hibler, 1995: Ridging and strength in modelling the thickness distribution of Arctic sea ice. *J. Geophys. Res.*, **100**, 18611–18626.

Fofonoff, N. P. and R. C. Millard, 1983: Algorithms for computation of fundamental properties of seawater. Technical report, UNESCO Tech. Papers in Marine Sci. No. 44, Paris.

Ganopolski, A., V. Petoukhov, S. Rahmstorf, V. Brovkin, M. Claussen, and C. Kubatzki, 2001: CLIMBER-2: A climate system model of intermediate complexity. Part II: Model sensitivity. *Clim. Dyn.*. In press.

Ganopolski, A., S. Rahmstorf, V. Petoukhov, and M. Claussen, 1998: Simulation of modern and glacial climates with a coupled global model of intermediate complexity. *Nature*, **391**, 351–356.

Gates, W. L., A. Henderson-Sellers, G. J. Boer, C. K. Folland, A. Kitoh, B. J. McAvaney, F. Semazzi, N. Smith, A. J. Weaver, and Q. C. Zeng, 1996: Climate models - evaluation. In J. T. Houghton, L. G. Meira Filho, B. A. Callander, N. Harris, A. Kattenburg, and K. Maskell, editors, *Climate Change 1995 - The Science of Climate Change: Contribution of Working Group I to the Second Assessment Report of the Intergovernmental Panel on Climate Change*, 229–284. Cambridge University Press Cambridge, England.

Gent, P. R. and J. C. McWilliams, 1990: Isopycnal mixing in ocean circulation models. *J. Phys. Oceanogr.*, **20**, 150–155.

Gibson, J. K., P. Kållberg, S. Uppala, A. Nomura, A. Hernandez, E. Serrano, and J. K. Gibson, 1997: ERA description. In *ECMWF Re-Analysis Project Report Series*, volume 1. ECMWF, Reading, UK.

Gill, A. E., 1982: *Atmosphere-Ocean Dynamics*, volume 30 of *Int. Geophys. Ser.*. Academic Press, New York, NY. 662 pp.

Glen, J. W., 1955: The creep of polycrystalline ice. *Proc. Roy. Soc. Lon. A.*, **228**, 519–538.

Glen, J. W., 1958: The flow law of ice. a discussion of the assumptions made in glacier theory, their experimental foundations and consequences. *IASH*, **47**, 171–183.

Gnanadesikan, A., 1999: A simple predictive model for the structure of the oceanic pycnocline. *Science*, **283**, 2077–2079.

Goldstein, H., 1950: *Classical Mechanics*. Addison-Wesley, New York.

Gordon, A. L., 1986: Interocean exchange of thermocline water. *J. Geophys. Res.*, **91**, 5037–5046.

Gordon, A. L., 1997: Which is it: warm or cold route, or maybe both? *WOCE Newsletter*, **28**, 37–38.

Gordon, C., C. Cooper, C. A. Senior, H. Banks, J. M. Gregory, T. C. Johns, J. F. B. Mitchell, and R. A. Wood, 2000: The simulation of sst, sea ice extents and ocean heat transports in a version of the hadley centre coupled model without flux adjustments. *Climate Dynamics*, **16**, 147–168.

Graves, C. E., W. H. Lee, and G. R. North, 1993: New parameterizations and sensitivities for simple climate models. *J. Geophys. Res.*, **98**, 5025–5036.

Guilderson, T. P., R. G. Fairbanks, and J. L. Rubenstone, 1994: Tropical temperature variations since 20,000 years ago: Modulating interhemispheric climate change. *Science*, **263**, 663–665.

Hansen, J., A. Lacis, D. Rind, G. Russell, P. Stone, I. Fung, R. Ruedy, and J. Lerner, 1984: Climate sensitivity: Analysis of feedback mechanisms. In J. E. Hansen and T. Takahashi, editors, *Climate Processes and Climate Sensitivity*, volume 29 of *Geophysical Monograph*, 130–163. Am. Geophys. Union.

Hasselmann, K., R. Sausen, E. Maier-Reimer, and R. Voss, 1993: On the cold start problem in transient simulations with coupled ocean-atmosphere models. *Clim. Dyn.*, **9**, 53–61.

Hebbein, D., T. Dokken, E. Andersen, M. Hald, and A. Elverhol, 1994: Moisture supply for northern ice-sheet growth during the last glacial maximum. *Nature*, **370**, 357–359.

Hibler, W. D., 1979: A dynamic thermodynamic sea ice model. *J. Phys. Oceanogr.*, **9**, 815–846.

Hibler, W. D., 1980: Modeling a variable thickness ice cover. *Mon. Wea. Rev.*, **108**, 1943–1973.

Holland, M. M., C. M. Bitz, M. Eby, and A. J. Weaver, 2001: The role of ice ocean interactions in the variability of the North Atlantic thermohaline circulation. *J. Climate*, **14**, 656–675.

Hughes, T. M. C. and A. J. Weaver, 1994: Multiple equilibria of an asymmetric two-basin ocean model. *J. Phys. Oceanogr.*, **24**, 619–637.

Hunke, E. C. and J. K. Dukowicz, 1997: An elastic-viscous-plastic model for sea ice dynamics. *J. Phys. Oceanogr.*, **27**, 1849–1867.

Hutter, K., 1983: *Theoretical Glaciology: Material Science of Ice and the Mechanics of Glaciers and Ice Sheets*. Reidel. Publishing Company, Dordrecht, Netherlands.

Hutter, K., 1993: Thermo-mechanically coupled ice-sheet response — cold polythermal, temperate. *J. Glaciol.*, **39**, 65–86.

Hyde, W. T., T. J. Crowley, K. Y. Kim, and G. R. North, 1989: Comparison of GCM and energy balance model simulations of seasonal temperature changes over the past 18 000 years. *J. Climate*, **2**, 864–887.

Ikehara, M., K. Kawamura, N. Ohkouchi, K. Kimoto, M. M. amd T. Nakamura, T. Oba, and A. Taira, 1997: Alkenone sea surface temperature in the Southern Ocean for the last two deglaciations. *Geophys. Res. Lett/*, **24**, 679–682.

Isemer, H. J., J. Willebrand, and L. Hasse, 1989: Fine adjustment of large scale air-sea energy flux parameterizations by direct estimates of ocean heat transport. *J. Clim*, **2**, 1173–1184.

Kalnay, E., M. Kanamitsu, R. Kistler, W. Collins, D. Deaven, L. Gandin, M. Iredell, S. Saha, G. White, J. Woollen, Y. Zhu, A. Leetmaa, and R. Reynolds, 1996: The NCEP/NCAR 40 year reanalysis project. *Bull. Amer. Meteor. Soc.*, **77**, 437–471.

Kattenberg, A., F. Giorgi, H. Grassl, G. A. Meehl, J. F. B. Mitchell, R. J. Stouffer, T. Tokioka, A. J. Weaver, and T. M. L. Wigley, 1996: Climate models-projections of future climate. In J. T. Houghton, L. G. Meira Filho, B. A. Callander, N. Harris, A. Kattenburg, and K. Maskell, editors, *Climate Change 1995*, 285–357. Cambridge University Press.

Keen, A. B. and J. M. Murphy, 1997: Influence of natural variability and the cold start problem on the simulated transient response to increasing CO_2. *Clim. Dyn.*, **13**, 835–845.

Kutzbach, J. E. and P. J. Guetter, 1986: The influence of changing orbital parameters and surface boundary conditions on climate simulations for the past 18,000 years. *J. Atmos. Sci.*, **43**, 1726–1759.

Lautenschlager, M. and K. Herterich, 1990: Atmospheric response to ice age conditions: climatology near the earth's surface. *J. Geophys. Res.*, **95**, 22547–22557.

Lea, D. W. and E. A. Boyle, 1990: Foraminiferal reconstructions of barium distributions in water masses of the glacial ocean. *Paleoceanogr.*, **5**, 719–742.

Lean, J. L., J. Beer, and R. Bradley, 1995: Reconstruction of solar irradiance since 1610: I implications for climate change. *Geophys. Res. Lett.*, **22**.

Levitus, S. and T. P. Boyer, 1994: *NOAA Atlas NESDIS 4, World Ocean Atlas 1994, Volume 4: Temperature*. NOAA, U. S. Dept. Commerce. 117 pp.

Levitus, S., R. Burgett, and T. P. Boyer, 1994: *NOAA Atlas NESDIS 3, World Ocean Atlas 1994, Volume 3: Salinity*. NOAA, U. S. Dept. Commerce. 99 pp.

Lyle, M. W., F. G. Prahl, and M. A. Sparrow, 1992: Upwelling and productivity changes inferred from a temperature record in the central equatorial pacific. *Nature*, **355**, 812–815.

Manabe, S. and A. J. Broccoli, 1985: The influence of continental ice sheets on the climate of an ice age. *J. Geophys. Res*, **90**, 2167–2190.

Manabe, S. and K. Bryan, 1985: CO_2-induced change in a coupled ocean-atmosphere model and its paleoclimatic implications. *J. Geophys. Res*, **90**, 11689–11707.

Manabe, S. and R. J. Stouffer, 1988: Two stable equilibria of a coupled ocean-atmosphere model. *J. Climate*, **1**, 841–866.

Manabe, S. and R. J. Stouffer, 1999: Are two modes of thermohaline circulation stable? *Tellus*, **51A**, 400–411.

Marshall, S. J., 1996: *Modelling Laurentide Ice Stream Thermomechanics*. Ph.D. thesis, University of British Columbia, Vancouver, B. C., Canada.

Marshall, S. J. and G. K. C. Clarke, 1997a: A continuum mixture model of ice stream thermomechanics in the Laurentide ice sheet, 1. theory. *J. Geophys. Res.*, **102**, 20599–20614.

Marshall, S. J. and G. K. C. Clarke, 1997b: A continuum mixture model of ice stream thermomechanics in the Laurentide ice sheet, 2. application to the Hudson Strait ice stream. *J. Geophys. Res.*, **102**, 20599–20614.

McFarlane, N. A., G. J. Boer, J. P. Blanchet, and M. Lazare, 1992: The Canadian Climate Centre second-generation general circulation model and its equilibrium climate. *J. Climate*, **5**, 1013–1044.

McPhee, M. G., 1992: Turbulent heat flux in the upper ocean under sea ice. *J. Geophys. Res.*, **97**, 5365–5379.

Mitchell, J. F. B., T. C. Johns, J. M. Gregory, and S. F. B. Tett, 1995: Climate response to increasing levels of greenhouse gases and sulphate aerosols. *Nature*, **376**, 501–504.

Oppo, D. W. and G. Fairbanks, 1987: Variability in the deep and intermediate water circulation of the Atlantic Ocean during the past 25,000 years: Northern Hemisphere modulation of the Southern Ocean. *Earth Planet. Sci. Lett.*, **86**, 1–15.

Oreskes, K. S., N. and K. Belitz, 1994: Verification, validation, and confirmation of numerical models in the earth sciences. *Science*, **263**, 641–646.

Orr, J. C., R. Najjar, C. L. Sabine, and F. Joos, 1999: Abiotic-HOWTO. Internal OCMIP Report, LSCE/CEA Saclay, Gif-sur-Yvette, France.

Pacanowski, R., 1995: *MOM 2 Documentation User's Guide and Reference Manual, GFDL Ocean Group Technical Report*. NOAA, GFDL, Princeton. 232pp.

Paterson, W. S. B., 1994: *The Physics of Glaciers*. Elsevier, New York, third edition. 480 pp.

Peixoto, J. P. and A. H. Oort, 1992: *Physics of Climate*. American Institute of Physics, New York. 520 pp.

Peltier, W. R., 1994: Ice age paleotopography. *Science*, **265**, 195–201.

Peltier, W. R. and S. Marshall, 1995: Coupled energy-balance/ice-sheet model simulations of the glacial cycle: A possible connection between terminations and terrigenous dust. *J. Geophys. Res.*, **100**, 14,269–14,289.

Petit, J. R., M. Briat, and A. Royer, 1981: Ice age aerosol content from east antarctica ice core samples and past wind strength. *Nature*, **293**, 391–394.

Petoukhov, V., A. Ganopolski, V. Brovkin, M. Claussen, A. Eliseev, C. Kubatzki, and S. Rahmstorf, 2000: CLIMBER-2: A climate system model of intermediate complexity. Part I: Model description and performance for present climate. *Clim. Dyn.*, **16**, 1–17.

Poussart, P. F., A. J. Weaver, and C. R. Barnes, 1999: Late Ordovician glaciation under high atmospheric CO_2: A coupled model analysis. *Paleoceanogr.*, **14**, 542–558.

Rahmstorf, S. and A. Ganopolski, 1999: Long-term warming scenarios computed with an efficient coupled climate model. *Clim. Change*, **43**, 353–367.

Ramanathan, V., L. Callis, R. Cess, J. Hansen, I. Isaksen, W. Kuhn, A. Lacis, F. Luther, J. Mahlman, P. Reck, and M. Schlesinger, 1987: Climate-chemical interactions and effects of changing atmospheric trace gases. *Rev. Geophys.*, **25**, 1441–1482.

Raper, S. C. B., T. M. L. Wigley, and R. A. Warrick, 1996: Global sea-level rise: past and future. In J. D. Milliman and B. U. Haq, editors, *Sea-Level Rise and Coastal Subsidence*, 11–46. Kluwer Academic Publishers.

Rintoul, S. R., 1991: South Atlantic interbasin exchange. *J. Geophysical Research*, **96**, 2675–2692.

Robitaille, D. Y. and A. J. Weaver, 1995: Validation of sub-grid-scale mixing schemes using CFCs in a global ocean model. *Geophys. Res. Lett.*, **22**, 2917–2920.

Rostek, F., G. Ruhland, F. Bassinot, P. J. Mueller, L. D. Labeyrie, Y. Lancelot, and E. Bard, 1993: Reconstructing sea surface temperature and salinity using $\delta^1 8o$ and alkenone records. *Nature*, **364**, 319–321.

Rothrock, D. A., 1975: The energetics of the plastic deformation of pack ice by ridging. *J. Geophys. Res.*, **80**, 4514–4519.

Rothrock, D. A., 1986: Ice thickness distribution-measurement and theory. In N. Untersteiner, editor, *The Geophysics of Sea Ice*, volume 146, 551–575. NATO ASI Series B, Pysics, Plenum, New York, London.

Rutberg, R. L., S. R. Hemming, and S. L. Goldstein, 2000: Reduced North Atlantic deep water flux to the glacial Southern Ocean inferred from neodymium isotope ratios. *Nature*, **405**, 935–938.

Saenko, O., G. M. Flato, and A. J. Weaver, 2001: Improved representation of sea ice processes in climate models. *Atmos.-Ocean*. In press.

Schiller, A., U. Mikolajewicz, and R. Voss, 1997: The stability of the North Atlantic thermohaline circulation in a coupled ocean-atmosphere general circulation model. *Clim. Dyn.*, **13**, 325.

Schneider, R. R., P. J. Muller, and G. Ruhland, 1995: Late Quaternary surface circulation in the east equatorial South Atlantic: Evidence from alkenone sea surface temperatures. *Paleoceanogr.*, **10**, 197–219.

Schwarzacher, W., 1959: Pack ice studies in the Arctic Ocean. *J. Geophys. Res.*, **64**, 2357–2367.

Semtner, A. J., 1976: A model for the thermodynamic growth of sea ice in numerical investigations of climate. *J. Phys. Oceanogr.*, **6**, 379–389.

Shackley, S., P. Young, S. Parkinson, and B. Wynne, 1998: Uncertainty, complexity and concepts of good science in climate change modelling. *Climatic Change*, **38**, 159–205.

Sher, A., 1995: Is there and real evidence for a huge ice sheet in East Siberia? *Quat. Int.*, **28**, 39–40.

Sikes, E. L. and L. Keigwin, 1994: Equatorial atlantic sea surface temperature for the last 30 kyr: A comparison of $U_{37}^{k'}\delta^{18}$ and foraminiferal assemblage temperature estimates. *Paleoceanogr.*, **9**, 31–45.

Stocker, T. F. and A. Schmittner, 1997: Influence of CO_2 emission rates on the stability of the thermohaline circulation. *Nature*, **388**, 862–865.

Stocker, T. F., D. G. Wright, and L. A. Mysak, 1992: A zonally averaged, coupled ocean-atmosphere model for paleoclimate studies. *J. Climate*, **5**, 773–797.

Stute, M., M. Forster, H. Frischkorn, A. Serejo, J. F. Clark, P. Schlosser, W. S. Broecker, and G. Bonani, 1995: Cooling of tropical Brazil (5^oC) during the last glacial maximum. *Science*, **269**, 379–383.

Suarez, M. J. and L. L. Takacs, 1986: Global 5'x5' depth and elevation. Technical report, National Geophysical Data Centre, NOAA, US Dept of Commerce, Code E/GC3, Boulder CO 80303.

Tarasov, L. and W. R. Peltier, 1997: A high-resolution model of the 100 ka ice-age cycle. *Ann Glaciol.*, **25**, 58–65.

Thompson, L. G., E. Mosley-Thompson, M. E. Davis, P. N. Lin, K. A. Henderson, J. Cole-Dai, J. F. Bolzan, and K. B. Liu, 1995: Late glacial stage and holocene tropical ice core records from Huascarán, Peru. *Science*, **269**, 46–50.

Thompson, S. L. and S. G. Warren, 1982: Parameterization of outgoing infrared radiation derived from detailed radiative calculations. *J. Atm. Sci.*, **39**, 2667–2680.

Thorndike, A. S., D. A. Rothrock, G. A. Maykut, and R. Colony, 1975: The thickness distribution of sea ice. *J. Geophys. Res.*, **80**, 4501–4513.

Thorpe, R., J. M. Gregory, T. C. Johns, R. A. Wood, and J. F. B. Mitchell, 2001: Mechanisms determining the Atlantic thermohaline response to greenhouse gas forcing in a non-fluxadjusted coupled climate model. *J. Climate*. In press.

Toggweiler, R. and B. Samuels, 1995: Effect of Drake Passage on the global thermohaline circulation. *Deep-Sea Res.*, **42**, 477–500.

UNESCO, 1981: 10th report of the joint panel on oceanographic tables and standards. Technical report, UNESCO Tech. Papers in Marine Sci. No. 36, Paris.

van de Wal, R. S. W., 1999: The importance of thermodynamics for modeling the volume of the greenland ice sheet. *J. Geophys. Res.*, **104**, 3887–3898.

Wanninkhof, R., 1992: Relationship between wind speed and gas exchange over the ocean. *J. Geophys. Res.*, **97**, 7373–7382.

Weaver, A. J., P. B. Duffy, M. Eby, and E. C. Wiebe, 2000: Evaluation of ocean and climate models using present-day observations and forcing. *Atmos. Ocean*, **38**, 271–301.

Weaver, A. J., M. Eby, A. F. Fanning, and E. C. Wiebe, 1998: Simulated influence of carbon dioxide, orbital forcing and ice sheets on the climate of the Last Glacial Maximum. *Nature*, **394**, 847–853.

Weaver, A. J. and T. M. C. Hughes, 1996: On the incompatibility of ocean and atmosphere models and the need for flux adjustments. *Clim. Dyn.*, **12**, 141–170.

Weaver, A. J. and E. C. Wiebe, 1999: On the sensitivity of projected oceanic thermal expansion to the parameterisation of sub-grid scale ocean mixing. *Geophys. Res. Lett.*, **26**, 3461–3464.

Webb, R. S., D. H. Rind, and D. Sigman, 1997: Influence of ocean heat transport on the climate of the last glacial maximum. *Nature.*, **385**, 695.

Wiebe, E. C. and A. J. Weaver, 1999: On the sensitivity of global warming experiments to the parameterisation of sub-grid-scale ocean mixing. *Clim. Dyn.*, **15**, 875–893.

Wigley, T. M. L., 1998: The Kyoto Protocol: CO_2, CH_4, and climate implictaions. *Geophys. Res. Let.*, **25**, 2285–2288.

Wigley, T. M. L. and S. C. B. Raper, 1987: Thermal expansion of sea water associated with global warming. *Nature*, **330**, 127–131.

Wigley, T. M. L. and S. C. B. Raper, 1992: Implications for climate and sea level of revised IPCC emissions scenarios. *Nature*, **357**, 293–300.

Yoshimori, M., A. J. Weaver, S. J. Marshall, and G. K. C. Clarke, 2001: Glacial termination: Sensitivity to orbital and CO_2 forcing in a coupled climate system model. *Climate Dynamics*. In press.